Ductile damage and fracture behavior in metal sheets under reverse loading: Experiments, modeling and numerical analysis

Zhichao Wei

Abstract

This thesis deals with experimental and numerical analysis of ductile damage and fracture behavior under reverse loading conditions. The experimental part includes novel one-axial and biaxial monotonic and reverse experiments conducted on different specimens taken from ductile aluminum alloy EN AW 6082-T6 sheet with a thickness of 4 mm. For this purpose, different one-axis-loaded and biaxially loaded specimens have been newly designed to generate a wide range of stress states under various reverse experiments. An anti-buckling device is used in uniaxial compression tests, and a down-holder is employed in biaxial testing to prevent buckling. The digital image correlation (DIC) technique is used to record and analyze displacements and strain fields, while scanning electron microscopy (SEM) images of fractured surfaces are utilized to verify the proposed damage mechanism. In the numerical part, an anisotropic two-surface cyclic plastic-damage constitutive model based on the framework of Brünig (2003a) is proposed, incorporating combined isotropic-kinematic hardening and softening laws. The plasticity model is further extended to simulate the Bauschinger effect, the strength-differential effect, and the non-hardening effect after shear reverse loading. Moreover, a novel kinematic softening rule based on Brünig's damage strain rate tensor is added to the damage condition to describe the movement of the damage surface. An efficient Euler explicit numerical integration is realized by the inelastic (plastic or plastic-damage) predictor-elastic corrector approach. In-depth discussions are presented on various consistent tangent operators related to numerical integration aimed at achieving convergence in the global Newton-Raphson scheme. The proposed constitutive model is implemented as a user-defined subroutine (UMAT) into the commercial software Ansys. The comparison between experimental and numerical results, encompassing global load-displacement curves and local strain fields, as well as the numerically predicted damage evolution and experimentally obtained SEM images, offers a comprehensive explanation of the influence of reverse loading histories on ductile damage and fracture behavior at both micro- and macro-levels.

Zusammenfassung

Diese Dissertation behandelt die experimentelle und numerische Analyse des duktilen Schädigungs- und Versagensverhaltens unter zyklischen Belastungen. Der experimentelle Teil umfasst neuartige einachsige und biaxiale, monotone und zyklische Versuche, die an verschiedenen Proben (4 mm Dicke) der duktilen Aluminiumlegierung EN AW 6082-T6 durchgeführt wurden. Zu diesem Zweck wurden verschiedene einachsige und biaxiale Proben neu entworfen, um eine große Bandbreite an Spannungszuständen unter verschiedenen zyklischen Belastungen zu erzeugen. Eine Druckvorrichtung wird bei einachsigen Druckversuchen verwendet und ein Niederhalter bei biaxialen Versuchen gegen Beulen eingesetzt. Die digitale Bildkorrelation erfasst und analysiert Verschiebungen und Dehnungsfelder, während Rasterelektronenmikroskop (REM)-Aufnahmen von den Bruchflächen zur Überprüfung der prognostizierten Schädigungsmechanismen verwendet werden. Im numerischen Teil wird ein anisotropes, zyklisches Plastizitäts-Schädigungsmodell basierend auf dem Ansatz von Brünig (2003a) vorgeschlagen, das kombinierte isotrop-kinematische Verfestigungs- und Entfestigungsgesetze integriert. Das Plastizitätsmodell wird weiterentwickelt, um den Bauschingereffekt, den Strength-Differential-Effekt und den Nicht-Verfestigungs-Effekt nach Scherumkehrbelastung zu simulieren. Darüber hinaus wird ein neuartiges kinematisches Entfestigungsmodell, basierend auf Brünigs Schädigungsdehnungstensor, eingeführt, um die kinematische Änderung der Schädigungsfläche zu beschreiben. Eine effiziente explizite numerische Euler-Integration wird durch den inelastischen Prädiktor-elastischen Korrektor-Ansatz realisiert. Verschiedene konsistente Tangentenoperatoren werden im Rahmen der numerischen Integration ausführlich diskutiert, um die Konvergenz im globalen Newton-Raphson-Schema zu gewährleisten. Das vorgeschlagene konstitutive Modell wird als benutzerdefiniertes Materialmodell in die Software Ansys implementiert. Der Vergleich zwischen experimentellen und numerischen Ergebnissen, einschließlich globaler Last-Verschiebungs-Kurven und lokaler Dehnungsfelder, sowie der numerisch vorhergesagten Schädigungsentwicklungen und den REM-Aufnahmen bietet eine umfassende Erklärung für den Einfluss von zyklischen Belastungsgeschichten auf das duktile Schädigungs- und Versagensverhalten auf mikro- und makroskopischer Ebene.

Acknowledgment

This thesis was developed during my tenure as a research assistant at the Institute for Mechanics and Structural Analysis, University of the Bundeswehr Munich. It was funded by the Deutsche Forschungsgemeinschaft (DFG, German Research Foundation). I gratefully acknowledge this financial support.

First and foremost, I must express my deepest gratitude to my supervisor, Prof. Dr. Michael Brünig, for his dedication to developing damage and fracture theory since the 1990s. His persistence and academic rigor in researching damage and fracture issues have deeply inspired my own interest in academia. He has consistently provided me with deep discussions and valuable suggestions to address my concerns throughout my research journey. The unlimited academic freedom and strong support in academia provided by him have emboldened me to accomplish many tasks that once appeared daunting. I also extend my thanks to Prof. Dr. Thomas Apel for chairing my examination, and to Prof. Dr. Holm Altenbach and Prof. Dr. Franz-Joseph Barthold for their thorough review of my thesis.

Secondly, I would like to thank PD Dr. Steffen Gerke for his efficient support, especially in developing experimental specimens and solving problems related to experimental techniques. His extensive knowledge of experimental work inspired my interest in this field and new ideas, enabling us to successfully design experimental directions through collaborative discussions with Prof. Dr. Brünig. I also want to extend my thanks to my colleagues, Dr. Moritz Zistl and Sanjeev Koirala, for their invaluable discussions on numerical implementations and simulations, as well as their assistance in conducting experiments. I am grateful to Wolfgang Saur for providing technical support with the one-axis testing machine and the use of the scanning electron microscopy.

Lastly, but also important, I would like to thank my parents for their financial support during my Master's studies in Germany, which enabled me to earn my master's degree in 2019 and to continue pursuing my PhD. Additionally, I am grateful to my older sister, whose care for our parents in China allowed me to focus on my research in Germany. I also want to thank myself for making the essential decision to come to Germany in 2013 to continue my academic journey, and for being the person who dared to persevere through every setback encountered along the way.

Contents

1 Introduction

1.1 Background

Numerical modeling of ductile damage and fracture behavior has emerged as a significant research field in recent decades. This approach is precious, considering that actual full-scale experiments in the industry are often costly and impractical. It is also well-established that nucleation, growth, and coalescence of micro-defects, such as micro-voids and micro-shear-cracks, are key mechanisms resulting in damage in ductile metals. Moreover, the influence of the stress triaxialities on the damage and fracture behavior has been extensively discussed in the literature (Bao and Wierzbicki, 2004, 2005; Brünig et al., 2008, 2014; Gao et al., 2010; Lou and Yoon, 2018; Lou et al., 2020; Wei et al., 2023b, 2022). In high stress triaxialities, damage is induced by the growth and coalescence of micro-voids, while in conditions of low negative stress states, damage arises from the growth and coalescence of micro-shear-cracks. Furthermore, Bao and Wierzbicki (2005) analyzed experimental data from upsetting tests for the aluminum alloy Al2024-T351 with cylindrical specimens and concluded that damage does not occur below the cut-off value of stress triaxiality, specifically when it is lower than $-1/3$. However, as studied by A. S. Khan and Liu (2012) through uniaxial tension followed by torsion and biaxial non-proportional compression tests, this aluminum alloy indicates that the cut-off values are not constant and depend on various stress states. Furthermore, Brünig et al. (2018) conducted a series of shear-compression biaxial experiments, and their analysis of both experimental and numerical results demonstrates that the cut-off values for stress triaxialities also depend on the Lode parameter. Additionally, the shear deformation component plays a crucial role in negative stress states, as also observed by Lou et al. (2014). The findings above underscore the necessity of a sophisticated phenomenological damage model to accurately capture the effects of varying stress states on material behavior.

A substantial body of literature on damage models is available, primarily divided into two types: (1) Gurson's damage hypothesis and (2) continuum damage mechanics (CDM). In Gurson's damage model (Gurson, 1977), damage is represented by the volume fraction, or porosity, which increases due to the nucleation and growth of micro-voids. In the numerical study of a rigid-plastic cell containing a single spherical void, porosity is incorporated into the yield criterion to model the softening effect. However, the original Gurson model cannot capture fracture and the effects of coalescence of micro-voids. To address these limitations, Tvergaard and Needleman (1984) introduced several parameters into the classic Gurson model, the so-called GTN model, which was further explored through various studies such as those by Chu and Needleman (1980), Faleskog et al. (1998), and Koplik and Needleman (1988). Subsequently, the GTN model has been extensively modified, as documented in the literature, to more accurately capture shear failure behaviors, with significant contributions from studies by I. A. Khan et al. (2023), Malcher et al. (2014), and Nahshon and Hutchinson (2008). It should be noted that Gurson-type damage models solely affect the plastic behavior and do not alter the material's elastic properties. This assumption appears somewhat inconsistent with experimental findings, which indicate that Young's modulus tends to decrease in tensile with loading and reloading experiments (Lemaitre and Dufailly, 1987; Voyiadjis et al., 2013; Wei et al., 2022). Thus, Rousselier (1987, 2001) considered the elastic properties change due to the damage in Gurson's type model. In addition, Rousselier and Luo (2014) introduced a comprehensive model that integrates void damage with a combined Mohr-Coulomb ductile fracture model for micro-shear-cracks. More recently, Rousselier (2022) enhanced this model by incorporating a Lode-dependent second porosity, which significantly improves the accuracy of modeling ductile damage behavior, particularly under shear-dominated loading conditions that involve void rotation and flattening.

The continuum damage mechanics (CDM) represents another phenomenological and widely utilized approach for predicting the evolution of damage. This approach primarily consists of two categories: the scalar parameter-based isotropic damage model (among of others Algarni et al. (2019), Lemaitre (1985a,b, 1986, 1996), Rabotnov (1969), Rong et al. (2022), Saanouni (2008), and Voyiadjis et al. (2012)) and the vector or

tensor-based anisotropic damage model (for example, Abu Al-Rub and Voyiadjis (2003), Badreddine and Saanouni (2017), Balieu and Kringos (2015), Brünig (2003a,b), Brünig et al. (2023), Chaboche (1984, 1992), Lemaitre et al. (2000), Murakami (1988, 2012), Simo and Ju (1987), Vignjevic et al. (2012), and Voyiadjis and Kattan (1992, 2005)). The principles of strain equivalence and effective stress are fundamental in realizing the theory of CDM. The concept of effective stress is based on introducing a fictitious undamaged configuration, in which no damage deformations are considered (Abu Al-Rub and Voyiadjis, 2003; Balieu and Kringos, 2015; Brünig, 2003a; Chaboche, 1992; Lemaitre, 1985a). In addition, the strain behavior in the undamaged configuration is equivalent to that in the damaged configuration; that is, damage modifies the elastic behavior solely through effective stress, as noted by Lemaitre (1985a). Alternatively, Simo and Ju (1987) introduced the concept of stress equivalence with effective strain, suggesting that damage alters elastic behavior due to effective strain. The concepts of effective stress and strain are fundamental in developing strain-based and stress-based elastic-plastic-damage constitutive equations, respectively. Moreover, the theoretical foundation of CDM is primarily rooted in the thermodynamic framework, and irreversible thermodynamics is the cornerstone of the science that makes the CDM a coherent theory. This field has been shaped significantly by the contributions of notable researchers, such as Brünig (2001, 2003a), Chaboche (1988a,b), Hayakawa et al. (1998), Krajcinovic (1983), Krajcinovic and Fonseka (1981), and Murakami and Ohno (1981).

Experiments are essential for verifying various proposed material models and investigating damage and fracture behavior. Most importantly, the designed experiments need to be sufficiently complex to generate a wide range of stress triaxialities, enabling the calibration of model performance under different loading conditions. Uniaxial tension, compression, and one-axis loaded shear test are extensively discussed in the literature (Brünig et al., 2008; Gao et al., 2010; Kong et al., 2023; Peng et al., 2019; Roth et al., 2018; Voyiadjis et al., 2013; Wei et al., 2022) since their simplicity and accessibility. One significant limitation of these one-axial tests is that they generate only a small range of stress triaxialities. To address this problem, both proportional and non-proportional biaxial experiments using multi-axis-loaded or biaxial cruciform specimens are proposed. Notched hollow cylinders are one of the widely used spec-

imens for generating a broad range of stress triaxialities through combined tension-torsion experiments (Barsoum and Faleskog, 2007; Cortese et al., 2016; Faleskog and Barsoum, 2013; Gao et al., 2010; Graham et al., 2012; Haltom et al., 2013; Papasidero et al., 2015 among of others). Notably, Cortese et al. (2016) performed a series of non-proportional loading by changing from tension to torsion with hollow cylindrical specimens without unloading processes before alternating the loading direction. Conversely, stocky tubular specimens (Papasidero et al., 2015) are first preloaded with tension, compression, or torsion, then unloaded, followed by subsequent reloading with different proportional loads. The resulting stress triaxialities cover a range from approximately 0 to 0.6. In addition, butterfly specimens can be subjected to either uniaxial loading or various combinations of normal and transverse loads, resulting in induced stress triaxialities ranging from -0.33 to 0.60 (Bai and Wierzbicki, 2008; Dunand and Mohr, 2011; Mohr and Henn, 2007).

Furthermore, cruciform biaxially loaded specimens represent another effective method for generating complex stress states, making them a valuable method for the study of metal sheets (Brünig et al., 2015; Demmerle and Boehler, 1993; Gerke et al., 2017; Hou et al., 2022; Kulawinski et al., 2011; Kuwabara, 2007; Müller and Pöhlandt, 1996; Raj et al., 2022; Zillmann et al., 2015). Based on experimental and numerical analyses, the XO- and H-specimens proposed by Brünig et al. (2015) and Gerke et al. (2017) induce stress triaxialities ranging from -0.1 to 0.9 and -0.6 to 0.8, respectively. Additionally, biaxially loaded experiments also provide the opportunity for accessible non-proportional loading. For instance, utilizing biaxially loaded specimens, Brünig et al. (2021c) designed a series of non-proportional experiments, alternating between tension and shear, to study damage and fracture behavior. More recently, Kong et al. (2023) also conducted similar non-proportional experiments. Furthermore, Zistl et al. (2022a) extended this series of non-proportional experiments by applying large compressive preloads and shear stress states, followed by a transition to tension. A special pneumatic downholder was employed to prevent buckling in experiments dominated by compression. Their findings suggested that different preloading methods can alter the material properties, either increasing brittleness or ductility in the investigated ductile metals.

Cyclic loading significantly affects the service lifetime of engineering

structures. However, most previous studies have focused on a limited range of strain states. Limited research is available in the literature on cyclic tests conducted at large strain ranges (Algarni et al., 2019; Barlat et al., 2003; Marcadet and Mohr, 2015; Voyiadjis et al., 2012, 2013; Wei et al., 2022; Yoshida et al., 2002). Barlat et al. (2003) conducted a series of shear tests on specimens made from 3 mm thick 1050-O aluminum sheets, applying different reversal strains up to 0.22. Marcadet and Mohr (2015) explored the effect of reversal loading on fracture initiation by analyzing compression-tension experiments conducted on flat-notched specimens. Concerning experimental technique, different anti-buckling devices have been employed to prevent buckling during compressive deformation, and details of these anti-buckling devices can be found in Boger et al. (2005), Cao et al. (2009), Gerke et al. (2023), Marcadet and Mohr (2015), and Ramberg and Miller (1946).

Moreover, reverse loading histories also significantly influence damage and fracture behavior. Kanvinde and Deierlein (2007) experimentally analyzed seven types of steel subjected to low-cycle (less than 20 cycles) tests under a large strain range, revealing that micro-defects became more susceptible to coalescence or fracture at smaller void volumes in subsequent tensile cycles. A slight recovery of Young's modulus for the high-strength DIN1.6959 steel was observed by Voyiadjis et al. (2012, 2013), and they also indicated different cyclic loading patterns influence damage and fracture behavior. It is worth noting that, for ductile metals, the microstructure undergoes significant degradation during the initial cycles of cyclic loading, followed by a reduction in deterioration during the subsequent cycles until failure, as highlighted by Algarni et al. (2019). Moreover, Wei et al. (2022) performed a series of uniaxial tension-compression and shear cyclic loading tests. The scanning electron images (SEM) revealed that larger and coalesced micro-defects were more prevalent than under monotonic loading. Additionally, the corresponding numerical simulations elucidated the influence of reverse loading conditions on material behavior. One area for improvement in the mentioned one-axis cyclic experiments is the limitation in generating a broad range of stress triaxialities. Inspired by the biaxial non-proportional monotonic loading tests, both proportional and non-proportional biaxial reverse experiments were required to solve this issue.

Several experimental effects, such as the Bauschinger effect, the strength-

differential effect, and changes in hardening ratio after reverse loading, have been observed in studies of ductile metal behavior, with many researchers using different approaches to model and explain these observations. The Bauschinger effect, commonly observed in metals under cyclic loading conditions, has led to the proposal of various kinematic hardening models to accurately predict the yield surface's movement. For a detailed review of these models, please refer to Chaboche (2008). Prager's kinematic hardening model (Prager, 1955) represents a linear approach to kinematic hardening, wherein the back stress tensor is collinear with the plastic strain tensor. It is obvious that this linear-type kinematic hardening cannot capture the non-linear elastic-plastic transient behavior. Hence, Frederick and Armstrong (2007) introduced a recovery term into Prager's hardening rule, resulting in the back stress rate tensor being a combination of the plastic strain rate tensor and the back stress tensor. During the application of the Armstrong-Frederick kinematic hardening model, a shortcoming is observed in modeling the strain hardening behavior under large strains. To address this problem (Chaboche, 1986; Chaboche and Rousselier, 1983) decomposed the total back stress rate tensor into different components, combining both Armstrong-Frederick and Prager's type kinematic hardening models. Indeed, these modifications significantly enhance the accuracy of modeling the Bauschinger effect.

The strength-differential (SD) effect denotes asymmetric yielding in uniaxial tension and compression. Wei et al. (2022) noted that for the aluminum alloy EN AW 6082-T6, the compressive yield stress exceeds the tensile yield stress. This phenomenon was also observed in various other ductile aluminum alloys (Bai and Wierzbicki, 2008; Brünig et al., 2023; Holmen et al., 2017; Spitzig and Richmond, 1984; Wilson, 2002). Several pressure-sensitive asymmetric yield functions, incorporating different combinations of stress invariants, have been proposed to model the SD effect effectively. Spitzig and Richmond (1984) and Spitzig et al. (1975) developed a linear term of the first stress invariant in the von Mises yield function, akin to the Drucker-Prager (Drucker and Prager, 1952) yield condition utilized in soil mechanics. Brünig (1999a) pursued this idea to study the influence of pressure on the plastic behavior of metals, further extending it to include the third stress invariant Brünig et al. (2000). Stoughton and Yoon (2004) proposed a pressure-sensitive yield

function incorporating a non-associated plastic flow, aligning with the assumption of incompressibility in plastic deformations. Gao et al. (2011) modeled the SD effect by considering all three stress invariants under non-associated plastic flow for isotropic materials. Most recently, Brünig et al. (2023) presented Hoffmann's anisotropic, pressure-dependent yield function (Hoffman, 1967), employing a non-associated plastic flow rule to predict the plastic behavior of the aluminum alloy EN AW-2017A. The models mentioned above agree with experimental observations of uniaxial tension superimposed hydrostatic pressure, performed by Spitzig and Richmond (1984), showing only a marginal increase in plastic volume.

The change in the hardening rate effect is also widely observed and modeled in literature. Daroju et al. (2022) experimentally observed that aluminum alloys AA6016-T4 and AA7021-T79 evidently reduce the hardening ratio when comparing cyclic loading to monotonic loading cases. Wei et al. (2023b) also reported that the hardening ratio significantly changes after shear reverse loading conditions by experimentally examining the load-displacement behavior for one-axial and biaxial shear reverse tests. On the other hand, Ohno (1982) and Ohno and Kachi (1986) proposed a non-hardening concept in their cyclic plasticity model, i.e., non-isotropic strain hardening occurs in a certain plastic region after reverse loading. A governing equation for plastic strain models the evolution of the non-hardening region. Nouailhas et al. (1985) proposed additional terms for the plastic memory surface variables to predict the behavior of the plastic memory surface under a decreasing plastic strain range. Okorokov et al. (2019a,b) present a function based on the plastic strain range and previously accumulated plastic strains, including more than ten material behaviors, in their new kinematic hardening law.

1.2 Motivation

This work is primarily dedicated to addressing the gap in research regarding the investigation of ductile damage and fracture behavior in metal sheets under uniaxial and biaxial reverse loading tests, covering a wide range of stress triaxialities. To achieve this objective, the work can be divided into three main parts: experiments, material modeling and numerical analysis.

The experiments initially focused on uniaxial tension-compression and one-axis shear monotonic and cyclic tests due to their simplicity and accessibility. Moreover, uniaxial tension-compression monotonic and cyclic tests provide nearly homogeneous stress states before necking or buckling occurs, which is crucial for accurately calibrating the necessary material parameters. Importantly, these tests present a fundamental understanding of the differences between monotonic and cyclic loading and offer insights into damage mechanisms induced by micro-voids, as well as those resulting from micro-shear-cracks. Addressing buckling under compressive loads is challenging, especially for one-axis-loaded specimens with a thickness of 4 mm. The newly developed experimental technique, which incorporates using different clamping jaws and anti-buckling devices in conjunction with the DIC technique, has successfully solved the issue of avoiding or delaying buckling in one-axis experiments.

After gaining insights into damage mechanisms under one-axial cyclic loading conditions, the present work progresses towards a more central objective: designing or modifying a new biaxially loaded cruciform specimen. The newly designed or modified biaxially loaded specimen needs to meet the following requirements: (1) facilitate the easy combination of compression/tension and shear loads, (2) allow both axes to impose cyclic loads either separately or simultaneously, and (3) cover as wide a range of stress triaxialities as possible. The focus initially is on single-cycle biaxial experiments, denoting that only one axis is imposed cyclic loading, i.e., tension-compression or shear. Inspired by the non-proportional experiments (Brünig et al., 2021c; Cortese et al., 2016; Papasidero et al., 2015; Zistl et al., 2022b), the single cyclic biaxial experiments involve applying different shear, tension, or compression preloads on one of the biaxial loading axes. After reaching a predetermined magnitude, these preloads are maintained without any unloading, followed by the superimposition of cyclic loading on the perpendicular axis. Subsequently, the idea arose to perform bi-cyclic biaxial experiments, that is, imposing cyclic loading simultaneously on both axes. Different combinations of loading sequences in both axes are designed to study the damage and fracture behavior. Details of the discussed experimental program are presented in Section 4.1.

Concerning numerical modeling, it is essential to propose a constitutive model that includes the following aspects.

- The model is conceptualized as a phenomenological CDM model, adept at capturing anisotropic damage mechanisms, explicitly focusing on incorporating the effect of different stress states.

- The yield condition must consider the stress strength differential effect, the Bauschinger effect, and the changes in the hardening ratio (non-hardening effect) under shear reverse loading conditions. These factors are crucial for accurately simulating material behavior under cyclic loading.

- The proposed continuum damage model should be designed for user-friendly implementation as a user-defined material subroutine, ensuring accessibility for a broad range of users.

- The model should consistently and accurately predict material behavior across various conditions, including reproducing global load-displacement curves and local strain fields under various complex loading conditions, all while utilizing a unified set of parameters.

Given the outlined requirements, the kinematic framework developed by Brünig (2001, 2003a) has been adopted. His anisotropic damage model, which employs a stress-state-dependent damage evolution tensor, effectively models a range of damage phenomena. Moreover, previous studies by Brünig et al. (2018, 2019a, 2021b, 2019b, 2021c) have conclusively demonstrated the effectiveness of Brünig's theoretical framework in modeling and predicting the behavior of various ductile metals under both proportional and non-proportional loading conditions. However, the previous Brünig's elastic-plastic-damage model (Brünig, 2001, 2003a; Brünig et al., 2008, 2013) shows shortcomings in accurately predicting the Bauschinger effect and the non-hardening effect after shear reverse loading. Therefore, the main task of this research is to incorporate an appropriately modified isotropic-kinematic hardening model into Brünig's existing constitutive framework. Moreover, a novel kinematic hardening rule based on the damage strain rate tensor is proposed to predict the damage surface movement under cyclic loading. Finally, the modified anisotropic elastic-plastic-damage model is implemented as a user-defined subroutine in Ansys FEM commercial software (Ansys, Inc., 2013). The numerical integration utilizes the plastic predictor-elastic corrector approach in undamaged configurations and the inelastic (plastic-damage) predictor-elastic corrector method in damaged configurations.

1.3 Outline

This thesis is structured as follows. Chapter 2 briefly recalls the kinematic framework proposed by Brünig (2001, 2003a) and discusses the plastic yield condition with modified isotropic-kinematic hardening, as well as the damage condition, incorporating a combined softening law. Chapter 3 describes the numerical integration method for the proposed elastic-plastic-damage model. Chapter 4 provides a detailed discussion of the experimental setups, including the novel design of experimental specimens, DIC settings, and numerical setup, encompassing the numerical model and parameter identification approach. Chapter 5 describes a comparison of experimental and numerical results, including the global load-displacement curves and local strain fields. Additionally, a comprehensive understanding of the occurrence and development of damage is discussed in this chapter, based on numerical damage strains, stress states, SEM images, and fracture pictures. Chapter 6 concludes the thesis, presenting a summary of the findings and providing outlooks for future research directions.

2 Constitutive modeling

Wei et al. (2022) performed uniaxial tensile tests under loading and reloading conditions, and the stress-strain curve is shown in Fig. 2.1(a). It can be observed that Young's modulus E reduces during the loading and unloading processes due to the damage. To characterize the elastic-plastic-damage behavior, Brünig (2001, 2003a) proposed an advanced phenomenological elastic-plastic-damage continuum model. A schematic picture is illustrated in Fig. 2.1(b) in terms of the load-displacement curve for the monotonic uniaxial tensile test. Following his idea, the
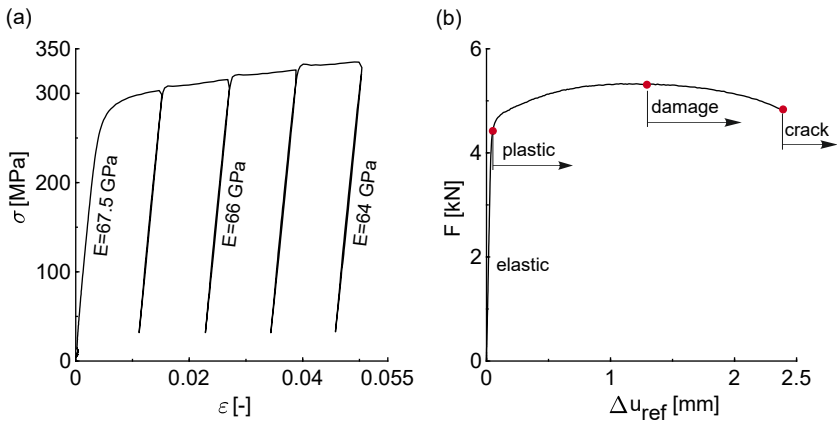
Figure 2.1: (a) Changes in Young's modulus E under tensile loading and unloading conditions, (b) the load-displacement curve for the uniaxial monotonic tensile test. Experimental data are cited from Wei et al. (2022).

material has elastic behavior until plastic yielding, and the plastic yield condition characterizes the onset of the plastic behavior. The plastic flow rule models the evolution of inelastic strains due to plastic behavior. Similarly, the same approach is used to describe damage. The damage

condition captures the onset of damage and the evolution of further inelastic strains governed by the damage strain rate tensor. When damage reaches a critical value, macro-cracks will begin to form.

Moreover, scanning electron microscopy (SEM) images of the fractured surfaces for the monotonic tensile and shear test show significantly different damage mechanics, as reported by Wei et al. (2022). As shown in Fig. 2.2, the micro-voids are visible on the fractured surface after monotonic tensile test, whereas the micro-shear-cracks predominate on the fractured surface after shear test. These findings confirmed that the damage and fracture behaviors show an anisotropic and stress-state-dependent response of the investigated ductile aluminum alloy. Thus, the anisotropic damage characteristics should be taken into account in the realistic material model.

(a) Uniaxial tension   (b) Shear
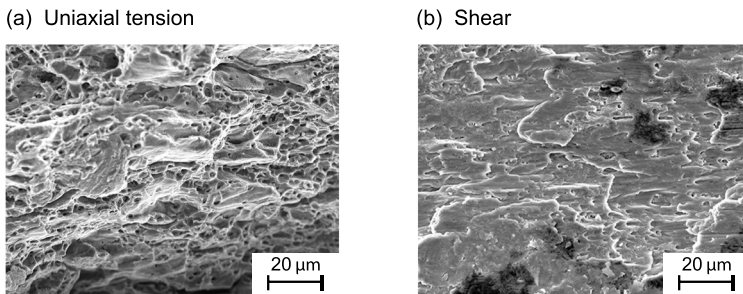
Figure 2.2: SEM images of the fractured surfaces for the uniaxial tension test (a) and shear test (b). The SEM pictures are cited from Wei et al. (2022).

To develop the above-mentioned phenomenological elastic-plastic-damage continuum model, Brünig (2001, 2003a) introduced a second-order damage strain rate tensor into the damage configurations to model the large inelastic deformations caused by micro-defects, whereas effective fictitious undamaged configurations characterize only elastic-plastic behavior. The relations between the damaged configurations and fictitious undamaged configurations are based on damage tensors. Moreover, the metric transformation tensor and the effective metric transformation tensor are used to characterize the deformations between the reference and

current configurations in the damaged configurations and undamaged configurations, respectively. In contrast to the approach of decomposing the deformation gradient tensor (Lee, 1969), the proposed continuum formulation is based on the multiplicatively decomposed (effective) metric transformation tensors into an inelastic and an elastic part in different configurations.

To characterize the material behavior under cyclic loading more accurately, in addition to the continuum model proposed by Brünig (2003a), the following modifications have been made.

- The strain triaxialities (Wei et al., 2022) and strain Lode parameter are newly proposed (Wei et al., 2023b) to distinguish between stress/strain states in monotonic and cyclic loading paths, as well as different cyclic loading patterns.

- For the cyclic plasticity model, Wei et al. (2022) incorporated the isotropic-kinematic combined hardening law into the Drucker-Prager-type yield criterion to capture the strength-differential (SD) and Bauschinger effects. Moreover, a newly proposed method by Wei et al. (2023b) provides a straightforward approach to characterize the change in the hardening ratio after shear reverse loading conditions.

- For the cyclic damage model, a novel kinematic softening material model based on the damage strain rate tensor is proposed by Wei et al. (2023b) to characterize the translation of the damage surface.

2.1 Kinematic framework

In this section, the kinematic framework proposed by Brünig (2001, 2003a) is briefly summarized. In the damaged configurations, basis vectors and metric coefficients for the initial undeformed configuration $\mathring{\mathcal{B}}$, the intermediate configuration $\overset{*}{\mathcal{B}}$ and the plastically deformed and damaged configuration $\mathcal{B}$ are given by

$$\mathring{G}_{ij} = \mathring{\mathbf{g}}_i \cdot \mathring{\mathbf{g}}_j \,, \quad \overset{*}{G}_{ij} = \overset{*}{\mathbf{g}}_i \cdot \overset{*}{\mathbf{g}}_j \,, \quad \text{and} \quad G_{ij} = \mathbf{g}_i \cdot \mathbf{g}_j \,, \tag{2.1}$$

respectively.

The macroscopic behavior of elastic-plastic-damage materials under large

deformations is formulated based on the mixed-variant metric transformation tensor

$$\mathbf{Q} = Q^{i}_{.j}\mathbf{g}_i \otimes \mathbf{g}^j = \mathring{G}_{ik}G^{kj}\mathbf{g}_i \otimes \mathbf{g}^j = \mathbf{F}\mathbf{F}^{\mathrm{T}} \, , \qquad (2.2)$$

where $\mathbf{F}$ is the deformation gradient tensor. It can be multiplicatively decomposed as:

$$\mathbf{Q} = Q^{i}_{.j}\mathbf{g}_i \otimes \mathbf{g}^j = \mathbf{F}\mathbf{F}^{\mathrm{T}} = \mathbf{Q}^{\mathrm{pd}}\mathbf{Q}^{\mathrm{el}} \qquad (2.3)$$

with $\mathbf{Q}^{\mathrm{pd}}$ and $\mathbf{Q}^{\mathrm{el}}$ representing the inelastic (plastic-damage) and the elastic part of the metric transformation tensor, respectively, as illustrated in Fig. 2.3.
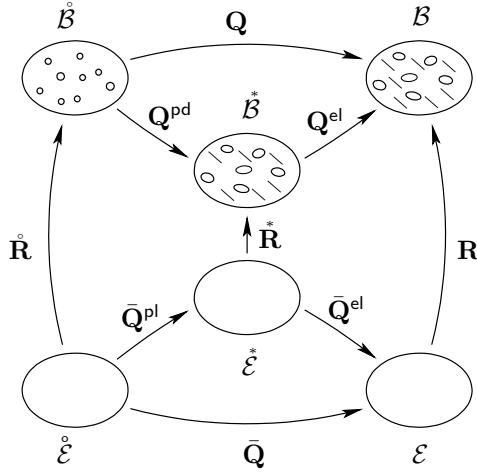
Figure 2.3: Configurations and metric transformation tensors: $\mathring{\mathcal{B}}$ – reference configuration in the damaged configurations, $\overset{*}{\mathcal{B}}$ and $\mathcal{B}$ – current configurations in the damaged configurations, $\mathring{\mathcal{E}}$ – reference configuration in the effective fictitious undamaged configurations, and $\overset{*}{\mathcal{E}}$ and $\mathcal{E}$ – current configurations in the effective fictitious undamaged configurations, see original image Brünig (2003a) and Wei et al. (2024b).

Moreover, the logarithmic Hencky strain tensor is expressed in the form

$$\mathbf{A} = A^i_{.j}\mathbf{g}_i \otimes \mathbf{g}^j = \frac{1}{2}\ln\mathbf{Q}\,, \tag{2.4}$$

and the elastic part of the logarithmic Hencky strain is defined as

$$\mathbf{A}^{\mathrm{el}} = (A^{\mathrm{el}})^i_{.j}\mathbf{g}_i \otimes \mathbf{g}^j = \frac{1}{2}\ln\mathbf{Q}^{\mathrm{el}}\,. \tag{2.5}$$

In addition, the strain rate tensor

$$\begin{aligned}
\dot{\mathbf{H}} = \dot{H}^i_{.j}\mathbf{g}_i \otimes \mathbf{g}^j = \frac{1}{2}\mathbf{Q}^{-1}\dot{\mathbf{Q}} =& \frac{1}{2}\mathbf{Q}^{\mathrm{el}-1}\mathbf{Q}^{\mathrm{pd}-1}\dot{\mathbf{Q}}^{\mathrm{pd}}\mathbf{Q}^{\mathrm{el}} \\
&+ \frac{1}{2}\mathbf{Q}^{\mathrm{el}-1}\dot{\mathbf{Q}}^{\mathrm{el}} = \dot{\mathbf{H}}^{\mathrm{pd}} + \dot{\mathbf{H}}^{\mathrm{el}}
\end{aligned} \tag{2.6}$$

is additively decomposed into the inelastic, $\dot{\mathbf{H}}^{\mathrm{pd}}$, and the elastic part, $\dot{\mathbf{H}}^{\mathrm{el}}$.

The effective fictitious undamaged configurations are introduced to characterize the pure elastic-plastic material behavior, similar to Betten (1982, 1983), Murakami and Ohno (1981), Voyiadjis and Kattan (1992), and Voyiadjis and Park (1999). Furthermore, the second-order initial damage tensor $\mathring{\mathbf{R}}$, and the current damage tensors $\mathbf{R}$ and $\overset{*}{\mathbf{R}}$ are addressed to describe the damage transformation respective to the damage configurations and the effective fictitious undamaged configurations, see Fig. 2.3. The significant advantage of the proposed approaches is that they simplify the complexity of the kinematic equations compared to the classical theory based on multiplicative decomposition of the total deformation gradient tensor (see, e.g., Voyiadjis and Park (1999)).

The basis vectors and metric coefficients for the initial undeformed undamaged configuration $\mathring{\mathcal{E}}$, the intermediate undamaged configuration $\overset{*}{\mathcal{E}}$ and the current undamaged configuration $\mathcal{E}$ are given by

$$\mathring{E}_{ij} = \mathring{\mathbf{e}}_i \cdot \mathring{\mathbf{e}}_j\,, \quad \overset{*}{E}_{ij} = \overset{*}{\mathbf{e}}_i \cdot \overset{*}{\mathbf{e}}_j\,, \quad \text{and} \quad E_{ij} = \mathbf{e}_i \cdot \mathbf{e}_j\,, \tag{2.7}$$

respectively. Moreover, the damage deformation gradient

$$\tilde{\mathbf{F}} = \mathbf{g}_i \otimes \mathbf{e}^i\,, \tag{2.8}$$

is used to transform the undeformed kinematic variables into the current damaged configuration $\mathcal{B}$.

In addition, the effective metric transformation tensor can be multiplicatively decomposed as

$$\bar{\mathbf{Q}} = \tilde{\mathbf{F}}(\bar{Q}^i_{.j}\mathbf{e}_i \otimes \mathbf{e}^j)\tilde{\mathbf{F}}^{-1} = \bar{Q}^i_{.j}\mathbf{g}_i \otimes \mathbf{g}^j = \bar{\mathbf{Q}}^{\mathrm{pl}}\bar{\mathbf{Q}}^{\mathrm{el}}\,, \tag{2.9}$$

where $\bar{\mathbf{Q}}^{\mathrm{pl}}$ and $\bar{\mathbf{Q}}^{\mathrm{el}}$ are the plastic and the elastic part of the effective metric transformation tensor, respectively. Moreover, the effective logarithmic strain tenor is given by

$$\bar{\mathbf{A}} = \bar{A}^i_{.j}\mathbf{g}_i \otimes \mathbf{g}^j = \frac{1}{2}\ln\bar{\mathbf{Q}}\,, \tag{2.10}$$

and the effective logarithmic elastic strain tenor is expressed as

$$\bar{\mathbf{A}}^{\mathrm{el}} = (\bar{A}^{\mathrm{el}})^i_{.j}\mathbf{g}_i \otimes \mathbf{g}^j = \frac{1}{2}\ln\bar{\mathbf{Q}}^{\mathrm{el}}\,. \tag{2.11}$$

In addition, the rate of the effective strain tensor

$$\begin{aligned}
\dot{\bar{\mathbf{H}}} = \dot{\bar{H}}^i_{.j}\mathbf{g}_i \otimes \mathbf{g}^j = \frac{1}{2}\bar{\mathbf{Q}}^{-1}\dot{\bar{\mathbf{Q}}} &= \frac{1}{2}\bar{\mathbf{Q}}^{\mathrm{el}-1}\bar{\mathbf{Q}}^{\mathrm{pl}-1}\dot{\bar{\mathbf{Q}}}^{\mathrm{pl}}\bar{\mathbf{Q}}^{\mathrm{el}} \\
&+ \frac{1}{2}\bar{\mathbf{Q}}^{\mathrm{el}-1}\dot{\bar{\mathbf{Q}}}^{\mathrm{el}} = \dot{\bar{\mathbf{H}}}^{\mathrm{pl}} + \dot{\bar{\mathbf{H}}}^{\mathrm{el}}
\end{aligned} \tag{2.12}$$

can be additively decomposed into plastic and elastic part.

Following Brünig (2001, 2003a), the explicit characterization of damage kinematics is achieved through the utilization of metric transformations and corresponding logarithmic strain measures. As shown in Fig. 2.3, the damage metric transformation tensors ($\mathbf{R}$, $\overset{*}{\mathbf{R}}$, and $\overset{\circ}{\mathbf{R}}$) describe the kinematic connections the effective undamaged configurations and damaged configurations. They are defined as

$$\overset{\circ}{\mathbf{R}}_{ij} = \overset{\circ}{R}{}^i_{.j}\mathbf{g}_i\otimes\mathbf{g}^j\,, \quad \overset{*}{\mathbf{R}}_{ij} = \overset{*}{R}{}^i_{.j}\mathbf{g}_i\otimes\mathbf{g}^j\,, \quad \text{and} \quad \mathbf{R}_{ij} = R^i_{.j}\mathbf{g}_i\otimes\mathbf{g}^j\,, \tag{2.13}$$

respectively. Compared to the damage tensor $\overset{\circ}{\mathbf{R}}$ corresponding to the initial damage and $\mathbf{R}$ associated with the current damage, the current damage tensor $\overset{*}{\mathbf{R}}$ solely describes the kinematic deformation of the dam-

age. Thus, the damage strain tensor is defined as

$$\mathbf{A}^{\mathrm{da}} = (A^{\mathrm{da}})^i_{.j}\mathbf{g}_i \otimes \mathbf{g}^j = \frac{1}{2}\ln\overset{*}{\mathbf{R}}, \tag{2.14}$$

and the rate of the damage strain tenor is given by

$$\dot{\mathbf{H}}^{\mathrm{da}} = (\dot{H}^{\mathrm{da}})^i_{.j}\mathbf{g}_i \otimes \mathbf{g}^j = \frac{1}{2}\overset{*}{\mathbf{R}}^{-1}\dot{\overset{*}{\mathbf{R}}}. \tag{2.15}$$

Furthermore, as illustrated in Fig. 2.3, the kinematic relation between the current damage tensor $\mathbf{R}$ and $\overset{*}{\mathbf{R}}$ is depicted as

$$\mathbf{R} = R^i_{.j}\mathbf{g}_i \otimes \mathbf{g}^j = \bar{\mathbf{Q}}^{\mathrm{el}-1}\overset{*}{\mathbf{R}}\mathbf{Q}^{\mathrm{el}}, \tag{2.16}$$

and the metric transformation tensor $\mathbf{Q}$ can be also decomposed in the form of

$$\mathbf{Q} = \overset{\circ}{\mathbf{R}}^{-1}\bar{\mathbf{Q}}^{\mathrm{pl}}\overset{*}{\mathbf{R}}\mathbf{Q}^{\mathrm{el}}. \tag{2.17}$$

Substituting Eqs. (2.15), (2.16), and (2.17) into Eq. (2.6), one gets

$$\dot{\mathbf{H}} = \dot{\mathbf{H}}^{\mathrm{el}} + \mathbf{R}^{-1}\dot{\mathbf{H}}^{\mathrm{pl}}\mathbf{R} + \mathbf{Q}^{\mathrm{el}-1}\dot{\mathbf{H}}^{\mathrm{da}}\mathbf{Q}^{\mathrm{el}}. \tag{2.18}$$

It is worth noting that the (effective) elastic strain rate tensors in the effective fictitious undamaged and damage configurations are assumed to be the same as discussed by Brünig (2001, 2003a) ($\dot{\bar{\mathbf{H}}}^{\mathrm{el}} = \dot{\mathbf{H}}^{\mathrm{el}}$), resulting in $\mathbf{A}^{\mathrm{el}} = \bar{\mathbf{A}}^{\mathrm{el}}$.

2.2 Thermodynamic considerations

The effective fictitious undamaged configurations characterize solely the elastic-plastic deformations. The rate of the effective specific mechanical work is defined as

$$\rho_0\dot{w} = \bar{\mathbf{T}} \cdot \dot{\bar{\mathbf{H}}}, \tag{2.19}$$

where ρ_0 represents the initial mass density and $\bar{\mathbf{T}}$ is the effective Kirchhoff stress tensor.

Making use of the Eq. (2.12), the effective mechanical work $\dot{\bar{w}}$ can be additively decomposed

$$
\begin{aligned}
\rho_0 \dot{\bar{w}} &= \rho_0 \dot{\bar{w}}^{\mathrm{el}} + \rho_0 \dot{\bar{w}}^{\mathrm{pl}} \\
&= \bar{\mathbf{T}} \cdot \dot{\bar{\mathbf{H}}}^{\mathrm{el}} + \bar{\mathbf{T}} \cdot \dot{\bar{\mathbf{H}}}^{\mathrm{pl}}
\end{aligned}
\tag{2.20}
$$

into an effective elastic part $\dot{\bar{w}}^{\mathrm{el}}$ and an effective plastic part $\dot{\bar{w}}^{\mathrm{pl}}$.

Moreover, the specific effective Helmholtz free energy $\bar{\psi}$ is introduced in the effective fictitious undamaged configurations. It is additively separable into an effective elastic $\bar{\psi}^{\mathrm{el}}$ and an effective plastic part $\bar{\psi}^{\mathrm{pl}}$

$$
\bar{\psi} = \bar{\psi}^{\mathrm{el}}(\bar{\mathbf{A}}^{\mathrm{el}}) + \bar{\psi}^{\mathrm{pl}}(\gamma) \, ,
\tag{2.21}
$$

where $\bar{\mathbf{A}}^{\mathrm{el}}$ denotes the effective elastic strain tensor (2.11) and γ is the equivalent plastic strain.

In addition, the second law of thermodynamics must be fulfilled to derive the consistent state relations of the elastic-plastic model in the effective fictitious undamaged configurations. The associated Clausius-Duhem inequality is given by

$$
\dot{\bar{w}} - \dot{\bar{\psi}} \geq 0 \, .
\tag{2.22}
$$

Taking Eqs. (2.20) and (2.21) into account, Eq. (2.22) can be rewritten as

$$
\bar{\mathbf{T}} \cdot \dot{\bar{\mathbf{H}}}^{\mathrm{el}} + \bar{\mathbf{T}} \cdot \dot{\bar{\mathbf{H}}}^{\mathrm{pl}} - \rho_0 \frac{\partial \bar{\psi}^{\mathrm{el}}}{\partial \bar{\mathbf{A}}^{\mathrm{el}}} \cdot \dot{\bar{\mathbf{A}}}^{\mathrm{el}} - \rho_0 \frac{\partial \bar{\psi}^{\mathrm{pl}}}{\partial \gamma} \dot{\gamma} \geq 0 \, .
\tag{2.23}
$$

Considering non-dissipative processes within the effective elastic range, it results in

$$
\bar{\mathbf{T}} \cdot \dot{\bar{\mathbf{H}}}^{\mathrm{el}} - \rho_0 \frac{\partial \bar{\psi}^{\mathrm{el}}}{\partial \bar{\mathbf{A}}^{\mathrm{el}}} \cdot \dot{\bar{\mathbf{A}}}^{\mathrm{el}} = 0 \, .
\tag{2.24}
$$

Taking into account the following assumption (Brünig, 2003a)

$$
\bar{\mathbf{T}} \cdot \dot{\bar{\mathbf{H}}}^{\mathrm{el}} = \bar{\mathbf{T}} \cdot \dot{\bar{\mathbf{A}}}^{\mathrm{el}} \, ,
\tag{2.25}
$$

and thus, based on Eq. (2.24), the effective Kirchhoff stress is given by

$$\bar{\mathbf{T}} = \rho_0 \frac{\partial \bar{\psi}^{\mathrm{el}}}{\partial \bar{\mathbf{A}}^{\mathrm{el}}} \,. \tag{2.26}$$

In addition, the remaining Kelvin inequality is given by

$$\bar{\mathbf{T}} \cdot \dot{\bar{\mathbf{H}}}^{\mathrm{pl}} - \rho_0 \frac{\partial \bar{\psi}^{\mathrm{pl}}}{\partial \gamma} \dot{\gamma} \geq 0 \,, \tag{2.27}$$

where the effective plastic strain rate tensor $\dot{\bar{\mathbf{H}}}^{\mathrm{pl}}$ governs the evolution of the effective plastic deformations.

In the context of damage configurations, following Eqs. (2.19) and (2.20), the rate of the specific mechanical work w is additively split of an elastic part ($\dot{w}^{\mathrm{el}}$), a plastic part ($\dot{w}^{\mathrm{pl}}$), and a damage part ($\dot{w}^{\mathrm{da}}$), i.e.,

$$\rho_0 \dot{w} = \rho_0 \dot{w}^{\mathrm{el}} + \rho_0 \dot{w}^{\mathrm{pl}} + \rho_0 \dot{w}^{\mathrm{da}} = \mathbf{T} \cdot \dot{\mathbf{H}} \,. \tag{2.28}$$

Masking use of the Eq. (2.18), one arrives at

$$\begin{aligned}
\rho_0 \dot{w}^{\mathrm{el}} &+ \rho_0 \dot{w}^{\mathrm{pl}} + \rho_0 \dot{w}^{\mathrm{da}} \\
&= \mathbf{T} \cdot \dot{\mathbf{H}}^{\mathrm{el}} + \mathbf{T} \cdot (\mathbf{R}^{-1} \dot{\mathbf{H}}^{\mathrm{pl}} \mathbf{R}) + \mathbf{T} \cdot (\mathbf{Q}^{\mathrm{el}-1} \dot{\mathbf{H}}^{\mathrm{da}} \mathbf{Q}^{\mathrm{el}}) \,.
\end{aligned} \tag{2.29}$$

In the framework by Brünig (2001, 2003a), plastic flow and damage lead to permanent deformations. In addition, as demonstrated in Fig. 2.1(a), micro-defect deformations evidently reduce Young's modulus. It is highlighted that damage also affects elastic behavior but not plastic deformations. Consistent with the assumptions made in Lemaitre (1985a) and Lu and Chow (1990), plastic flow and damage processes are considered to be independent. Thus, the Helmholtz free energy ψ is assumed to be an additive combination of an elastic part ψ^{el}, a plastic part ψ^{pl}, and a damage part ψ^{da}

$$\psi = \psi^{\mathrm{el}}(\mathbf{A}^{\mathrm{el}}, \mathbf{A}^{\mathrm{da}}) + \psi^{\mathrm{pl}}(\gamma) + \psi^{\mathrm{da}}(\mu) \,. \tag{2.30}$$

The elastic part of free energy ψ^{el} only depends on the elastic strain tensor $\mathbf{A}^{\mathrm{el}}$ and the damage strain tensor $\mathbf{A}^{\mathrm{da}}$, modeling the elastic response of the damaged material in the damage configurations. In addition, the

plastic part of the free energy ψ^{pl} characterizes the plastic flow in terms of the plastic internal variable γ. In contrast, the damage part of the free energy ψ^{da} describes the evolution of damage and depends on the equivalent damage strain μ.

From which the second law of the thermodynamics the Clausius-Duhem inequality is given by

$$
\begin{aligned}
&\mathbf{T} \cdot \dot{\mathbf{H}}^{\mathrm{el}} + (\mathbf{R}\mathbf{T}\mathbf{R}^{-1}) \cdot \dot{\bar{\mathbf{H}}}^{\mathrm{pl}} + (\mathbf{Q}^{\mathrm{el}}\mathbf{T}\mathbf{Q}^{\mathrm{el}-1}) \cdot \dot{\mathbf{H}}^{\mathrm{da}} \\
&- \rho_0 \frac{\partial \psi^{\mathrm{el}}}{\partial \mathbf{A}^{\mathrm{el}}} \cdot \dot{\mathbf{A}}^{\mathrm{el}} - \rho_0 \frac{\partial \psi^{\mathrm{el}}}{\partial \mathbf{A}^{\mathrm{da}}} \cdot \dot{\mathbf{A}}^{\mathrm{da}} - \rho_0 \frac{\partial \psi^{\mathrm{pl}}}{\partial \gamma}\dot{\gamma} - \rho_0 \frac{\partial \psi^{\mathrm{da}}}{\partial \mu}\dot{\mu} \geq 0\,.
\end{aligned} \tag{2.31}
$$

According to the non-dissipative processes within the elastic range, one gets

$$
\mathbf{T} \cdot \dot{\mathbf{H}}^{\mathrm{el}} - \rho_0 \frac{\partial \psi^{\mathrm{el}}}{\partial \mathbf{A}^{\mathrm{el}}} \cdot \dot{\mathbf{A}}^{\mathrm{el}} = 0\,. \tag{2.32}
$$

Following the assumption (Brünig, 2003a)

$$
\mathbf{T} \cdot \dot{\mathbf{H}}^{\mathrm{el}} = \mathbf{T} \cdot \dot{\mathbf{A}}^{\mathrm{el}}\,, \tag{2.33}
$$

one gets

$$
\mathbf{T} = \rho_0 \frac{\partial \psi^{\mathrm{el}}}{\partial \mathbf{A}^{\mathrm{el}}}\,. \tag{2.34}
$$

Moreover, the remaining dissipation inequality is decomposed into a plastic part

$$
(\mathbf{R}\mathbf{T}\mathbf{R}^{-1}) \cdot \dot{\bar{\mathbf{H}}}^{\mathrm{pl}} - \rho_0 \frac{\partial \psi^{\mathrm{pl}}}{\partial \gamma}\dot{\gamma} \geq 0\,, \tag{2.35}
$$

and a damage part

$$
(\mathbf{Q}^{\mathrm{el}}\mathbf{T}\mathbf{Q}^{\mathrm{el}-1}) \cdot \dot{\mathbf{H}}^{\mathrm{da}} - \rho_0 \frac{\partial \psi^{\mathrm{el}}}{\partial \mathbf{A}^{\mathrm{da}}} \cdot \dot{\mathbf{A}}^{\mathrm{da}} - \rho_0 \frac{\partial \psi^{\mathrm{da}}}{\partial \mu}\dot{\mu} \geq 0\,. \tag{2.36}
$$

It should be noted that the effective plastic strain rate $\dot{\bar{\mathbf{H}}}^{\mathrm{pl}}$ based on the plastic potential function $\bar{\psi}^{\mathrm{pl}}$ needs only to enforce Eq. (2.27). The

second damage dissipation may lead to restrictions in formulating the elastic part of the free energy ψ^{el} and in choosing the damage material parameters. Moreover, it is evident that the evolution equation for the damage part of the deformation is expressed in terms of the damage strain rate tensor $\dot{\mathbf{H}}^{\mathrm{da}}$, as shown in Eq. (2.36).

2.3 Elastic laws and stress and strain states

2.3.1 Elastic laws in damaged and undamaged configurations

In effective fictitious undamaged configurations, the effective elastic part of the Helmholtz free energy

$$\rho_0 \dot{\bar{\psi}}^{\mathrm{el}}(\bar{\mathbf{A}}^{\mathrm{el}}) = G\bar{\mathbf{A}}^{\mathrm{el}} \cdot \bar{\mathbf{A}}^{\mathrm{el}} + \frac{1}{2}\left(K - \frac{2}{3}G\right)(\operatorname{tr}\bar{\mathbf{A}}^{\mathrm{el}})^2 \tag{2.37}$$

is formulated in terms of the effective logarithmic elastic strain tensor $\bar{\mathbf{A}}^{\mathrm{el}}$ (2.11), the shear modulus G, and the bulk modulus K. Thus, based on Eq. (2.26), the effective Kirchhoff stress is given by

$$\begin{aligned}
\bar{\mathbf{T}} &= \rho_0 \frac{\partial \bar{\psi}^{\mathrm{el}}}{\partial \bar{\mathbf{A}}^{\mathrm{el}}} \\
&= 2G\bar{\mathbf{A}}^{\mathrm{el}} + \left(K - \frac{2}{3}G\right)\operatorname{tr}\bar{\mathbf{A}}^{\mathrm{el}}\mathbf{1}\,,
\end{aligned} \tag{2.38}$$

where $\mathbf{1}$ is the second-order unit tensor.

Furthermore, the elastic part of the free energy in the damaged configuration is defined as

$$\begin{aligned}
\rho_0 \psi^{\mathrm{el}}(\mathbf{A}^{\mathrm{el}}, \mathbf{A}^{\mathrm{da}}) = {}& G\mathbf{A}^{\mathrm{el}} \cdot \mathbf{A}^{\mathrm{el}} + \frac{1}{2}(K - \frac{2}{3}G)(\operatorname{tr}\mathbf{A}^{\mathrm{el}})^2 \\
&+ \eta_1 \operatorname{tr}\mathbf{A}^{\mathrm{da}}(\operatorname{tr}\mathbf{A}^{\mathrm{el}})^2 + \eta_2 \operatorname{tr}\mathbf{A}^{\mathrm{da}}\mathbf{A}^{\mathrm{el}} \cdot \mathbf{A}^{\mathrm{el}} \\
&+ \eta_3 \operatorname{tr}\mathbf{A}^{\mathrm{el}}\mathbf{A}^{\mathrm{da}} \cdot \mathbf{A}^{\mathrm{el}} + \eta_4 \mathbf{A}^{\mathrm{el}} \cdot (\mathbf{A}^{\mathrm{el}}\mathbf{A}^{\mathrm{da}})
\end{aligned} \tag{2.39}$$

with the damaged parameters $\eta_1...\eta_4$ to describe the deterioration of the elastic properties induced by the micro-defects (Brünig, 2003a; Brünig and Michalski, 2017; Hayakawa et al., 1998).

Taking into account Eq. (2.34), the Kirchhoff stress can be obtained

$$
\begin{aligned}
\mathbf{T} &= \rho_0 \frac{\partial \psi^{\mathrm{el}}}{\partial \mathbf{A}^{\mathrm{el}}} \\
&= 2(G + \eta_2 \operatorname{tr} \mathbf{A}^{\mathrm{da}})\mathbf{A}^{\mathrm{el}} + (K - \frac{2}{3}G + 2\eta_1 \operatorname{tr} \mathbf{A}^{\mathrm{da}}) \operatorname{tr} \mathbf{A}^{\mathrm{el}}\mathbf{1} \\
&\quad + \eta_3(\mathbf{A}^{\mathrm{da}} \cdot \mathbf{A}^{\mathrm{el}})\mathbf{1} + \eta_3 \operatorname{tr} \mathbf{A}^{\mathrm{el}}\mathbf{A}^{\mathrm{da}} + \eta_4(\mathbf{A}^{\mathrm{el}}\mathbf{A}^{\mathrm{da}} + \mathbf{A}^{\mathrm{da}}\mathbf{A}^{\mathrm{el}}) \,.
\end{aligned}
\tag{2.40}
$$

2.3.2 State variables

In the continuum damage and fracture community, the stress invariants I_1 and J_2, the stress triaxiality η, and the stress Lode parameter ω are widely used to characterize the stress states, such as Bai and Wierzbicki (2008), Brünig et al. (2008), Gao et al. (2010), and Lou et al. (2020). In addition, Wei et al. (2023b, 2022) suggested adding the strain invariants (I_1^{el}, J_2^{el}, I_1^{A}, and J_2^{A}), strain triaxialities (η_{el} and η_{A}), and strain Lode parameters (ω_{el} and ω_{A}) together with stress state variables (I_1, J_2, η, and ω) to better distinguish the stress and strain state between multi-axis loaded monotonic and cyclic loading conditions. The invariants based on stress and strain fields are summarized as

$$
\begin{aligned}
I_1 &= \operatorname{tr} \mathbf{T}, \quad \text{and} \quad J_2 = \frac{1}{2} \operatorname{dev} \mathbf{T} \cdot \operatorname{dev} \mathbf{T} \,, \\
I_1^{\mathrm{el}} &= \operatorname{tr} \mathbf{A}^{\mathrm{el}}, \quad \text{and} \quad J_2^{\mathrm{el}} = \frac{1}{2} \operatorname{dev} \mathbf{A}^{\mathrm{el}} \cdot \operatorname{dev} \mathbf{A}^{\mathrm{el}} \,, \\
I_1^{\mathrm{A}} &= \operatorname{tr} \mathbf{A}, \quad \text{and} \quad J_2^{\mathrm{A}} = \frac{1}{2} \operatorname{dev} \mathbf{A} \cdot \operatorname{dev} \mathbf{A} \,,
\end{aligned}
\tag{2.41}
$$

respectively, where $\mathbf{A}$ is total strain tensor (2.4).

With stress and strain invariants in hand, the stress or strain triaxialities are expressed as

$$
\begin{aligned}
\eta &= \frac{\sigma_{\mathrm{m}}}{\sigma_{\mathrm{eq}}} = \frac{I_1}{3\sqrt{3J_2}} \,, \\
\eta_{\mathrm{el}} &= \frac{\varepsilon_{\mathrm{vol}}^{\mathrm{el}}}{\varepsilon_{\mathrm{eq}}^{\mathrm{el}}} = \frac{I_1^{\mathrm{el}}}{\sqrt{3J_2^{\mathrm{el}}}} \,, \quad \text{and} \quad \eta_{\mathrm{A}} = \frac{\varepsilon_{\mathrm{vol}}}{\varepsilon_{\mathrm{eq}}} = \frac{I_1^{\mathrm{A}}}{\sqrt{3J_2^{\mathrm{A}}}} \,,
\end{aligned}
\tag{2.42}
$$

where σ_{m} is the mean stress, $\varepsilon^{\mathrm{el}}_{\mathrm{vol}}$ and $\varepsilon_{\mathrm{vol}}$ are the volumetric parts of the elastic and total strain tensors, respectively, as well as σ_{eq}, $\varepsilon^{\mathrm{el}}_{\mathrm{eq}}$, and $\varepsilon_{\mathrm{eq}}$ are the von Mises equivalent stress and elastic and total equivalent strains, respectively.

The stress Lode parameter

$$\omega = \frac{2T_2 - T_1 - T_3}{T_1 - T_3} \quad \text{with} \quad T_1 \geq T_2 \geq T_3 , \tag{2.43}$$

and elastic and total strain Lode parameters

$$\begin{aligned} \omega_{\mathrm{el}} &= \frac{2A^{\mathrm{el}}_2 - A^{\mathrm{el}}_1 - A^{\mathrm{el}}_3}{A^{\mathrm{el}}_1 - A^{\mathrm{el}}_3} \quad \text{with} \quad A^{\mathrm{el}}_1 \geq A^{\mathrm{el}}_2 \geq A^{\mathrm{el}}_3 \\ \omega_{\mathrm{A}} &= \frac{2A_2 - A_1 - A_3}{A_1 - A_3} \quad \text{with} \quad A_1 \geq A_2 \geq A_3 \end{aligned} \tag{2.44}$$

are defined with the principal stresses T_i and principal elastic, A^{el}_i, and total strains, A_i ($i = 1...3$), respectively.

2.4 Isotropic plasticity with combined hardening

Wei et al. (2022) observed that the compressive yield stresses are higher than the tensile yield stresses from the monotonic uniaxial tension and compression experiments for the investigated aluminum alloy EN-AW 6082-T6. This experimental strength-differential effect (SD effect) was also reported by Spitzig and Richmond (1984), Holmen et al. (2017), and Brünig et al. (2023). Furthermore, the Bauschinger effect was detected particularly during the reverse loading experiments. In addition, in the case of proportional or non-proportional shear reverse loading, the change in the hardening ratio can be obviously observed in experimental load-displacement curves (Wei et al., 2023b). The material model, which takes into account the SD effect, the Bauschinger effect, and the effect of hardening ratio changes, is comprehensively summarized in this section.

Furthermore,   the   hydrostatic-stress-dependent   Drucker-Prager-type

yield criterion with combined hardening

$$
\begin{aligned}
f^{\mathrm{pl}} &= \sqrt{\frac{1}{2}\operatorname{dev}(\bar{\mathbf{T}}-\bar{\boldsymbol{\alpha}})\cdot\operatorname{dev}(\bar{\mathbf{T}}-\bar{\boldsymbol{\alpha}})} - \bar{c}(1-\frac{a}{\bar{c}}\operatorname{tr}(\bar{\mathbf{T}}-\bar{\boldsymbol{\alpha}})) \\
&= \sqrt{\bar{J}_2} - \bar{c}(1-\frac{a}{\bar{c}}\bar{I}_1) = 0
\end{aligned}
\tag{2.45}
$$

characterizes the onset of the plastic flow caused by the plastic behavior, where $\bar{c}$ is the current equivalent stress, $a/\bar{c}$ represents the hydrostatic stress coefficient related to the SD effect, and $\bar{\boldsymbol{\alpha}}$ describes the effective back stress tensor associated with the Bauschinger effect.

In addition, Spitzig and Richmond (1984) experimentally observed that the plastic volume change in iron-based materials and aluminum alloys is only marginally affected by the hydrostatic-stress. Hence, a non-associated flow rule is used to predict the evolution of plastic strain, ensuring compliance with the assumption of incompressibility in plastic deformations. The non-associated von Mises potential function (g^{pl}) is given by

$$
g^{\mathrm{pl}}(\bar{\mathbf{T}}-\bar{\boldsymbol{\alpha}}) = \sqrt{\frac{1}{2}\operatorname{dev}(\bar{\mathbf{T}}-\bar{\boldsymbol{\alpha}})\cdot\operatorname{dev}(\bar{\mathbf{T}}-\bar{\boldsymbol{\alpha}})} = \sqrt{\bar{J}_2}\,.
\tag{2.46}
$$

In addition, the effective plastic strain rate can be computed in the form

$$
\dot{\bar{\mathbf{H}}}^{\mathrm{pl}} = \dot{\lambda}\frac{1}{2\sqrt{\bar{J}_2}}\operatorname{dev}(\bar{\mathbf{T}}-\bar{\boldsymbol{\alpha}}) = \dot{\gamma}\bar{\mathbf{N}}\,,
\tag{2.47}
$$

where the equivalent plastic strain rate $\dot{\gamma} = \frac{\dot{\lambda}}{\sqrt{2}}$ is the non-negative plastic multiplier, and $\bar{\mathbf{N}} = \frac{\operatorname{dev}(\bar{\mathbf{T}}-\bar{\boldsymbol{\alpha}})}{\sqrt{2\bar{J}_2}}$ represents the normalized deviatoric effective reduced stress tensor, describing the direction of the plastic strain rate.

The extended double Voce-hardening law (Holmen et al., 2017; Wei et al., 2023b, 2022)

$$
\bar{c} = c_0 + Q_1(1-e^{-p_1\gamma}) + Q_2\xi(1-e^{-p_2\gamma})
\tag{2.48}
$$

is used to model the change of the size of the yield surface, where c_0

denotes the initial yield stress, Q_1 and Q_2 represent isotropic hardening moduli, and p_1 and p_2 are material constants that describe the shape of the hardening function. Furthermore, ξ is an elastic strain triaxiality based variable function proposed to characterize material behaviors more accurately at the onset of plasticity under a wide range of elastic strain triaxialities. The parameter ξ is given by

$$\xi = \begin{cases} -6.650\eta_{\text{el}} - 0.565 & \text{for } \eta_{\text{el}} < -0.1 \\ \frac{1}{0.787(1+e^{-50(\eta_{\text{el}}+1)})} & \text{for } -0.1 \leq \eta_{\text{el}} < 0.1 \text{ and } \eta_{\text{el}} \geq 0.45 \\ 2.477\eta_{\text{el}} + 1.025 & \text{for } 0.1 \leq \eta_{\text{el}} < 0.45 \end{cases},$$

$$(2.49)$$

where the coefficients are inversely calibrated by one-axial and biaxial experiments, covering a wide range of the elastic strain triaxialities, see Wei et al. (2023b, 2022) for more details.

The modified Chaboche type non-linear kinematic hardening law (Chaboche and Rousselier, 1983; Voyiadjis et al., 2013; Wei et al., 2022) captures the transformation of the current yield surface through the effective back stress tensor $\bar{\boldsymbol{\alpha}}$. To provide a more accurate description of the Bauschinger effect under finite strain, the effective back stress rate tensor $\dot{\bar{\boldsymbol{\alpha}}}$ is additively decomposed into three terms, as follows:

$$\dot{\bar{\boldsymbol{\alpha}}} = \dot{\bar{\boldsymbol{\alpha}}}_1 + \dot{\bar{\boldsymbol{\alpha}}}_2 + \dot{\bar{\boldsymbol{\alpha}}}_3,$$

$$(2.50)$$

with

$$\begin{aligned} \dot{\bar{\boldsymbol{\alpha}}}_1 &= b_1\chi\dot{\bar{\mathbf{H}}}^{\text{pl}} - b_2\chi\dot{\gamma}\bar{\boldsymbol{\alpha}}_1, \\ \dot{\bar{\boldsymbol{\alpha}}}_2 &= b_3\dot{\bar{\mathbf{H}}}^{\text{pl}} - b_4\dot{\gamma}\bar{\boldsymbol{\alpha}}_2, \\ \dot{\bar{\boldsymbol{\alpha}}}_3 &= b_5\dot{\bar{\mathbf{H}}}^{\text{pl}} - (1 - \cos^2\theta)b_6\dot{\gamma}\bar{\boldsymbol{\alpha}}_3, \end{aligned}$$

$$(2.51)$$

respectively, where $b_1...b_6$ are material constants. The exponential Decay function

$$\chi = 0.8e^{-300\gamma} + 0.2$$

$$(2.52)$$

models the decreasing translation rate of the current yield surface with an increasing accumulated equivalent plastic strain γ. This approach

was proposed by Voyiadjis et al. (2013). In addition, Wei et al. (2022) introduces a scalar angle parameter

$$\cos^2 \theta = \frac{((\bar{\mathbf{T}} - \bar{\boldsymbol{\alpha}}) \cdot \bar{\boldsymbol{\alpha}}_3)^2}{\left\| \bar{\mathbf{T}} - \bar{\boldsymbol{\alpha}} \right\| \left\| \bar{\boldsymbol{\alpha}}_3 \right\|} \tag{2.53}$$

into the third terms of the effective back stress rate, activating or deactivating the non-linear recovery term under large plastic deformations. This correction implies that the transformation rate of the yield surface decreases under finite strain or when there are changes in loading paths. Furthermore, the isotropic hardening ratio ρ_h is proposed to combine the isotropic and kinematic hardening part. Therefore, the current total equivalent isotropic hardening rate is expressed as

$$\dot{\bar{\sigma}} = k_h \rho_h \dot{\bar{c}} + (1 - k_h \rho_h) \dot{\bar{\alpha}} \quad \text{with} \quad 0 \leq \rho_h \leq 1 \,, \tag{2.54}$$

where $\dot{\bar{c}}$ denotes the current equivalent stress rate associated with the isotropic hardening, and $\dot{\bar{\alpha}}$ is the current equivalent effective back stress rate corresponding to kinematic hardening. k_h is a scalar parameter to model the change in hardening ratio after reverse loading conditions. This above-mentioned phenomenon is widely observed in the experiments (Daroju et al., 2022; Ohno, 1982; Ohno and Kachi, 1986; Okorokov et al., 2019b; Wei et al., 2023b). One possible explanation could be that metal hardening during plastic deformation results from dislocation immobilization due to obstacle formation. Shear reverse loading briefly restores mobility to some dislocations, temporarily softening a specific plastic strain region before subsequent immobilization and further hardening (Ohno, 1982). Following this physical explanation, Wei et al. (2023b) introduced piecewise function as follows:

$$k_h = \begin{cases} 0 & \text{for} & \gamma^* \leq 0.05 & \text{and} & \gamma^* < \gamma \\ f_k & \text{for} & 0.05 < \gamma^* \leq 0.15 & \text{and} & \gamma^* < \gamma \\ 1 & \text{for} & 0.15 < \gamma^* < \gamma & \text{or} & \gamma^* \geq \gamma \end{cases} \tag{2.55}$$

with

$$f_k = 1 - e^{-60(\gamma^* - 0.05)} + (10\gamma^* - 0.5)e^{-6} \,,$$

where γ^* is the cyclic equivalent plastic strain, and the value of γ^* resets to zero during each elastic unloading paths. In this formulation, tem-

porary softening occurs in a range of $\gamma^* \leq 0.05$ based on a numerical study performed by (Ohno, 1982), and hardening recovers slowly during further loading processes until $\gamma^* = 0.15$. One of the highlights of the proposed approach is that only a single parameter is needed, compared to the multi-factor (Okorokov et al., 2019a,b) or multi-surface methods (Ohno, 1982; Ohno and Kachi, 1986).

2.5 Anisotropic damage with combined softening

Many previous studies indicated that damage and fracture behavior depends on stress states (Bai and Wierzbicki, 2008; Brünig, 2003a; Brünig et al., 2008; Gao et al., 2010; Yu et al., 2018). In addition, the damage might occur early after uniaxial compressive reverse load since the micro-defects change their shapes and sizes (Kanvinde and Deierlein, 2007). For a more accurate characterization of the changes in the position and shape of the current damage surface under cyclic loading conditions, Wei et al. (2023b) introduced a novel combined softening rule based on Brünig's damage strain rate tensor (Brünig, 2003a).

The damage condition taking into account the combined softening law is expressed as

$$
\begin{aligned}
f^{\mathrm{da}} &= \hat{\alpha}\,\mathrm{tr}(\mathbf{T}-\boldsymbol{\alpha}) + \hat{\beta}\sqrt{\frac{1}{2}\,\mathrm{dev}(\mathbf{T}-\boldsymbol{\alpha})\cdot\mathrm{dev}(\mathbf{T}-\boldsymbol{\alpha})} - \tilde{\sigma} \\
&= \hat{\alpha}I_1 + \hat{\beta}\sqrt{J_2} - \tilde{\sigma} = 0\,,
\end{aligned}
\tag{2.56}
$$

where $\boldsymbol{\alpha}$ represents the damage back stress tensor, and $\tilde{\sigma}$ is the current equivalent isotropic softening. The stress-state-dependent coefficients

$$
\hat{\alpha}(\eta) = \left\{
\begin{array}{llll}
0 & \text{for} & \eta & \leq & 0 \\
\frac{1}{3} & \text{for} & \eta & > & 0
\end{array}
\right.
$$

and
$$
\hat{\beta}(\eta,\omega) = -0.017\omega^3 - 0.065\omega^2 - 0.078\omega - 1.28\eta + 0.85 \geq 0
$$

$$\tag{2.57}$$

govern different damage conditions under different stress states (Brünig et al., 2013, 2016). For example, $\hat{\alpha}$ equals zero for all negative stress triaxialities, see Fig. 2.4(a), simplifying the damage condition to $\hat{\beta}\sqrt{J_2}$.
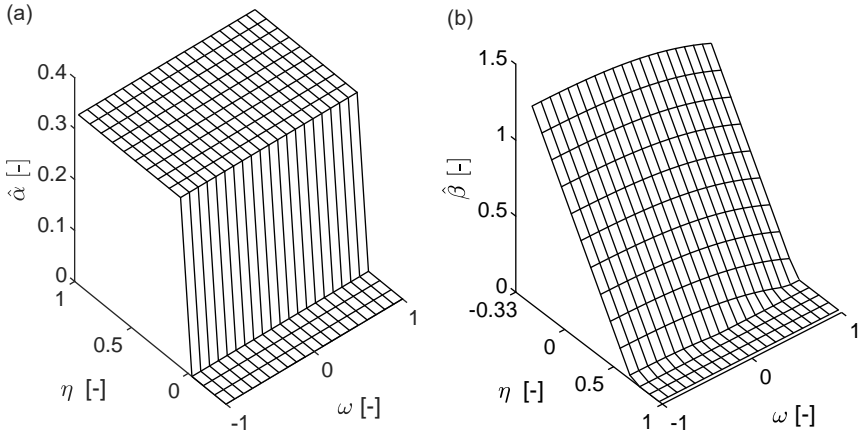
Figure 2.4: Damage parameters $\hat{\alpha}$ (a) and $\hat{\beta}$ (b) in the damage condition (2.56) (Wei et al., 2023b).

Moreover, $\hat{\beta}$ increases with increasing the negative triaxialities, as shown in Fig. 2.4(b). Notably, there is no damage for metals under large negative stress triaxialities ($\eta \leq \eta_{\mathrm{cut}}$), see Bao and Wierzbicki (2004) and Brünig et al. (2018). It is indicated that the onset of the damage is mainly due to the shear or deviatoric stresses under nearly zero and low negative stress triaxialities. On the other hand, $\hat{\beta}$ becomes zero under large stress triaxialities ($\eta \geq \frac{2}{3}$). Thus, the damage condition is governed only by the first stress invariant term $\hat{\alpha}I_1$, with $\hat{\alpha} = \frac{1}{3}$. In this context, hydrostatic stresses for high stress triaxialities significantly affect the onset of damage. Obviously, the proposed damage condition depends on the stress states. In addition, $\hat{\alpha}$ and $\hat{\beta}$ are calibrated by analyzing the initial equivalent damage stresses and the corresponding stress states (η and ω) of the unit-cell containing a spherical void in its center under various loading paths. The detail of the identification and validation of $\hat{\alpha}$ and $\hat{\beta}$ can be found in (Brünig et al., 2013, 2016).

Furthermore, the non-associated damage potential function is modified as a combination of the first transformed reduced stress invariant $\tilde{I}_1 = \mathrm{tr}(\tilde{\mathbf{T}} - \tilde{\boldsymbol{\alpha}})$ and second deviatoric transformed reduced stress invariant

$\tilde{J}_2 = \sqrt{\frac{1}{2} \operatorname{dev}(\tilde{\mathbf{T}} - \tilde{\boldsymbol{\alpha}}) \cdot \operatorname{dev}(\tilde{\mathbf{T}} - \tilde{\boldsymbol{\alpha}})}$, which is given by

$$g^{\mathrm{da}}(\tilde{\mathbf{T}} - \tilde{\boldsymbol{\alpha}}) = g^{\mathrm{da}}(\tilde{I}_1, \tilde{J}_2) = \tilde{\alpha}\tilde{I}_1 + \tilde{\beta}\sqrt{\tilde{J}_2}\,. \tag{2.58}$$

Based on the kinematic model proposed by Brünig (2003a), the transformed stress and damage back stress tensor can be computed as

$$\tilde{\mathbf{T}} = \mathbf{Q}^{\mathrm{el}}\mathbf{T}\mathbf{Q}^{\mathrm{el}-1} \quad \text{and} \quad \tilde{\boldsymbol{\alpha}} = \mathbf{Q}^{\mathrm{el}}\boldsymbol{\alpha}\mathbf{Q}^{\mathrm{el}-1}\,, \tag{2.59}$$

respectively. In addition, the damage strain rate tensor can be calculated as the derivative of the damage potential function to the transformed reduced tensor $(\tilde{\mathbf{T}} - \tilde{\boldsymbol{\alpha}})$, which leads to

$$\dot{\mathbf{H}}^{\mathrm{da}} = \dot{\mu}\frac{\partial g^{\mathrm{da}}(\tilde{\mathbf{T}} - \tilde{\boldsymbol{\alpha}})}{\partial(\tilde{\mathbf{T}} - \tilde{\boldsymbol{\alpha}})} = \dot{\mu}(\tilde{\alpha}\frac{1}{\sqrt{3}}\mathbf{1} + \tilde{\beta}\tilde{\mathbf{N}})\,, \tag{2.60}$$

where $\dot{\mu}$ represents the non-negative damage multiplier. Clearly, $\dot{\mathbf{H}}^{\mathrm{da}}$ consists of two terms: (1) the isotropic part $\tilde{\alpha}\frac{1}{\sqrt{3}}\mathbf{1}$ associated with the growth of micro-defects; (2) the deviatoric part based on the transformed normalized reduced deviatoric stress tensor $\tilde{\mathbf{N}} = \frac{\operatorname{dev}(\tilde{\mathbf{T}} - \tilde{\boldsymbol{\alpha}})}{\sqrt{2J_2}}$ describes the isochoric deformation of the micro-defects. The damage parameters $\tilde{\alpha}$ and $\tilde{\beta}$ are calibrated by performing numerical simulations using unit-cell containing a spherical void in its center across a wide range of stress states. These numerical simulations are used to identify parameters in the damage strain rate tensor, see Eq. (2.60), based on the kinematic relation of the continuum damage model proposed by Brünig et al. (2013). These kinematic stress-dependent parameters (Brünig et al., 2013, 2016) are defined as

$$\tilde{\alpha}(\eta) = \left\{ \begin{array}{llll} 0 & \text{for} & \eta & \leq & 0 \\ 0.5714\eta \leq 1 & \text{for} & \eta & > & 0 \end{array} \right.\,, \tag{2.61}$$

and

$$\tilde{\beta}(\eta,\omega) = \tilde{\beta}_0(\eta) + \left\{ \begin{array}{llll} (1-\omega^2)(0.0378\eta - 0.0252) & \text{for} & \eta & \leq & 2/3 \\ 0 & \text{for} & \eta & > & 2/3 \end{array} \right. \tag{2.62}$$

with

$$\tilde{\beta}_0(\eta) = \begin{cases} 0.87 & \text{for} & \eta \leq 1/3 \\ 0.97875 - 0.32625\eta \geq 0 & \text{for} & \eta > 1/3 \end{cases}, \quad (2.63)$$
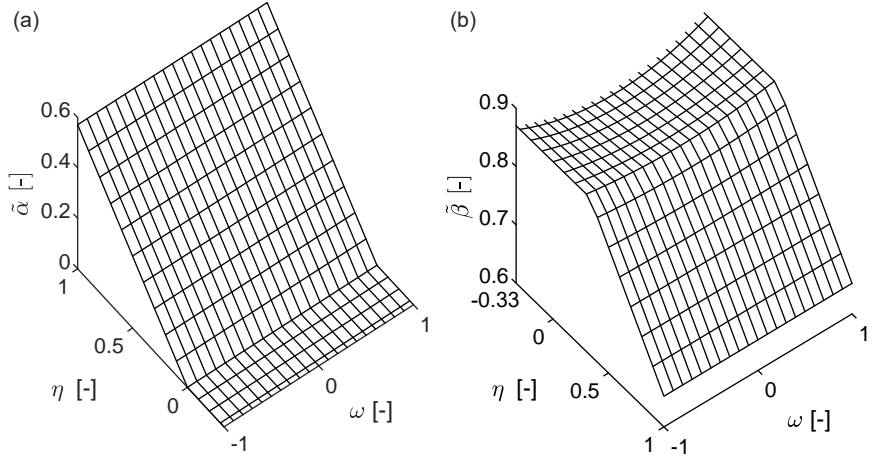

Figure 2.5: Damage parameters $\tilde{\alpha}$ (a) and $\tilde{\beta}$ (b) in the damage evolution equation (2.60) (Wei et al., 2023b).

respectively. In addition, $\tilde{\alpha}$ and $\tilde{\beta}$ are visualized in Fig. 2.5. For low negative stress triaxialities ($-\frac{1}{3} < \eta \leq 0$), $\tilde{\alpha}$ is zero, and the damage strain rate tensor is only governed by the deviatoric part. This corresponds to the damage mechanism involving the formation and growth of micro-shear-cracks caused by deviatoric stresses under shear or compressive loading conditions. For high stress triaxialities, $\tilde{\alpha}$ increases with increasing stress triaxialities, whereas $\tilde{\beta}$ decreases as stress triaxialities increase, as shown in Fig. 2.5. Thus, damage is mainly caused by the formation, growth, coalescence of the micro-voids under tension-dominated stress states. In addition, damage is due to both above-mentioned mechanisms for the low positive stress triaxialities. Briefly, the effect of different damage mechanisms on macroscopic deformation behavior can be accurately characterized by the proposed damage criterion and damage evolution equation with damage parameters identified by the micro-mechanical

simulations.

Furthermore, an Armstrong-Frederick type non-linear anisotropic softening law based on the damage strain rate tensor $\dot{\mathbf{H}}^{\mathrm{da}}$ (2.60) is newly proposed to predict the transformation of the damage surface (2.56) under different stress states (Wei et al., 2023b). Thus, the rate of the back stress tensor is given by

$$\dot{\boldsymbol{\alpha}} = d_1\dot{\mathbf{H}}^{\mathrm{da}} - d_2\dot{\mu}\boldsymbol{\alpha}\,, \tag{2.64}$$

where d_1 and d_2 are softening material constants. It is clear that the evolution of the damage back stress tensor depends on stress-states since the $\dot{\mathbf{H}}^{\mathrm{da}}$ contains the stress-state-dependent variables $\tilde{\alpha}$ and $\tilde{\beta}$. Therefore, the newly proposed softening law enables the characterization of the change in the position of the damage surface under different loading paths and introduces anisotropic properties in the softening law. It is worth noting that the proposed softening law can also be decomposed into different terms to better predict the damage behavior.

The exponential softening law

$$\tilde{\sigma} = \tilde{\sigma}_0 - C_1 e^{-C_2\mu} \tag{2.65}$$

is additionally introduced to model the change in the shape of the current damage surface, where $\tilde{\sigma}_0$ is the initial damage stress, C_1 denotes the damage softening modulus, and C_2 describes isotropic softening material constant.

As mentioned in Section 2.4, the isotropic hardening ratio ρ_h combines the isotropic and kinematic hardening. Following this idea, the scalar softening ratio ρ_s is further proposed to describe the mixed softening behavior. Hence, the total equivalent softening rate can be calculated as

$$\dot{\sigma} = \rho_s\dot{\tilde{\sigma}} + (1 - \rho_s)\dot{\alpha}_{\mathrm{eq}} \quad \text{with} \quad 0 \leq \rho_s \leq 1\,, \tag{2.66}$$

where $\dot{\tilde{\sigma}}$ is the current equivalent damage stress rate and $\dot{\alpha}_{\mathrm{eq}}$ represents the equivalent damage back stress rate.

3 Numerical implementation

In the present work, the numerical simulations are performed within the commercial program package Ansys Classic APDL. Thus, the proposed two-surface elastic-plastic-damage continuum model in Chapter 2 is implemented as a user-defined subroutine. To be able to solve the discretized equilibrium equations, the numerical integration of the constitutive rate equations is required.

The main idea is to use one single step without iterations strategy, first proposed by Nemat-Nasser (1991) and Nemat-Nasser and Li (1992) for the elastic-plastic material model. In this approach, the plastic strain increment is first assumed to be the same as the total strain increment since the plastic deformations are predominant for ductile metals after plastic yielding, followed by an elastic corrector step to compute the current plastic increment. This method provides accurate numerical results for various loading conditions. Afterward, Brünig (1999b) introduced the plastic predictor-elastic corrector method in the finite element analyses for the large hydrostatic stress-sensitive elastic-plastic material. Moreover, Brünig (2003b) innovatively extended the above-mentioned approach for implementing an anisotropic elastic-plastic-damage two-surface uncoupled continuum model. Compared to one-surface elastoplasticity material, two independent unknown variables (plastic and damage increment) must be computed by solving a comprehensive set of integrated equations. Hence, the inelastic predictor-elastic corrector approach assumes in the first step the elastic strain increment to be equal to zero in the inelastic predictor step and then computes the plastic and damage strain increment error in the elastic corrector step. Finally, with the current stress direction and elastic-damage material laws, all stress and strain components can be determined.

Two different implementation strategies are considered for the proposed continuum model in undamaged and damaged configurations.

- In the fictitious undamaged configurations, the plastic predictor-elastic corrector is used to compute the stress and strain compo-

nents, as well as the current yield surface due to the plastic deformations by solving a single scalar-valued rate constitutive equation.

- In the damaged configurations, the inelastic predictor-elastic corrector approach is introduced to calculate the stress and strain components, the current yield surface, and the current damage surface caused by the inelastic deformations by solving a system of the scalar-valued rate constitutive equations.

The following will comprehensively summarize the numerical integration for the proposed material model described in Chapter 2. This approach is adapted from Wei et al. (2024b).

3.1 Preliminaries

Deriving Eqs. (2.45) and (2.56) with respect to time, respectively, the plastic consistency condition is obtained as follow:

$$\dot{f}^{\mathrm{pl}} = \left(\frac{1}{2\sqrt{\bar{J}_2}} \operatorname{dev}(\bar{\mathbf{T}} - \bar{\boldsymbol{\alpha}}) + a\mathbf{1} \right) \cdot (\dot{\bar{\mathbf{T}}} - \dot{\bar{\boldsymbol{\alpha}}}) - \left(1 - \frac{a}{\bar{c}}\bar{I}_1 \right) \dot{\bar{c}} = 0, \quad (3.1)$$

and the damage consistency condition is given by

$$\dot{f}^{\mathrm{da}} = \left(\hat{\alpha}\mathbf{1} + \hat{\beta}\frac{1}{2\sqrt{J_2}} \operatorname{dev}(\mathbf{T} - \boldsymbol{\alpha}) \right) \cdot (\dot{\mathbf{T}} - \dot{\boldsymbol{\alpha}}) - \dot{\hat{\sigma}} = 0. \quad (3.2)$$

Making use of the normalized deviatoric effective reduced stress tensor

$$\bar{\mathbf{N}} = \frac{\operatorname{dev}(\bar{\mathbf{T}} - \bar{\boldsymbol{\alpha}})}{2\sqrt{\bar{J}_2}} \quad (3.3)$$

and the normalized deviatoric reduced stress tensor

$$\mathbf{N} = \frac{\operatorname{dev}(\mathbf{T} - \boldsymbol{\alpha})}{2\sqrt{J_2}}, \quad (3.4)$$

Eqs. (3.1) and (3.2) can be rewritten as

$$\left(1 - \frac{a}{\bar{c}}\bar{I}_1\right)\dot{\bar{c}} = \left(\frac{1}{\sqrt{2}}\bar{\mathbf{N}} + a\mathbf{1}\right) \cdot (\dot{\bar{\mathbf{T}}} - \dot{\bar{\boldsymbol{\alpha}}}) \tag{3.5a}$$

$$\dot{\bar{\sigma}} = \left(\hat{\alpha}\mathbf{1} + \hat{\beta}\frac{1}{\sqrt{2}}\mathbf{N}\right) \cdot (\dot{\mathbf{T}} - \dot{\boldsymbol{\alpha}}). \tag{3.5b}$$

3.1.1 Fictitious undamaged configurations

As mentioned in Section 2.1, the fictitious undamaged configurations exclusively describe elastic-plastic deformations. Consequently, the plastic consistency condition, denoted as $\dot{f}^{\mathrm{pl}}$ in Eq. (3.5a), is the only relevant criterion. Additionally, the total effective strain rate can be decomposed into effective elastic ($\dot{\bar{\mathbf{H}}}^{\mathrm{el}}$) and plastic ($\dot{\bar{\mathbf{H}}}^{\mathrm{pl}}$) part, see Eq. (2.12), and the corresponding effective stress rate

$$\dot{\bar{\mathbf{T}}} = 2G\dot{\bar{\mathbf{H}}}^{\mathrm{el}} + \left(K - \frac{2}{3}G\right)\mathrm{tr}\,\dot{\bar{\mathbf{H}}}^{\mathrm{el}}\mathbf{1} \tag{3.6}$$

can be derived from the elastic law (2.38) with respect to time in the undamaged configurations.

Inserting Eqs. (2.12) and (3.6), and the effective back stress rate tensor $\dot{\bar{\boldsymbol{\alpha}}}$ (2.51) into Eq. (3.5a), which leads to

$$\left(1 - \frac{a}{\bar{c}}\bar{I}_1\right)\dot{\bar{c}} = \sqrt{2}G\bar{\mathbf{N}} \cdot (\dot{\bar{\mathbf{H}}} - \dot{\bar{\mathbf{H}}}^{\mathrm{pl}}) + 3aK\,\mathrm{tr}\,\dot{\bar{\mathbf{H}}} - \frac{\sqrt{2}}{2}\bar{b}_1(\bar{\mathbf{N}} \cdot \dot{\bar{\mathbf{H}}}^{\mathrm{pl}})$$
$$+ \sqrt{2}\left(\frac{1}{2}\bar{b}_2(\bar{\mathbf{N}} \cdot \bar{\boldsymbol{\alpha}}) + \frac{a}{\sqrt{2}}\bar{b}_2\,\mathrm{tr}\,\bar{\boldsymbol{\alpha}}\right)\dot{\gamma} \tag{3.7}$$

with

$$\bar{b}_1 = (1 - \rho_h)(b_1 + b_3 + b_5), \tag{3.8}$$

and

$$\bar{b}_2 = (1 - \rho_h)(b_2 + b_4 + b_6(1 - \cos^2\theta)). \tag{3.9}$$

Substituting $\dot{\bar{\gamma}} = \bar{\mathbf{N}} \cdot \dot{\bar{\mathbf{H}}}^{\mathrm{pl}}$ (2.47) into Eq. (3.7), one arrives at

$$\left(1 - \frac{a}{\bar{c}}\bar{I}_1\right)\dot{\bar{c}} = \sqrt{2}G(\dot{\bar{\varepsilon}} - (1 + w_h)\dot{\bar{\gamma}}) \tag{3.10}$$

with

$$\dot{\bar{\varepsilon}} = \bar{\mathbf{N}} \cdot \dot{\bar{\mathbf{H}}} + \frac{3aK}{\sqrt{2}G}\,\mathrm{tr}\,\dot{\bar{\mathbf{H}}}, \tag{3.11}$$

and

$$w_h = \frac{1}{2G}\bar{b}_1 - \frac{1}{2G}\bar{b}_2(\bar{\mathbf{N}} \cdot \bar{\boldsymbol{\alpha}}) - \frac{a}{\sqrt{2}G}\bar{b}_2\,\mathrm{tr}\,\bar{\boldsymbol{\alpha}}. \tag{3.12}$$

Furthermore, numerically integrating Eq. (3.10) over the time increment Δt results in

$$\Delta\bar{c} = \bar{c}(t + \Delta t) - \bar{c}(t) = \sqrt{2}\bar{G}(\Delta\bar{\varepsilon} - (1 + w_h)\Delta\bar{\gamma}) \tag{3.13}$$

with $\bar{G} = \frac{G}{1 - \frac{a}{\bar{c}}\bar{I}_1}$.

Hence, the goal in the fictitious undamaged configurations is to determine the non-negative $\Delta\bar{\gamma}$ that satisfies the Kuhn-Tucker condition:

$$f^{\mathrm{pl}} \leq 0, \qquad \Delta\bar{\gamma} \geq 0, \qquad \Delta\bar{\gamma}f^{\mathrm{pl}} = 0. \tag{3.14}$$

3.1.2 Damaged configurations

In the damaged configurations, inelastic deformations are mainly caused by plasticity and damage. Therefore, both the plastic and damage consistency conditions must be satisfied simultaneously. Moreover, the elastic strain rate tensor $\dot{\mathbf{H}}^{\mathrm{el}}$ is calculated based on Eq. (2.18), and the associated Kirchhoff stress rate is given by

$$\begin{aligned}
\dot{\mathbf{T}} =\; & 2(G + \eta_2\,\mathrm{tr}\,\mathbf{A}^{\mathrm{da}})\dot{\mathbf{H}}^{\mathrm{el}} + (K - \frac{2}{3}G + 2\eta_1\,\mathrm{tr}\,\mathbf{A}^{\mathrm{da}})\,\mathrm{tr}\,\dot{\mathbf{H}}^{\mathrm{el}}\mathbf{1} \\
& + \eta_3(\mathbf{A}^{\mathrm{da}} \cdot \dot{\mathbf{H}}^{\mathrm{el}})\mathbf{1} + \eta_3\,\mathrm{tr}\,\dot{\mathbf{H}}^{\mathrm{el}}\mathbf{A}^{\mathrm{da}} + \eta_4(\dot{\mathbf{H}}^{\mathrm{el}}\mathbf{A}^{\mathrm{da}} + \mathbf{A}^{\mathrm{da}}\dot{\mathbf{H}}^{\mathrm{el}}) \\
& + 2\eta_2\,\mathrm{tr}\,\dot{\mathbf{H}}^{\mathrm{da}}\mathbf{A}^{\mathrm{el}} + 2\eta_1\,\mathrm{tr}\,\dot{\mathbf{H}}^{\mathrm{da}}\,\mathrm{tr}\,\mathbf{A}^{\mathrm{el}}\mathbf{1} + \eta_3\,\mathrm{tr}\,\mathbf{A}^{\mathrm{el}}\dot{\mathbf{H}}^{\mathrm{da}} \\
& + \eta_3(\dot{\mathbf{H}}^{\mathrm{da}} \cdot \mathbf{A}^{\mathrm{el}})\mathbf{1} + \eta_4(\mathbf{A}^{\mathrm{el}}\dot{\mathbf{H}}^{\mathrm{da}} + \dot{\mathbf{H}}^{\mathrm{da}}\mathbf{A}^{\mathrm{el}}).
\end{aligned} \tag{3.15}$$

Considering the plastic and damage strain rate tensors (2.47) and (2.60), the effective back stress rate tenor (2.51), the damage back stress rate tensor (2.64), and the Kirchhoff stress (2.18) and elastic strain rate tensor (3.15), the plastic (3.1) and damage consistency (3.2) conditions can be numerically integrated over the time increment Δt as follows:

$$
\begin{aligned}
\Delta\bar{c} &= \sqrt{2}\bar{G}(\Delta\varepsilon_1 - w_1\Delta\gamma - w_2\Delta\mu) \\
\Delta\tilde{\sigma} &= \sqrt{2}G_2(\Delta\varepsilon_2 - w_3\Delta\gamma - w_4\Delta\mu)
\end{aligned}
\tag{3.16}
$$

with the equivalent strain increments

$$
\begin{aligned}
\Delta\varepsilon_1 &= \frac{1}{\sqrt{2}\bar{G}}\mathbf{Z}_1 \cdot \Delta\bar{\mathbf{H}} \\
\Delta\varepsilon_2 &= \frac{1}{\sqrt{2}G_2}\mathbf{Z}_3 \cdot \Delta\mathbf{H} \,,
\end{aligned}
\tag{3.17}
$$

where

$$
\bar{G} = \frac{G}{1 - \frac{a}{\bar{c}}\bar{I}_1}
\tag{3.18}
$$

and

$$
G_2 = G + \eta_2 \operatorname{tr} \mathbf{A}^{\mathrm{da}}.
\tag{3.19}
$$

Additionally, the parameters $w_1...w_4$ are defined as

$$
\begin{aligned}
w_1 &= \mathbf{R}\bar{\mathbf{N}}\mathbf{R}^{-1} \cdot \bar{\mathbf{N}} + \frac{1}{2G}\bar{b}_1 - \frac{1}{2G}\bar{b}_2(\bar{\mathbf{N}} \cdot \bar{\boldsymbol{\alpha}}) - \frac{a}{\sqrt{2}G}\bar{b}_2 \operatorname{tr} \bar{\boldsymbol{\alpha}} \,, \\
w_2 &= \frac{1}{\sqrt{2}G}\mathbf{Q}^{\mathrm{el}}\mathbf{Z}_1\mathbf{Q}^{\mathrm{el}-1} \cdot \mathbf{Z}_2 \,, \\
w_3 &= \frac{1}{\sqrt{2}G_2}\mathbf{R}\mathbf{Z}_3\mathbf{R}^{-1} \cdot \bar{\mathbf{N}} \,, \\
w_4 &= \frac{1}{\sqrt{2}G_2}\left[(\mathbf{Q}^{\mathrm{el}}\mathbf{Z}_3\mathbf{Q}^{\mathrm{el}-1} - \mathbf{Z}_4) \cdot \mathbf{Z}_2 + w_5\right] \,, \\
w_5 &= \hat{\alpha}(1 - \rho_s)d_2 \operatorname{tr}(\boldsymbol{\alpha}) + (1 - \rho_s)d_2\frac{\hat{\beta}}{\sqrt{2}}(\mathbf{N} \cdot \boldsymbol{\alpha}) \,,
\end{aligned}
\tag{3.20}
$$

with the following tensor abbreviations

$$\mathbf{Z}_1 = \sqrt{2}G\bar{\mathbf{N}} + 3aK\mathbf{1}\,,$$

$$\mathbf{Z}_2 = \tilde{\alpha}\mathbf{1} + \tilde{\beta}\bar{\mathbf{N}}\,,$$

$$\mathbf{Z}_3 = \sqrt{2}\hat{\beta}G_2 + \left(\hat{\alpha}(3K + 6\eta_1 + 2\eta_2 + \eta_3)\operatorname{tr}\mathbf{A}^{\mathrm{da}} + \frac{\hat{\beta}}{\sqrt{2}}\eta_3\mathbf{N}\cdot\mathbf{A}^{\mathrm{da}}\right)\mathbf{1}$$

$$+ \frac{\hat{\beta}}{\sqrt{2}}\eta_4(\mathbf{N}\mathbf{A}^{\mathrm{da}} + \mathbf{A}^{\mathrm{da}}\mathbf{N}) + \hat{\alpha}(3\eta_3 + 2\eta_4)\mathbf{A}^{\mathrm{da}}\,,$$

$$\mathbf{Z}_4 = \frac{\hat{\beta}}{\sqrt{2}}\eta_3\operatorname{tr}\mathbf{A}^{\mathrm{el}} + \frac{\hat{\beta}}{\sqrt{2}}\eta_4(\mathbf{N}\mathbf{A}^{\mathrm{el}} + \mathbf{A}^{\mathrm{el}}\mathbf{N}) + \hat{\alpha}(3\eta_3 + 2\eta_4)\mathbf{A}^{\mathrm{el}}$$

$$+ \left(\frac{\hat{\beta}}{\sqrt{2}}2\eta_2\mathbf{N}\cdot\mathbf{A}^{\mathrm{el}} + \hat{\alpha}(6\eta_1 + 2\eta_2 + \eta_3)\operatorname{tr}\mathbf{A}^{\mathrm{el}} - \hat{\alpha}(1 - \rho_s)d_1\right)\mathbf{1}$$

$$- \frac{\hat{\beta}}{\sqrt{2}}(1 - \rho_s)d_1\mathbf{N}\,. \tag{3.21}$$

Hence, in the damage configurations, the aim is to find non-scalar parameters $\Delta\gamma$ and $\Delta\mu$ considering Eq. (3.16), while ensuring they adhere to the corresponding Kuhn-Tucker conditions:

$$\begin{aligned} f^{\mathrm{pl}} &\leq 0, & \Delta\gamma &\geq 0, & \Delta\gamma f^{\mathrm{pl}} &= 0 \\ f^{\mathrm{da}} &\leq 0, & \Delta\mu &\geq 0, & \Delta\mu f^{\mathrm{da}} &= 0\,. \end{aligned} \tag{3.22}$$

3.2 Elastic behavior

If the plastic yield condition $f^{\mathrm{pl}} < 0$, $\Delta\bar{\gamma}$ equals zero as per the Kuhn-Tucker conditions (3.14) in terms of the equation $\Delta\bar{\gamma}f^{\mathrm{pl}} = 0$. The result is that the elastic strain increment tensor is equal to the total strain increment tensor

$$\Delta\mathbf{H}^{\mathrm{el}} = \Delta\bar{\mathbf{H}}^{\mathrm{el}} = \Delta\mathbf{H}\,. \tag{3.23}$$

Thus, the total elastic strain tensor at time step t_{n+1} can be computed as

$$\mathbf{A}^{\mathrm{el}} = \mathbf{A}_n^{\mathrm{el}} + \Delta\mathbf{H}^{\mathrm{el}} \tag{3.24}$$

with

$$\mathbf{A}_n^{\mathrm{el}} = \frac{1}{2}\ln\mathbf{Q}_n^{\mathrm{el}},$$

and the corresponding elastic part of transformation tensor is calculated using the first Padé approximation (Brünig, 1999a)

$$\mathbf{Q}^{\mathrm{el}} = \exp(2\mathbf{A}^{\mathrm{el}}) = [\mathbf{1} - \mathbf{A}^{\mathrm{el}}]^{-1}[\mathbf{1} + \mathbf{A}^{\mathrm{el}}]. \tag{3.25}$$

Moreover, the third Padé approximation

$$\mathbf{A}_n^{\mathrm{el}} = \left(\mathbf{Q}_n^{\mathrm{el}} - \frac{4}{15}(\mathbf{Q}_n^{\mathrm{el}})^3\right)\left(\mathbf{1} - \frac{3}{5}(\mathbf{Q}_n^{\mathrm{el}})^2\right)^{-1} \tag{3.26}$$

is used to compute the value of logarithm with high accuracy (Brünig, 1999a). Please note that, for enhanced readability, this thesis omits the subscripts $(\cdot)_{n+1}$ at current time t_{n+1}, and instead, the subscripts $(\cdot)_n$ correspond to the previous time steps at t_n.

With the current elastic strain tensor $\mathbf{A}^{\mathrm{el}}$ in hand, the current stress can be calculated in two different ways.

- In the absence of previous damage ($\mu_n = 0$), the current stress is computed using the elastic law given by Eq. (2.38).

- In the presence of previous damage ($\mu_n > 0$), the current stress is calculated using the elastic-damage law specified by Eq. (2.40).

In addition, in the absence of previous damage ($\mu_n = 0$), the elastic tangent modulus $\mathbb{C}^{\mathrm{el}}$ is given by

$$\mathbb{C}^{\mathrm{el}} = \frac{\mathrm{d}\bar{\mathbf{T}}}{\mathrm{d}\mathbf{A}^{\mathrm{el}}} = 2G\mathbb{1} + (K - \frac{2}{3}G)\mathbf{1}\otimes\mathbf{1} \tag{3.27}$$

with the fourth-order isotropic tensor

$$\mathbb{1} = \frac{1}{2}(\delta_k^i \delta_j^l + \delta^{il}\delta_{jk})\mathbf{g}_i \otimes \mathbf{g}^k \otimes \mathbf{g}_l \otimes \mathbf{g}^j \,, \tag{3.28}$$

where $\mathbf{1}$ describes the second-order identity tensor. Furthermore, the elastic-damage tangent modulus $\mathbb{C}^{\mathrm{el,d}}$ expresses in the form of

$$\mathbb{C}^{\mathrm{el,d}} = \frac{\mathrm{d}\mathbf{T}}{\mathrm{d}\mathbf{A}^{\mathrm{el}}} = 2(G + \eta_2 \operatorname{tr}\mathbf{A}_n^{\mathrm{da}})\mathbb{1} + (K - \frac{2}{3}G + 2\eta_1 \operatorname{tr}\mathbf{A}_n^{\mathrm{da}})\mathbf{1} \otimes \mathbf{1}$$
$$+ \eta_3(\mathbf{A}_n^{\mathrm{da}} \otimes \mathbf{1} + \mathbf{1} \otimes \mathbf{A}_n^{\mathrm{da}}) + \eta_4 \mathbb{A}_n^{\mathrm{da}} \tag{3.29}$$

in the presence of previous damage ($\mu_n > 0$), where $\mathbf{A}_n^{\mathrm{da}}$ represents the damage strain tensor at previous time step t_n and $\mathbb{A}_n^{\mathrm{da}} = (\mathbf{A}_n^{\mathrm{da}})_l^i \delta_j^k + (\mathbf{A}_n^{\mathrm{da}})_k^j \delta_l^i$ denotes fourth-order damage tensor.

3.3 Elastic-plastic behavior

3.3.1 Predictor-corrector-algorithm

According to Eq. (3.13), in the fictitious undamaged configurations, the predictor of the equivalent plastic strain increment

$$(1 + w_h)\Delta\bar{\gamma}_{\mathrm{pr}} = \Delta\bar{\varepsilon} \,, \tag{3.30}$$

can be equated to the equivalent total strain increment $\Delta\bar{\varepsilon}$ in the plastic predictor step, where w_h defined in Eq. (3.12) denotes the kinematic hardening factor. In addition, $\Delta\bar{\varepsilon}$ can be numerically integrated in the time increment Δt in terms of Eq. (3.11)

$$\Delta\bar{\varepsilon} = \bar{\mathbf{N}} \cdot \Delta\bar{\mathbf{H}} + \frac{3aK}{\sqrt{2}G}\operatorname{tr}\Delta\bar{\mathbf{H}} \,, \tag{3.31}$$

with

$$\bar{\mathbf{N}} \cdot \Delta\bar{\mathbf{H}} = \frac{\theta}{2}\bar{\mathbf{N}}_n \cdot \Delta\bar{\mathbf{H}} + (1 - \frac{\theta}{2})\sqrt{\operatorname{dev}\Delta\bar{\mathbf{H}} \cdot \operatorname{dev}\Delta\bar{\mathbf{H}}} \,, \tag{3.32}$$

where θ is the weighting factor between 0 and 2. Furthermore, Nemat-Nasser and Li (1992) reported that variations in the parameter θ have an insignificant impact on the numerical accuracy of the isotropic elastic-plastic materials. Hence, the θ value of 0 is chosen in the present work because the elastic strain rate is significantly smaller than the plastic strain rate, providing an estimation as reliable as those from other values. Additionally, the factor a in Eq. (3.31) can be calculated as $\frac{a}{\bar{c}} \cdot \bar{c}_n$ using the material constant $a/\bar{c}$.

The isotropic hardening tangent is given by

$$\frac{\mathrm{d}\bar{c}}{\mathrm{d}\bar{\gamma}_{\mathrm{pr}}} = p_1 Q_1 e^{-p_1 \bar{\gamma}_{\mathrm{pr}}} + p_2 Q_2 \xi e^{-p_2 \bar{\gamma}_{\mathrm{pr}}} , \tag{3.33}$$

and thus, the equivalent stress increment $\Delta\bar{c}_{\mathrm{pr}}$ can be computed as

$$\Delta\bar{c}_{\mathrm{pr}} = k_h \rho_h \frac{\mathrm{d}\bar{c}}{\mathrm{d}\bar{\gamma}_{\mathrm{pr}}} \Delta\bar{\gamma}_{\mathrm{pr}} . \tag{3.34}$$

Moreover, the predicted current total equivalent stress at time t_{n+1} can be expressed as

$$\bar{c}_{\mathrm{pr}} = \bar{c}(\gamma_n + \Delta\bar{\gamma}_{\mathrm{pr}}) = \bar{c}_n + k_h \rho_h \frac{\mathrm{d}\bar{c}}{\mathrm{d}\bar{\gamma}_{\mathrm{pr}}} \Delta\bar{\gamma}_{\mathrm{pr}} , \tag{3.35}$$

where $k_h \rho_h = 0$ in the pure kinematic hardening model, resulting in $\bar{c}_{\mathrm{pr}} = \bar{c}(\gamma_n)$.

The estimated values of the equivalent plastic strain $\bar{\gamma}_{\mathrm{pr}}$ (3.30) and the yield stress $\bar{c}_{\mathrm{pr}}$ (3.35) are obviously overestimated because the elastic strain increment is not accounted for during the plastic predictor step. The respective errors are given by

$$\Delta_{\mathrm{er}}\bar{\gamma} = \Delta\bar{\gamma}_{\mathrm{pr}} - \Delta\bar{\gamma} = \frac{\Delta\bar{c}}{\sqrt{2}\bar{G}(1 + w_h)} , \tag{3.36}$$

and

$$\Delta_{\mathrm{er}}\bar{c} \approx k_h \rho_h \frac{\mathrm{d}\bar{c}}{\mathrm{d}\bar{\gamma}_{\mathrm{pr}}} \Delta_{\mathrm{er}}\bar{\gamma} = \bar{c}_{\mathrm{pr}} - \bar{c}_n - \Delta\bar{c}, \tag{3.37}$$

respectively. Making use of Eqs. (3.36) and (3.37), the error in the equivalent plastic strain increment can be rewritten as

$$\Delta_{\mathrm{er}}\bar{\gamma} = \frac{\bar{c}_{\mathrm{pr}} - \bar{c}(t)}{\sqrt{2}\bar{G}(1 + w_h) + k_h\rho_h\frac{\mathrm{d}\bar{c}}{\mathrm{d}\bar{\gamma}}} \; . \tag{3.38}$$

Hence, the current equivalent plastic strain increment can be computed as

$$\Delta\bar{\gamma} = \Delta\bar{\gamma}_{\mathrm{pr}} - \Delta_{\mathrm{er}}\bar{\gamma} = \frac{\Delta\bar{\varepsilon}}{(1 + w_h)} - \frac{\bar{c}_{\mathrm{pr}} - \bar{c}_n}{\sqrt{2}\bar{G}(1 + w_h) + k_h\rho_h\frac{\mathrm{d}\bar{c}}{\mathrm{d}\bar{\gamma}_{\mathrm{pr}}}} \; . \tag{3.39}$$

As the normalized deviatoric effective reduced stress tensor defined in Eq. (2.47), the effective stress direction alters as

$$\bar{\mathbf{N}} - \bar{\mathbf{N}}_n = \frac{\mathrm{dev}(\bar{\mathbf{T}} - \bar{\boldsymbol{\alpha}})}{\sqrt{2\bar{J}_2}} - \frac{\mathrm{dev}(\bar{\mathbf{T}}_n - \bar{\boldsymbol{\alpha}}_n)}{\sqrt{2\bar{J}_{2,n}}} \; . \tag{3.40}$$

Rewriting Eq. (3.40), one arrives at

$$\begin{aligned}
\sqrt{2\bar{J}_2}\bar{\mathbf{N}} - \sqrt{2\bar{J}_{2,n}}\bar{\mathbf{N}}_n &= \mathrm{dev}\,\Delta\bar{\mathbf{T}} - \mathrm{dev}\,\Delta\bar{\boldsymbol{\alpha}} \\
&= 2G\,\mathrm{dev}\,\Delta\bar{\mathbf{H}}^{\mathrm{el}} - \mathrm{dev}\,\Delta\bar{\boldsymbol{\alpha}} \\
&= 2G\,\mathrm{dev}\,\Delta\bar{\mathbf{H}} - 2G\,\mathrm{dev}\,\Delta\bar{\mathbf{H}}^{\mathrm{pl}} - \mathrm{dev}\,\Delta\bar{\boldsymbol{\alpha}} \; .
\end{aligned} \tag{3.41}$$

The estimated plastic strain increment is given by

$$\Delta\bar{\mathbf{H}}^{\mathrm{pl}} = \mathrm{dev}\,\Delta\bar{\mathbf{H}}^{\mathrm{pl}} = \Delta\bar{\gamma}\bar{\mathbf{N}}_m \; , \tag{3.42}$$

where $\bar{\mathbf{N}}_m$ is the mean normalized deviatoric effective reduced stress tensor at time $t + \Delta t$. It can be computed as follows

$$\bar{\mathbf{N}}_m = \lambda_1\left[(1 - \lambda_2)\bar{\mathbf{N}} + \lambda_2\bar{\mathbf{N}}_n\right] \quad \text{with} \quad \lambda_1 = 1 \text{ and } \lambda_2 = \frac{1}{2} \; , \tag{3.43}$$

where λ_1 is employed to maintain the normalization of $\bar{\mathbf{N}}_m$, as discussed in Wang and Atluri (1994) and Wei et al. (2024b). Similarly, the esti-

mated effective back stress increment can be calculated as

$$\text{dev } \Delta\bar{\boldsymbol{\alpha}} = (1 - k_h \rho_h) \Delta\bar{\gamma} (\bar{b}_1 \bar{\mathbf{N}}_m - \sum_i b_i \text{ dev } \bar{\boldsymbol{\alpha}}_{i,n}) \quad (i = 2,4,6) \,, \quad (3.44)$$

where $\bar{b}_1 = b_1 + b_3 + b_5$ represents the sum of the kinematic hardening moduli, as shown in Eq. (2.51).

Substituting Eqs. (3.42), (3.43) and (3.44) into Eq. (3.40), the current normalized deviatoric effective reduced stress tensor can be expressed as

$$\bar{\mathbf{N}} = \frac{2G \text{ dev } \Delta\bar{\mathbf{H}} + (\sqrt{2\bar{J}_{2,n}} - G_d \Delta\bar{\gamma})\bar{\mathbf{N}}_n - \sum_i \Delta\bar{\gamma} b_i \text{ dev } \bar{\boldsymbol{\alpha}}_{i,n}}{\sqrt{2\bar{J}_2} + G_d \Delta\bar{\gamma}} \,, \quad (3.45)$$

where $G_d = G + \frac{1}{2}(1 - k_h \rho_h)\bar{b}_1$ and $i = 2,4,6$.

Following Eq. (3.43), the current normalized mean effective stress tensor is

$$\bar{\mathbf{N}}_m = \frac{1}{2}(\bar{\mathbf{N}} + \bar{\mathbf{N}}_n) \,. \tag{3.46}$$

With $\bar{\mathbf{N}}_m$ in hand, the updated plastic strain increment is given by

$$\Delta\bar{\mathbf{H}}^{\text{pl}} = \Delta\bar{\gamma} \bar{\mathbf{N}}_m \,. \tag{3.47}$$

In addition, the current elastic strain increment tensor is

$$\Delta\mathbf{H}^{\text{el}} = \Delta\bar{\mathbf{H}}^{\text{el}} = \Delta\bar{\mathbf{H}} - \Delta\bar{\mathbf{H}}^{\text{pl}} \,, \tag{3.48}$$

and the calculation of total elastic strain tensor $\mathbf{A}^{\text{el}}$ is outlined in (3.24).

3.3.2 Consistent elastic-plastic tangent modulus

The stress differential without previous damage ($\mu_n = 0$) can be computed in the form

$$\mathrm{d}\bar{\mathbf{T}} = \frac{\mathrm{d}\bar{\mathbf{T}}}{\mathrm{d}\mathbf{A}^{\text{el}}} \mathbf{A}^{\text{el}} = \mathbb{C}^{\text{el}} \mathrm{d}\mathbf{A}^{\text{el}} \,, \tag{3.49}$$

where

$$\mathrm{d}\mathbf{A}^{\mathrm{el}} = \mathrm{d}\bar{\mathbf{H}}^{\mathrm{el}} = \mathrm{d}\bar{\mathbf{H}} - \mathrm{d}\bar{\mathbf{H}}^{\mathrm{pl}} = \mathrm{d}\bar{\mathbf{H}} - \bar{\mathbf{N}}_m \mathrm{d}\bar{\gamma}. \tag{3.50}$$

Based on Eq. (3.39), one arrives at

$$\mathrm{d}\bar{\gamma} = \frac{\sqrt{2}G}{(1+w_h)\sqrt{2}G + (1 - \frac{a}{c}I_1)k_h\rho_h\frac{\mathrm{d}\bar{c}}{\mathrm{d}\bar{\gamma}}}\bar{\mathbf{N}}_n \cdot \mathrm{d}\bar{\mathbf{H}}. \tag{3.51}$$

Substituting Eq. (3.51) into Eq. (3.50), the elastic strain differential is

$$\mathrm{d}\bar{\mathbf{H}}^{\mathrm{el}} = \left(\mathbf{1} \otimes \mathbf{1} - \frac{\sqrt{2}G}{(1+w_h)\sqrt{2}G + (1 - \frac{a}{c}I_1)k_h\rho_h\frac{\mathrm{d}\bar{c}}{\mathrm{d}\bar{\gamma}}}\bar{\mathbf{N}}_m \otimes \bar{\mathbf{N}}_n\right)\mathrm{d}\bar{\mathbf{H}}. \tag{3.52}$$

Making use of Eqs. (3.52) and (3.49), in the absence of previous damage ($\mu_n = 0$), the mixed elastic-plastic tangent modulus $\mathbb{C}^{\mathrm{ep}}$ considering the isotropic-kinematic combined hardening can be calculated as

$$\mathbb{C}^{\mathrm{ep}} = \mathbb{C}^{\mathrm{el}} - \left(\frac{2\sqrt{2}G^2}{(1+w_h)\sqrt{2}G + (1 - \frac{a}{c}I_1)k_h\rho_h\frac{\mathrm{d}\bar{c}}{\mathrm{d}\bar{\gamma}}}\right)\bar{\mathbf{N}}_m \otimes \bar{\mathbf{N}}_n, \tag{3.53}$$

where the elastic tangent without previous damage $\mathbb{C}^{\mathrm{el}}$ is shown in (3.27), w_h corresponds to the kinematic hardening modulus (3.12), and $k_h\rho_h\frac{\mathrm{d}\bar{c}}{\mathrm{d}\bar{\gamma}}$ is related to the isotropic hardening modulus.

In the presence of previous damage ($\mu_n > 0$), Eq. (3.49) is given by

$$\mathrm{d}\mathbf{T} = \frac{\mathrm{d}\mathbf{T}}{\mathrm{d}\mathbf{A}^{\mathrm{el}}}\mathbf{A}^{\mathrm{el}} = \mathbb{C}^{\mathrm{el,d}}\mathrm{d}\mathbf{A}^{\mathrm{el}}, \tag{3.54}$$

Again, substituting Eq. (3.52) into Eq. (3.54), the mixed elastic-plastic tangent modulus with previous damage $\mathbb{C}^{\mathrm{ep,d}}$ for the isotropic-kinematic combined hardening is

$$\mathbb{C}^{\mathrm{ep,d}} = \mathbb{C}^{\mathrm{el,d}} - \left(\frac{2\sqrt{2}G^2}{(1+w_h)\sqrt{2}G + (1 - \frac{a}{c}I_1)k_h\rho_h\frac{\mathrm{d}\bar{c}}{\mathrm{d}\bar{\gamma}}}\right)\bar{\mathbf{N}}_m \otimes \bar{\mathbf{N}}_n, \tag{3.55}$$

where $\mathbb{C}^{\mathrm{el,d}}$ (3.29) denotes the elastic-damage tangent modulus.

3.4 Elastic-plastic-damage behavior

3.4.1 Predictor-corrector-algorithm

The plastic-damage (inelastic) predictor approach is used in the damage configurations, where the elastic strain increment is assumed as $\Delta\mathbf{H}^{\mathrm{el}} = 0$. This results in an equivalent effective stress increment $\Delta\bar{c} = 0$, indicating no plastic hardening increment, and an equivalent stress increment $\Delta\sigma = 0$, representing no evolution of damage softening. Therefore, the predicted values can be computed in the form

$$\begin{bmatrix} \Delta\gamma_{\mathrm{pr}} \\ \Delta\mu_{\mathrm{pr}} \end{bmatrix} = \begin{bmatrix} w_1 & w_2 \\ w_3 & w_4 \end{bmatrix}^{-1} \begin{bmatrix} \Delta\varepsilon_1 \\ \Delta\varepsilon_2 \end{bmatrix} \tag{3.56}$$

based on Eq. (3.16). Parameters $w_1...w_4$ are defined in Eq. (3.20), where the effective stress direction $\bar{\mathbf{N}}$ is given by

$$\bar{\mathbf{N}} = \frac{\theta}{2}\bar{\mathbf{N}}_n + (1 - \frac{\theta}{2})\mathbf{N}^F \quad \text{with} \quad 0 \leq \theta \leq 2\,, \tag{3.57}$$

and stress direction $\mathbf{N}$ can be calculated as

$$\mathbf{N} = \frac{\theta}{2}\mathbf{N}_n + (1 - \frac{\theta}{2})\mathbf{N}^F \quad \text{with} \quad 0 \leq \theta \leq 2\,, \tag{3.58}$$

where $\mathbf{N}^F$ represents the final orientation (Nemat-Nasser and Li, 1992), and it is coaxial with the deviatoric strain increment tenor

$$\mathbf{N}^F = \frac{\operatorname{dev}\Delta\mathbf{H}}{\sqrt{\operatorname{dev}\Delta\mathbf{H} \cdot \operatorname{dev}\Delta\mathbf{H}}}\,. \tag{3.59}$$

Moreover, the parameters $\hat{\alpha}_n$, $\hat{\beta}_n$, $\tilde{\alpha}_n$, $\tilde{\beta}_n$ at previous time step (t_n) are utilized to compute $w_1...w_4$ because these parameters are implicitly dependent on the stress states (Wei et al., 2024b).

Omitting the elastic strain increment $\Delta\mathbf{H}^{\mathrm{el}}$ leads to overestimations in both the plastic and damage strain increments and the equivalent yield and damage stresses. To quantify the degree of overestimation, account-

ing for the errors associated with the equivalent yield stress $\Delta_{\mathrm{er}}\bar{c}$ and the equivalent damage stress $\Delta_{\mathrm{er}}\tilde{\sigma}$ is crucial. They are given by

$$\Delta_{\mathrm{er}}\bar{c} \approx k_h\rho_h \frac{\mathrm{d}\bar{c}}{\mathrm{d}\gamma_{\mathrm{pr}}}\Delta_{\mathrm{er}}\gamma = \bar{c}_{\mathrm{pr}} - \bar{c}_n - \Delta\bar{c}, \tag{3.60}$$

and

$$\Delta_{\mathrm{er}}\tilde{\sigma} \approx \rho_s \frac{\mathrm{d}\tilde{\sigma}}{\mathrm{d}\mu_{\mathrm{pr}}}\Delta_{\mathrm{er}}\mu = \tilde{\sigma}_{\mathrm{pr}} - \tilde{\sigma}_n - \Delta\tilde{\sigma}, \tag{3.61}$$

respectively, where $k_h\rho_h$ denotes the isotropic hardening ratio and ρ_s is the softening ratio.

Making use of Eqs. (3.16), (3.60), and (3.61), the errors of the equivalent plastic and damage strain increments are calculated as follow

$$\begin{bmatrix} \Delta_{\mathrm{er}}\gamma \\ \Delta_{\mathrm{er}}\mu \end{bmatrix} = \begin{bmatrix} \sqrt{2}\bar{G}w_1 + k_h\rho_h\frac{\mathrm{d}\bar{c}}{\mathrm{d}\gamma_{\mathrm{pr}}} & \sqrt{2}\bar{G}w_2 \\ \sqrt{2}G_2w_3 & \sqrt{2}G_2w_4 + \rho_s\frac{\mathrm{d}\tilde{\sigma}}{\mathrm{d}\mu_{\mathrm{pr}}} \end{bmatrix}^{-1} \begin{bmatrix} \bar{c}_{\mathrm{pr}} - \bar{c}_n \\ \tilde{\sigma}_{\mathrm{pr}} - \tilde{\sigma}_n \end{bmatrix}. \tag{3.62}$$

By subtracting Eq. (3.62) from Eq. (3.56), one gets

$$\begin{bmatrix} \Delta\gamma \\ \Delta\mu \end{bmatrix} = \begin{bmatrix} \Delta\gamma_{\mathrm{pr}} \\ \Delta\mu_{\mathrm{pr}} \end{bmatrix} - \begin{bmatrix} \Delta_{\mathrm{er}}\gamma \\ \Delta_{\mathrm{er}}\mu \end{bmatrix} = \begin{bmatrix} w_1 & w_2 \\ w_3 & w_4 \end{bmatrix}^{-1} \begin{bmatrix} \Delta\varepsilon_1 \\ \Delta\varepsilon_2 \end{bmatrix}$$
$$- \begin{bmatrix} \sqrt{2}\bar{G}w_1 + k_h\rho_h\frac{\mathrm{d}\bar{c}}{\mathrm{d}\gamma_{\mathrm{pr}}} & \sqrt{2}\bar{G}w_2 \\ \sqrt{2}G_2w_3 & \sqrt{2}G_2w_4 + \rho_s\frac{\mathrm{d}\tilde{\sigma}}{\mathrm{d}\mu_{\mathrm{pr}}} \end{bmatrix}^{-1} \begin{bmatrix} \bar{c}_{\mathrm{pr}} - \bar{c}_n \\ \tilde{\sigma}_{\mathrm{pr}} - \tilde{\sigma}_n \end{bmatrix}. \tag{3.63}$$

As discussed in Eq. (3.41), the alteration in the effective stress direction is expressed as

$$\sqrt{\bar{J}_2}\bar{\mathbf{N}} - \sqrt{\bar{J}_{2,n}}\bar{\mathbf{N}}_n = 2G\,\mathrm{dev}\,\Delta\mathbf{H}^{\mathrm{el}} - \mathrm{dev}\,\Delta\bar{\boldsymbol{\alpha}}. \tag{3.64}$$

Wei et al. (2024b) indicted that the tensorial quantities of the $\mathbf{Q}^{\mathrm{el}}$ and $\mathbf{R}$ undergo only minimal changes during the numerical simulations. More-

over, it has been noted that the elastic metric transformation tensor $\mathbf{Q}^{\mathrm{el}}$ tends to closely approximate the identity tensor $\mathbf{1}$. Hence, in the damaged configurations, the elastic strain increment tensor (2.18) can be simplified as

$$\Delta \mathbf{H}^{\mathrm{el}} = \Delta \mathbf{H} - \Delta \bar{\mathbf{H}}^{\mathrm{pl}} - \Delta \mathbf{H}^{\mathrm{da}} \tag{3.65}$$

to determine the current stress direction. Thus, inserting Eq. (3.65) into Eq. (3.64), one arrives at

$$\sqrt{2\bar{J}_2}\bar{\mathbf{N}} - \sqrt{2\bar{J}_{2,n}}\bar{\mathbf{N}}_n = 2G \operatorname{dev} \Delta \mathbf{H} - 2G \operatorname{dev} \Delta \bar{\mathbf{H}}^{\mathrm{pl}} \\ - 2G \operatorname{dev} \Delta \mathbf{H}^{\mathrm{da}} - \operatorname{dev} \Delta \bar{\boldsymbol{\alpha}} . \tag{3.66}$$

Moreover, the deviatoric plastic increment is given by

$$\operatorname{dev} \Delta \bar{\mathbf{H}}^{\mathrm{pl}} = \Delta \gamma \bar{\mathbf{N}}_m = \frac{1}{2} \Delta \gamma (\bar{\mathbf{N}} + \bar{\mathbf{N}}_n) , \tag{3.67}$$

as shown in Eqs. (3.42) and (3.43). Similarly, the deviatoric damage strain increment can be approximately calculated as

$$\operatorname{dev} \Delta \mathbf{H}^{\mathrm{da}} = \Delta \mu \tilde{\beta} \tilde{\mathbf{N}}_m = \frac{1}{2} \Delta \mu \tilde{\beta} (\tilde{\mathbf{N}} + \tilde{\mathbf{N}}_n) , \tag{3.68}$$

in terms of the damage strain rate tensor Eq. (2.60). Then, substituting Eqs. (3.44), (3.67), and (3.68) into Eq. (3.66), and neglecting $\sqrt{2\bar{J}_2}\bar{\mathbf{N}} - \sqrt{2\bar{J}_{2,n}}\bar{\mathbf{N}}_n$ leads to

$$\frac{1}{2} \tilde{\beta} G \Delta \mu \tilde{\mathbf{N}} = 2G \operatorname{dev} \Delta \mathbf{H} - 2G \Delta \gamma \bar{\mathbf{N}}_m - \frac{1}{2} \tilde{\beta} G \Delta \mu \tilde{\mathbf{N}}_n \\ - (1 - k_h \rho_h) \Delta \gamma (\bar{b}_1 \bar{\mathbf{N}}_m - \sum_i b_i \operatorname{dev} \bar{\boldsymbol{\alpha}}_{i,n}) \quad (i = 2,4,6) . \tag{3.69}$$

This simplification is justified as the term $\sqrt{2\bar{J}_2}\bar{\mathbf{N}} - \sqrt{2\bar{J}_{2,n}}\bar{\mathbf{N}}_n$ can be considered negligible compared to the other terms in Eq. (3.69). Furthermore, the numerical analysis has shown that the most effective convergence is achieved when utilizing a constant effective deviatoric stress

direction over the time increment, i.e., $\bar{\mathbf{N}}_m = \bar{\mathbf{N}}_{n+1} = \bar{\mathbf{N}}_n$. As explained in Wei et al. (2024b), significant plastic deformations typically occur at the initiation of damage, leading to a negligible change in the effective stress direction. Based on the above assumptions, the current transformed stress direction can be computed in the form

$$
\begin{aligned}
\tilde{\mathbf{N}} = {} & \frac{2G \operatorname{dev} \varDelta\mathbf{H} - 2G\varDelta\gamma\bar{\mathbf{N}}_m - \frac{1}{2}\tilde{\beta}G\varDelta\mu\tilde{\mathbf{N}}_n}{\frac{1}{2}\tilde{\beta}G\varDelta\mu} \\
& - \frac{(1 - k_h\rho_h)\varDelta\gamma(\bar{b}_1\bar{\mathbf{N}}_m - \sum_i b_i \operatorname{dev}\bar{\boldsymbol{\alpha}}_{i,n})}{\frac{1}{2}\tilde{\beta}G\varDelta\mu} \quad (i = 2,4,6)\,.
\end{aligned} \tag{3.70}
$$

Following Eq. (3.43), in the damage configurations, the current normalized mean transformed stress direction is given by

$$
\tilde{\mathbf{N}}_m = \frac{1}{2}(\tilde{\mathbf{N}} + \tilde{\mathbf{N}}_n)\,. \tag{3.71}
$$

Therefore, the corresponding plastic strain increment tensor is

$$
\varDelta\bar{\mathbf{H}}^{\mathrm{pl}} = \varDelta\gamma\bar{\mathbf{N}}_m\,, \tag{3.72}
$$

and the damage strain increment tensor is calculated as

$$
\varDelta\mathbf{H}^{\mathrm{da}} = \varDelta\mu(\tilde{\alpha}\frac{1}{\sqrt{3}}\mathbf{1} + \tilde{\beta}\tilde{\mathbf{N}}_m)\,. \tag{3.73}
$$

Hence, the total damage strain tensor is

$$
\mathbf{A}^{\mathrm{da}} = \mathbf{A}_n^{\mathrm{da}} + \varDelta\mathbf{H}^{\mathrm{da}}\,, \tag{3.74}
$$

and the current damage tensor $\overset{*}{\mathbf{R}}$ can be determined by the first Padé approximation (Brünig, 1999a)

$$
\overset{*}{\mathbf{R}} = [\mathbf{1} - \mathbf{A}^{\mathrm{da}}]^{-1}[\mathbf{1} + \mathbf{A}^{\mathrm{da}}]\,, \tag{3.75}
$$

and then, the damage transformation tensor $\mathbf{R}$ is given by

$$
\mathbf{R} = \mathbf{Q}_n^{\mathrm{el}-1}\overset{*}{\mathbf{R}}\mathbf{Q}_n^{\mathrm{el}}\,. \tag{3.76}
$$

As mentioned in Eq. (3.65), the elastic metric transformation tensor $\mathbf{Q}^{\mathrm{el}}$ tends to closely approximate the identity tensor $\mathbf{1}$ after initiation of damage. Thus, $\mathbf{Q}_n^{\mathrm{el}}$ is used in Eq. (3.76) to calculate the current damage strain tensor $\mathbf{R}$.

Moreover, substituting Eqs. (3.72) and (3.73) into Eq. (2.18), the elastic strain increment tensor can be computed in the form

$$\Delta\mathbf{H}^{\mathrm{el}} = \Delta\mathbf{H} - \Delta\gamma\mathbf{R}^{-1}\bar{\mathbf{N}}_m\mathbf{R} - \Delta\mu\mathbf{Q}_n^{\mathrm{el}-1}(\tilde{\alpha}\frac{1}{\sqrt{3}}\mathbf{1} + \tilde{\beta}\tilde{\mathbf{N}}_m)\mathbf{Q}_n^{\mathrm{el}}. \quad (3.77)$$

Then, the total elastic strain $\mathbf{A}^{\mathrm{el}}$ (3.24) and the current elastic metric transformation tensor $\mathbf{Q}^{\mathrm{el}}$ can be further calculated (3.25), respectively.

3.4.2 Consistent elastic-plastic-damage tangent modulus

As the current plastic strain increment $\Delta\bar{\mathbf{H}}^{\mathrm{pl}}$, the updated damage strain increment $\Delta\mathbf{H}^{\mathrm{da}}$, and the total elastic strain $\mathbf{A}^{\mathrm{el}}$ are known, the effective back stress increments (2.51), the damage back stress increment (2.64), as well as the stress tensor (2.40) can be calculated, respectively. Furthermore, the stress-state-dependent parameters $\hat{\alpha}$, $\hat{\beta}$, $\tilde{\alpha}$, $\tilde{\beta}$ and corresponding factors $w_1...w_4$ in (3.16) can be computed based on the newly obtained stress tensors ($\bar{\mathbf{T}}$ (2.38) and $\mathbf{T}$ (2.40)) and stress directions ($\bar{\mathbf{N}}_m$ and $\tilde{\mathbf{N}}_m$), and these are utilized to determine the consistent elastic-plastic-damage tangent modulus according to the above-mentioned numerical integration method.

In the damaged configurations, the stress differential is

$$\begin{aligned}
\mathrm{d}\mathbf{T} = \mathbb{C}^{\mathrm{epd}}\mathrm{d}\mathbf{H} &= \mathbb{C}^{\mathrm{el,d}}\mathrm{d}\mathbf{A}^{\mathrm{el}} + \mathbb{C}^{\mathrm{da}}\mathrm{d}\mathbf{A}^{\mathrm{da}} \\
&= \frac{\mathrm{d}\mathbf{T}}{\mathrm{d}\mathbf{A}^{\mathrm{el}}}\mathrm{d}\mathbf{A}^{\mathrm{el}} + \frac{\mathrm{d}\mathbf{T}}{\mathrm{d}\mathbf{A}^{\mathrm{da}}}\mathrm{d}\mathbf{A}^{\mathrm{da}},
\end{aligned} \quad (3.78)$$

where the elastic strain differential is

$$\mathrm{d}\mathbf{A}^{\mathrm{el}} = \mathrm{d}\mathbf{H}^{\mathrm{el}} = \mathrm{d}\mathbf{H} - \mathrm{d}\gamma\mathbf{R}^{-1}\bar{\mathbf{N}}_m\mathbf{R} - \mathrm{d}\mu\mathbf{Q}^{\mathrm{el}-1}(\tilde{\alpha}\frac{1}{\sqrt{3}}\mathbf{1} + \tilde{\beta}\tilde{\mathbf{N}}_m)\mathbf{Q}^{\mathrm{el}},$$

$$(3.79)$$

and $\mathbb{C}^{\mathrm{el,d}}$ is shown in Eq. (3.29). In addition, $\mathbb{C}^{\mathrm{da}}$ is expressed as

$$\mathbb{C}^{\mathrm{da}} = 2\eta_1 \operatorname{tr} \mathbf{A}^{\mathrm{el}} \mathbf{1} \otimes \mathbf{1} + 2\eta_2 \mathbf{A}^{\mathrm{el}} \otimes \mathbf{1} + \eta_3 \mathbf{1} \otimes \mathbf{A}^{\mathrm{el}} + \eta_3 \operatorname{tr} \mathbf{A}^{\mathrm{el}} \mathbb{1} + \eta_4 \mathbb{A}^{\mathrm{el}} \tag{3.80}$$

with

$$\mathbb{A}^{\mathrm{el}} = (\mathbf{A}^{\mathrm{el}})^i_{.k} \delta^l_{.j} + \delta^i_{.k} (\mathbf{A}^{\mathrm{el}})^l_{.j} \,.$$

It should be emphasized that $\mathrm{d}\gamma$ and $\mathrm{d}\mu$ are computed utilizing the above-mentioned numerical integration method. Thus, considering Eqs. (3.56), (3.60), (3.61), (3.62) and (3.63), one gets

$$\begin{bmatrix} \mathrm{d}\gamma \\ \mathrm{d}\mu \end{bmatrix} = \begin{bmatrix} m_1 & m_2 \\ m_3 & m_4 \end{bmatrix} \begin{bmatrix} \mathrm{d}\varepsilon_1 \\ \mathrm{d}\varepsilon_2 \end{bmatrix} . \tag{3.81}$$

with

$$\begin{bmatrix} m_1 & m_2 \\ m_3 & m_4 \end{bmatrix} = \begin{bmatrix} w_1 & w_2 \\ w_3 & w_4 \end{bmatrix}^{-1} - \mathbf{D}^{-1} \begin{bmatrix} k_h \rho_h \frac{\mathrm{d}\bar{c}}{\mathrm{d}\gamma} & 0 \\ 0 & \rho_s \frac{\mathrm{d}\tilde{\sigma}}{\mathrm{d}\mu} \end{bmatrix} \begin{bmatrix} w_1 & w_2 \\ w_3 & w_4 \end{bmatrix}^{-1} , \tag{3.82}$$

and

$$\mathbf{D} = \begin{bmatrix} \sqrt{2}\bar{G}_1 w_1 + k_h \rho_h \frac{\mathrm{d}\bar{c}}{\mathrm{d}\gamma} & \sqrt{2}\bar{G}_1 w_2 \\ \sqrt{2}G_2 w_3 & \sqrt{2}G_2 w_4 + \rho_s \frac{\mathrm{d}\tilde{\sigma}}{\mathrm{d}\mu} \end{bmatrix} . \tag{3.83}$$

Finally, inserting Eq. (3.81) into Eq. (3.78), the elastic-plastic-damage tangent moduli considering combined hardening and softening laws can be expressed as

$$\begin{aligned}
\mathbb{C}^{\mathrm{epd}} &= \mathbb{C}^{\mathrm{el,d}} - [\mathbb{C}^{\mathrm{el,d}}(\mathbf{R}^{-1}\bar{\mathbf{N}}_m\mathbf{R})] \otimes \left(\frac{m_1 \mathbf{Z}_1}{\sqrt{2}G} + \frac{m_2 \mathbf{Z}_3}{\sqrt{2}G_2} \right) \\
&\quad - \left[\mathbb{C}^{\mathrm{el,d}} \left(\frac{\tilde{\alpha}}{\sqrt{3}}\mathbf{1} + \tilde{\beta}\mathbf{Q}^{\mathrm{el}-1}\tilde{\mathbf{N}}_m\mathbf{Q}^{\mathrm{el}} \right) \right] \otimes \left(\frac{m_3 \mathbf{Z}_1}{\sqrt{2}G} + \frac{m_4 \mathbf{Z}_3}{\sqrt{2}G_2} \right) \tag{3.84} \\
&\quad + \left[\mathbb{C}^{\mathrm{da}} \left(\frac{\tilde{\alpha}}{\sqrt{3}}\mathbf{1} + \tilde{\beta}\tilde{\mathbf{N}}_m \right) \right] \otimes \left(\frac{m_3 \mathbf{Z}_1}{\sqrt{2}G} + \frac{m_4 \mathbf{Z}_3}{\sqrt{2}G_2} \right) .
\end{aligned}$$

3.5 Algorithmic implementation

The active set strategy (Kiefer et al., 2018; Simo et al., 1988) is used to correctly and effectively seek the respective constraints between the effective fictitious configurations and damaged configurations, respectively, in the proposed two-surface constitutive model. This adopted strategy satisfies the requirements of the Kuhn-Tucker conditions within different configurations. The main structure of the inelastic predictor-elastic corrector approach for the proposed constitutive model is summarized in Algorithm 1.

Algorithm 1 Inelastic predictor-elastic corrector

1: History variables: $\mathfrak{D} \in \{\mathbf{A}_n^{\text{el}}, \mathbf{A}_n^{\text{da}}, \bar{\mathbf{T}}_n, \mathbf{T}_n, \bar{\boldsymbol{\alpha}}_{i,n}, \bar{\boldsymbol{\alpha}}_n, \boldsymbol{\alpha}_n, \gamma_n, \mu_n\}$
2: Given strain filed: $\mathbf{A}^{\text{el,tri}} = \mathbf{A}_n^{\text{el}} + \Delta\mathbf{H}$
3: Compute and check the trial yield condition $f^{\text{pl,tri}}$ and the equivalent effective plastic strain increment $\Delta\bar{\gamma}$, as well as the trial damage condition $f^{\text{da,tri}}$, the equivalent plastic strain increment $\Delta\gamma$ and the equivalent damage strain increment $\Delta\mu$
4: **if** $f^{\text{pl,tri}} > 0$ and $\Delta\bar{\gamma} > 0$ **then**
5:     **if** $f^{\text{da,tri}} > 0$ and $\Delta\gamma > 0$ and $\Delta\mu > 0$ **then**
6:         go to elastic-plastic-damage part, see Section 3.4
7:         update $\mathbf{A}^{\text{el}}$, $\mathbf{A}^{\text{da}}$, $\mathbf{T}$ (2.40), $\bar{\boldsymbol{\alpha}}$, $\boldsymbol{\alpha}$, γ, μ, and $\mathbb{C}^{\text{epd}}$ (3.84)
8:     **end if**
9: **else**
10:     go to elastic-plastic part, see Section 3.3
11:     **if** $\mu_n > 0$ **then**
12:         update $\mathbf{A}^{\text{el}}$, $\mathbf{T}$ (2.40), $\bar{\boldsymbol{\alpha}}$, γ,and $\mathbb{C}^{\text{ep,d}}$ (3.55)
13:     **else**
14:         update $\mathbf{A}^{\text{el}}$, $\bar{\mathbf{T}}$ (2.38), $\bar{\boldsymbol{\alpha}}$, γ, and $\mathbb{C}^{\text{ep}}$ (3.53)
15:     **end if**
16: **else**
17:     go to elastic part, see Section 3.2
18:     **if** $\mu_n > 0$ **then**
19:         update $\mathbf{A}^{\text{el}}$, $\mathbf{T}$ (2.40), and $\mathbb{C}^{\text{el,d}}$ (3.29)
20:     **else**
21:         update $\mathbf{A}^{\text{el}}$, $\bar{\mathbf{T}}$ (2.38), and $\mathbb{C}^{\text{el}}$ (3.27)
22:     **end if**
23: **end if**

---

4 Experimental and numerical setups

Experiments with one-axis-loaded and biaxially loaded specimens have been performed to validate the proposed continuum damage model and to capture the mechanical response of the investigated ductile aluminum alloy EN AW 6082-T6. One-axis loaded monotonic and cyclic tension and shear tests (Wei et al., 2022, 2023d) are initially carried out to identify the material parameters. Subsequently, different proportional and non-proportional biaxial experiments (Wei et al., 2023b, 2024b) are conducted to verify the performance of the proposed continuum damage model under various complex loading conditions. According to previous
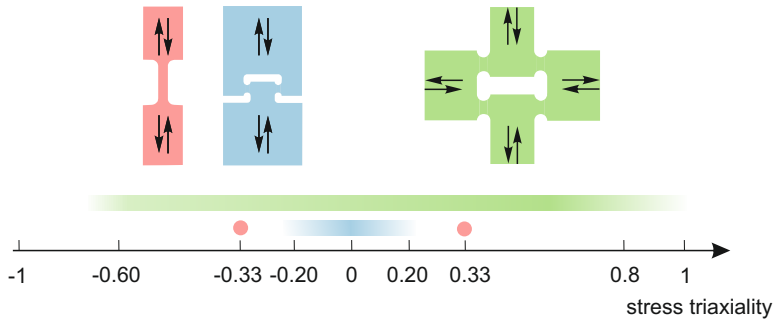
Figure 4.1: Attainable stress triaxiality for different specimens (Wei et al., 2023b).

numerical and experimental studies (Wei et al., 2022), see Fig. 4.1, the uniaxial tension and compression tests generate stress triaxialities of 0.33 and -0.33, respectively. In addition, the stress triaxialities induced by monotonic and cyclic shear tests fall within the range of approximately -0.2 to 0.2. One of the highlights of the newly designed experiments with thin metal sheets covers a wide range of stress triaxialities (from -0.60 to 0.8) under non-proportional biaxial reverse loading conditions, as illustrated in Fig. 4.1. This addresses a crucial gap in studying damage

and fracture behavior under cyclic biaxial loading. During the experiments, digital image correlation (DIC) technique records deformations and strain changes. Following the experiments, the fractured surfaces are examined by scanning electron microscopy (SEM). In Section 4.1, the material, geometries, and experimental setups and programs will be discussed in detail. Furthermore, the finite element mesh and material parameter identification strategy (Wei et al., 2022, 2023d) are presented in detail in Section 4.2.

4.1 Experimental aspects

4.1.1 Material and geometries of specimens

The medium strength aluminum-magnesium-silicon (AlSiMgMn) alloy EN AW 6082-T6, which is widely used in building structures, aircraft, and automobile constructions, is utilized to study the damage and fracture behavior under cyclic loading conditions. The chemical composition is shown in Table 4.1.

Table 4.1: Chemical composition of the aluminum alloy EN AW 6082-T6. The table is adapted from Wei et al. (2023b).

Al	Si	Mg	Mn	Fe	Zn	Cu	Ti	Others
To balance	0.90%	0.70%	0.47%	0.37%	0.09%	0.09%	0.03%	0.06%

The uniaxial tension-compression specimen (TC-specimen) and the one-axis-loaded shear specimen are shown in Fig. 4.2, respectively. Compared to the standard tensile specimen (Brünig et al., 2021a), the central compact part of the TC-specimen, as shown in Fig. 4.2(a), has been shortened to 21 mm with a quadratic 4 mm×4 mm cross-section for compression testing to avoid early buckling. Fig. 4.2(c) illustrates the geometry of the one-axis-loaded shear specimen, which has a double notch part in its center. The design of this new shear specimen, drawing inspiration from the performance of the notch in the biaxially loaded H-specimen proposed by Gerke et al. (2017), is specifically engineered to prevent rotation around the vertical axis as much as possible. In addition, the

details of the notched parts are depicted in Figs. 4.2(d) and (e), respectively. Moreover, the geometries of the biaxially loaded cruciform HC-specimen is shown in Fig. 4.3. As can be seen in Fig. 4.3(b), it
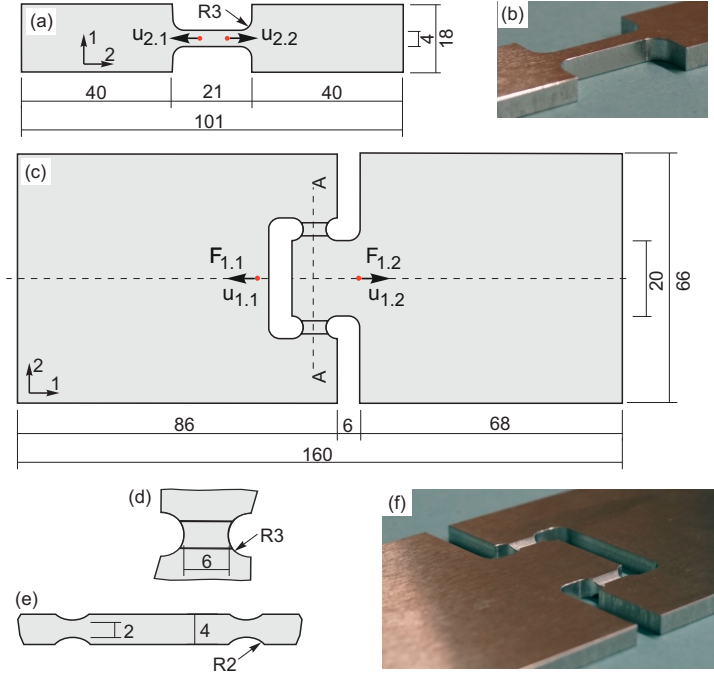

Figure 4.2: One-axis-loaded geometries: (a) TC-specimen, (b) isometric photo of the TC-specimen, (c) shear specimen, (d)-(e) details of the notch parts of the shear specimen, and (f) isometric photo of the shear specimen; all units in mm, thickness 4 mm (Wei et al., 2022).

has four 2 mm thick notches in its center, and the distances between the notches in the horizontal and vertical directions are 32 mm and 8 mm, respectively, to allow imposing the cyclic loading on both axes. This design is similar to the H-specimen but differs in that the distances in the vertical direction have been increased from 2 mm to 8 mm. In addition, tension or compression stresses are obtained when the load is subjected

to the horizontal axis (axis 1), whereas the shear stresses occur with
loading along the vertical axis (axis 2). Hence, non-proportional biaxial
reverse experiments are achieved by altering the loading directions and
axes using the HC-specimen.

Furthermore, the relative displacement Δu_{ref} is introduced to character-
ize the load-displacement curves during the experimental and numerical
analysis. For the TC-specimen and the shear specimen, it is defined as

$$\Delta u_{i,\mathrm{ref}} = u_{i.1} + u_{i.2} \tag{4.1}$$

between the two measuring points, as plotted in Figs. 4.2(a) and (c),
respectively. Similarly, the relative displacements for the HC-specimen
are calculated between the measuring points in axis 1 and 2 are shown
in Fig. 4.3(e), respectively. In addition, the mean forces F_i

$$F_i = \frac{F_{i.1} + F_{i.2}}{2} \tag{4.2}$$

are used for the load-displacement analysis for all above discussed spec-
imens.
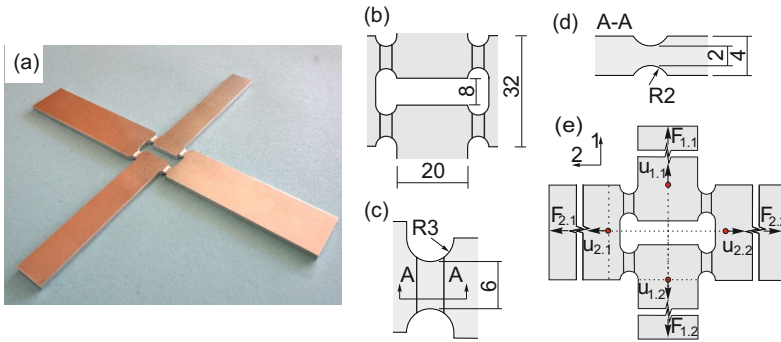
Figure 4.3: Biaxially loaded HC-specimen: (a) isometric photo of the
HC-specimen, (b)-(d) details of the notch parts, (e) loading
and measurement points (red); all units in mm, thickness
4 mm (Wei et al., 2023b).

4.1.2 Experimental setups

Testing machines, DIC setups, and SEM

The one-axis-loaded experiments are conducted on the standard electro-mechanical testing machine Inspekt Table 50-1 manufactured by Hege-wald & Peschke, Germany. All experiments are performed under quasi-static loading conditions with a machine speed of 0.05 mm/min. As illus-trated in Fig. 4.4, the DIC setups includes four 6 Mpx cameras mounting 75 mm lenses, two LED lights type FL-B50, and two LED lights type FL-B25. On each side, two cameras monitor the front and back side of the specimen, and all cameras are calibrated into a unified system us-ing a specially designed double-sided target. Moreover, the same LED lights combinations, i.e., FL-B50 and FL-B25, are used in both sides of the specimen to provide sufficient brightness without creating shad-ows and reflection around the region of interest (ROI) of the specimens. Prior to conducting the experiments, the specimens are sprayed with
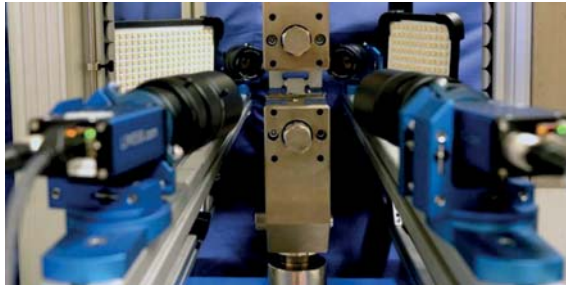
Figure 4.4: DIC setups for one-axial experiments: lighting system and camera equipment (Wei et al., 2022).

white acrylic paint and subsequently coated with graphite, creating a black spot pattern. The average resolution at the center of the one-axis-loaded specimens is approximately 56 px/mm. Istra 4D, from the commercial company Limess/Dantec, is utilized for the analysis of ex-perimental data, with special emphasis on calculating the physical strain directly from the distortions of the facet. During the experimental evalu-ation, the subset (facet size) is set to 33 px and the grid spacing (overlap)

is selected to 11 px, respectively. These settings are recommended by the manufacturer (Limess/Dantec), consistent with the recommendations for good practice (Jones et al., 2018). Moreover, displacement or contour smoothing is not taken into account. The region of interest (ROI) for the TC-specimen is chosen as 1168 px in width and 501 px in height, and 2752 px in width and 2206 px in height for the shear specimen.

The biaxial experiments are performed using the horizontally arranged electro-mechanical testing machine LFM-BIAX 20 kN, which was manufactured by Walter + Bai, Switzerland, under quasi-static loading conditions with a machine speed of 0.004 mm/s. The experiments employ
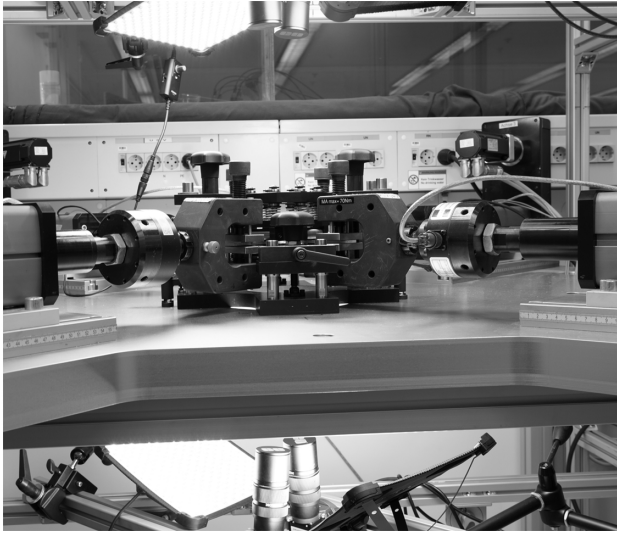
Figure 4.5: DIC setups for biaxial experiments with down-holder: lighting system and camera equipment.

the same cameras and LED lights as those utilized in the one-axis-loaded experiments, with the DIC setups depicted in Fig. 4.5. The average resolution at the center of the biaxially loaded specimens is about 60 px/mm. The subset and the grid spacing are set to match the one-axis-loaded tests, i.e., 33 px and 11 px. In addition, the ROI is defined as 2752 px × 2206 px.

After the experiments, the fractured surfaces are examined by scanning electron microscopy (SEM) with ZEISS EVO 15 with lanthanum hexaboride electron emitter (LaB6) and Everhart-Thornley (ET) detector to confirm the proposed damage mechanisms. Imaging is conducted in a high vacuum environment, maintaining a working distance of approximately 11 mm, an electron beam diameter (spot-size) of 300 nm, and an accelerating voltage of 20 kV.

Clamping jaws and anti-buckling devices

Different clamping jaws are used to perform different one-axial experiments: (1) a wedge grip up to 40 kN (Fig. 4.6(a)) for tensile loading with TC-specimens; (2) anti-buckling device (THS613:50 kN), see Fig. 4.6(b), for uniaxial compression test using TC-specimens; (3) Jaws with screw-action grip (THS90-BP), as illustrated in Fig. 4.6(c), for one-axial shear test.

(a)   (b)   (c)
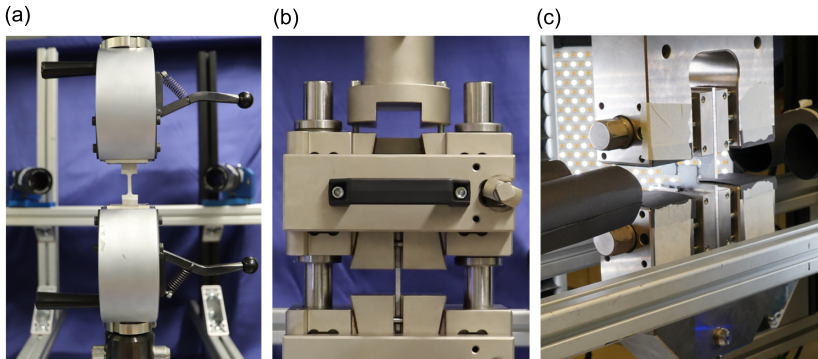
Figure 4.6: Clamping jaws: (a) wedge grip 40 kN, (b) anti-buckling device (THS613:50 kN), and (c) clamping with screw-action grip (THS90-BP).

Initially designed for composite compression, the anti-buckling device (THS613:50 kN) is well-suited for flat specimens up to 30 mm wide and 6 mm thick. Moreover, this device automatically aligns itself and delays buckling significantly. The TC-specimen is secured in the anti-buckling

device as follows. First, remove the clamping jaws from the anti-buckling taper wedge device. Then, position the TC-specimen centrally within the clamping jaws and secure it by tightening the jaw screws. Finally, the clamping jaws are reinserted into the anti-buckling device with the TC specimen. The DIC technique allows for the evaluation and analysis of experimental data across different series using the same specimen, with cameras and lights fixed in position. Hence, the idea arose to alternate between using tensile wedge grips and an anti-buckling device for uniaxial tension-compression cyclic loading tests to avoid buckling and provide reliable results.

In addition, the shear cyclic experiments are conducted using the screw-action grip THS90-BP, which enables the imposition of both tensile and compressive loads. It should be noted that this device must be aligned carefully to avoid eccentricities as much as possible. These clamping jaws are employed with the one-axis-loaded shear specimen, offering greater robustness against buckling than the TC-specimen.

(a)   (b)
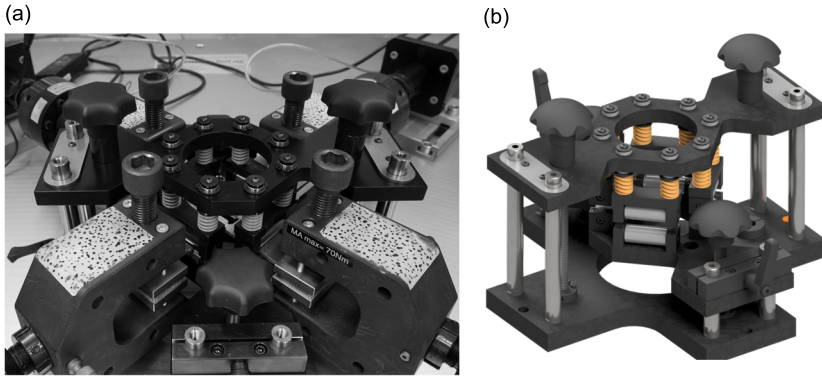
Figure 4.7: Clamping jaws with down-holder in biaxial testing machine(a) and down-holder(b).

Furthermore, as shown in Fig. 4.7, a newly designed down-holder in co-operation with Walter + Bai is incorporated to restrict the perpendicular displacements on the surface of the HC-specimen. The central opening is purposefully designed to accommodate the DIC technique. Additionally, it features a stationary base and a mobile upper section fitted with

a coiled spring. Rollers incorporated into the down-holder provide adequate and consistent contact with the HC-specimen. It is imperative to ensure precise alignment of the base of the down-holder with the base of the machine plate through swivel brackets to prevent interference with DIC usage (Fig. 4.5). In addition, the height of the lower roller bearings is meticulously adjusted using rotary controls and subsequently verified through both visual and acoustic inspections following the installation of the cross-check. It is essential to align the base's height with the clamping jaws' bottom. Following the installation of the HC-specimen, the mobile upper section of the down-holder is affixed and subjected to preloading using springs, which are tightened by rotary controls, guaranteeing that the specimen receives sufficient support from the roller, as shown in Fig. 4.7(b).

4.1.3 Experimental programs

The test naming rule includes three parts: the first part refers to the specimen type; the second part indicates between monotonic (mon), single cyclic (cyc), and bi-cyclic (cyc^2) loading; and the third part alters between one-axial and biaxial experiments. This could be the loading sequence for one-axial experiments or the preload and loading pattern in biaxial tests. A detailed explanation is discussed in this section.

One-axial experiments

The uniaxial monotonic tensile and compression tests are conducted to study the strength-differential effect (SD-effect) and to calibrate the material parameters. Various cyclic loading patterns are designed to observe the Bauschinger effect. Moreover, both monotonic and cyclic shear tests are performed to distinguish between the damage mechanisms induced by tension-dominated and shear-dominated (near zero) stress states. The test classifications are summarized in Table 4.2. The test ID for one-axial experiments consists of three parts: the specimen, the loading pattern, and the loading sequence. In addition, TC and S refer to the tension-compression and shear specimen, respectively, while the symbols cyc and mon are abbreviations for cyclic and monotonic loadings, respectively.

Table 4.2: Test classifications for one-axial experiments.

Test ID	Specimen	Loading pattern
TC-mon-T	TC-specimen	Monotonic tension
TC-cyc-TCT	TC-specimen	Tension-compression-tension
TC-cyc-TCTCT	TC-specimen	Tension-compression-tension-compression-tension
TC-cyc-CT	TC-specimen	Compression-tension
TC-cyc-CTCT	TC-specimen	Compression-tension-compression-tension
S-mon-T	Shear specimen	Monotonic tension
S-cyc-TCT	Shear specimen	Tension-compression-tension
S-cyc-TCTCT	Shear specimen	Tension-compression-tension-compression-tension
S-cyc-CT	Shear specimen	Compression-tension
S-cyc-CTCT	Shear specimen	Compression-tension-compression-tension

Biaxial experiments

The proportional and non-proportional biaxial reverse experiments using HC-specimens are performed to generate a wide range of stress triaxialities, with the aim of investigating stress-state-dependent ductile damage and fracture behavior. In the present work, single cyclic loading superimposed with different preloads without unloading, and bi-cyclic loading experiments are designed. The symbols cyc and cyc^2 represent the single cyclic loading and bi-cyclic loading tests, respectively. Compared to the one-axial experiments, only the cyclic loading pattern TCT is selected to study the ductile damage and fracture behavior under reverse loading conditions.

In the single cyclic experiments, shear or tensile preloads are subjected to axis 1 or axis 2 to achieve the target forces without unloading. Subsequently, the TCT cyclic loading is imposed on axis 2 or axis 1. As shown in Table 4.3, the different tensile or compressive preloads $0\,\mathrm{kN}$, $\pm3\,\mathrm{kN}$, and $\pm5\,\mathrm{kN}$ are first imposed on axis 2 (horizontal axis, as shown in Fig. 4.3(e)) at the loading stage 1. Then, the TCT shear cyclic loading is superimposed on the axis 1 (vertical axis, as shown in Fig. 4.3(e)) until specimens failed during the second loading stage. Moreover, similar nomenclature is used for the biaxially loaded experiments. HC is the abbreviation for the used HC-specimen. The notations mon-Tx and cyc-Tx denote the monotonic or cyclic loading imposed on axis 1 superimposed by $F_2 = x\,\mathrm{kN}$ in axis 2. Also, u_1^{M} and u_2^{M} describe the machine displacements of cylinder 1 and cylinder 2, respectively. In addition, a schematic

diagram of the experimental loading paths is presented in Fig. 4.8.

Table 4.3: Test classifications for single biaxial cyclic experiments superimposed by tensile or compressive preloads (Wei et al., 2023b).

Test ID	Stage 1	Stage 2	
	u_2^{M} [mm]	u_1^{M} [mm]	F_2 [kN]
HC-mon/cyc-T0	until reaction force $F_2 = 0\,\mathrm{kN}$	mon./cyc. until fracture	0
HC-mon/cyc-T3	until reaction force $F_2 = 3\,\mathrm{kN}$	mon./cyc. until fracture	3
HC-mon/cyc-TN3	until reaction force $F_2 = -3\,\mathrm{kN}$	mon./cyc. until fracture	-3
HC-mon/cyc-T5	until reaction force $F_2 = 5\,\mathrm{kN}$	mon./cyc. until fracture	5
HC-mon/cyc-TN5	until reaction force $F_2 = -5\,\mathrm{kN}$	mon./cyc. until fracture	-5
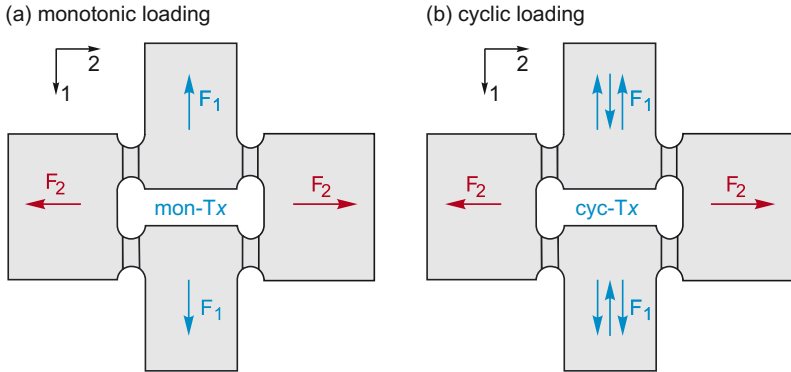
Figure 4.8: Schematic diagram of the experimental loading paths. Tensile or compressive preload F_2 is illustrated as red arrows, and superimposed monotonic or cyclic load F_1 is depicted as blue arrows (Wei et al., 2023b).

Moreover, the positive shear preloads $0\,\mathrm{kN}$, $4.5\,\mathrm{kN}$ and $5\,\mathrm{kN}$ applied along axis 1 (vertical axis) are superimposed by the tensile cyclic loading pattern TCT along axis 2 (horizontal axis), respectively. The test classifications are summarized in Table 4.4. The notations mon-Sx and cyc-Sx denote the monotonic or cyclic loading imposed on axis 2 superimposed by $F_1 = x\,\mathrm{kN}$ in axis 1. Notably, different compressive displacements

(C) in the TCT (stage 2) loading patterns are selected to investigate the influence of the degree of compressive displacements on the mechanical response of the material, denoted as symbols i and ii, respectively. Also, Fig. 4.9 shows the schematic diagram of experimental loading paths.

Table 4.4: Test classifications for single biaxial cyclic experiments superimposed by shear preloads (Wei et al., 2024b).

Test ID	Stage 1 u_1^{M} [mm]	Stage 2 F_1 [kN]	u_2^{M} [mm]
HC-mon-S0	-	0	mon. until fracture
HC-mon-S4.5	until reaction force $F_1 = 4.5\,\mathrm{kN}$	4.5	mon. until fracture
HC-cyc-S4.5-i	until reaction force $F_1 = 4.5\,\mathrm{kN}$	4.5	cyc. until fracture
HC-cyc-S4.5-ii	until reaction force $F_1 = 4.5\,\mathrm{kN}$	4.5	cyc. until fracture
HC-mon-S5	until reaction force $F_1 = 5\,\mathrm{kN}$	5	mon. until fracture
HC-cyc-S5-i	until reaction force $F_1 = 5\,\mathrm{kN}$	5	cyc. until fracture
HC-cyc-S5-ii	until reaction force $F_1 = 5\,\mathrm{kN}$	5	cyc. until fracture
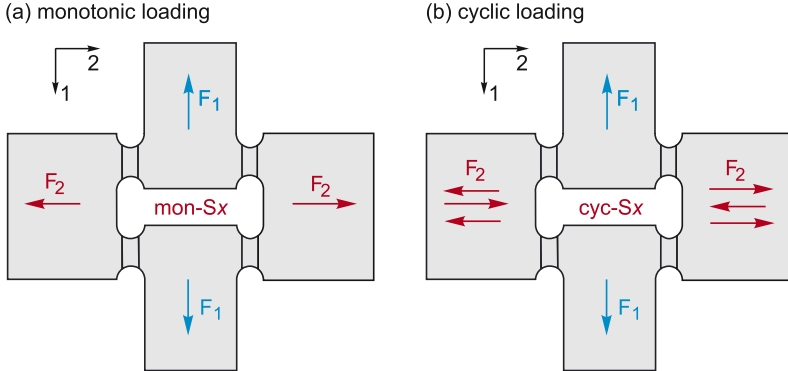
Figure 4.9: Schematic diagram of the experimental loading paths. Shear preload F_1 is illustrated as blue arrows, and superimposed monotonic or cyclic load F_2 is depicted as red arrows (Wei et al., 2024b).

Regarding the bi-cyclic experiments, both axes of the HC-specimens are subjected to cyclic loading simultaneously until the specimens fail. A schematic diagram for the loading paths is illustrated in Fig. 4.10. Cur-
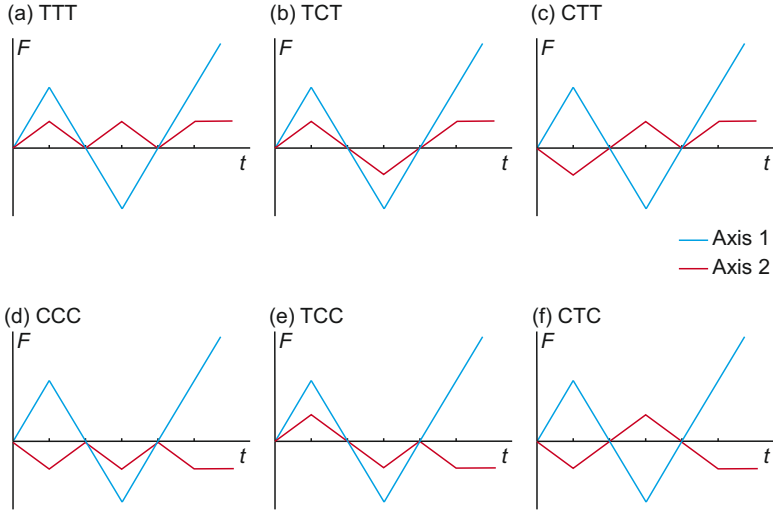
Figure 4.10: Schematic diagram of the bi-cyclic biaxial experimental loading paths (Wei et al., 2024a).

Table 4.5: Test classifications for bi-cyclic biaxial experiments.

Test ID	LP1		LP2		LP3			
					Stage1		Stage2	
	u_1^{M}	u_2^{M} till F_2 [kN]	u_1^{M}	u_2^{M} till F_2 [kN]	u_1^{M}	u_2^{M} till F_2 [kN]	u_1^{M}	F_2 [kN]
HC-cyc²-TTT3	+	3	-	3	+	3	Fx	3
HC-cyc²-TTT5	+	5	-	5	+	5	Fx	5
HC-cyc²-TCT3	+	3	-	-3	+	3	Fx	3
HC-cyc²-TCT5	+	5	-	-5	+	5	Fx	5
HC-cyc²-CTT3	+	-3	-	3	+	3	Fx	3
HC-cyc²-CTT5	+	-5	-	5	+	5	Fx	5
HC-cyc²-CCC3	+	-3	-	-3	+	-3	Fx	-3
HC-cyc²-CCC5	+	-5	-	-5	+	-5	Fx	-5
HC-cyc²-TCC3	+	3	-	-3	+	-3	Fx	-3
HC-cyc²-TCC5	+	5	-	-5	+	-5	Fx	-5
HC-cyc²-CTC3	+	-3	-	3	+	-3	Fx	-3
HC-cyc²-CTC5	+	-5	-	5	+	-5	Fx	-5

Note: $+/-$ indicates tensile or compressive loading, and Fx signifies fracture.

rently, the newly designed experiments focus on the shear cyclic loading (TCT, see blue lines in Fig. 4.10) along axis 1 superimposed with different kinds of tensile or compressive cyclic loading patterns on axis 2, i.e., TTT, TCT, CTT, CCC, TCC, and CTC, as the red lines shown in Fig. 4.10. It should be emphasized that the maximum or minimum forces in the first and second tensile cyclic loading patterns are restricted to $3\,\mathrm{kN}$ and $5\,\mathrm{kN}$ or $-3\,\mathrm{kN}$ and $-5\,\mathrm{kN}$, respectively. Most importantly, if the target forces in the last loading pattern reach $\pm 3\,\mathrm{kN}$ or $\pm 5\,\mathrm{kN}$, the loads are kept constant until failure. The corresponding test classifications are listed in Table 4.5.

4.2 Numerical aspects

4.2.1 FE mesh

Concerning numerical analysis, Solid185 elements with default settings in Ansys are utilized. In the one-axial shear tests, one-half of the spec-
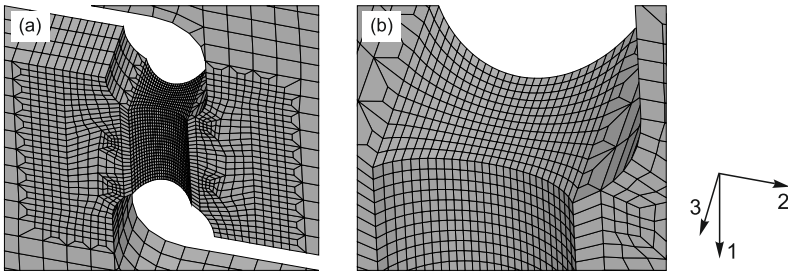
Figure 4.11: Mesh of the one-axis-loaded shear specimen: (a) overview, (b) details of the notched part (Wei et al., 2022).

imen with 15,037 elements is analyzed, considering the symmetry of the one-axis-loaded shear specimen. Additionally, mesh refinement is applied in the notched part where damage is expected to occur in the numerical simulations, see Fig. 4.11. Similarly, as depicted in Figs. 4.12(a) and (b), one-quarter of the HC-specimen with 22,502 elements, incorporating mesh refinement in the notched part, is used to analyze the material
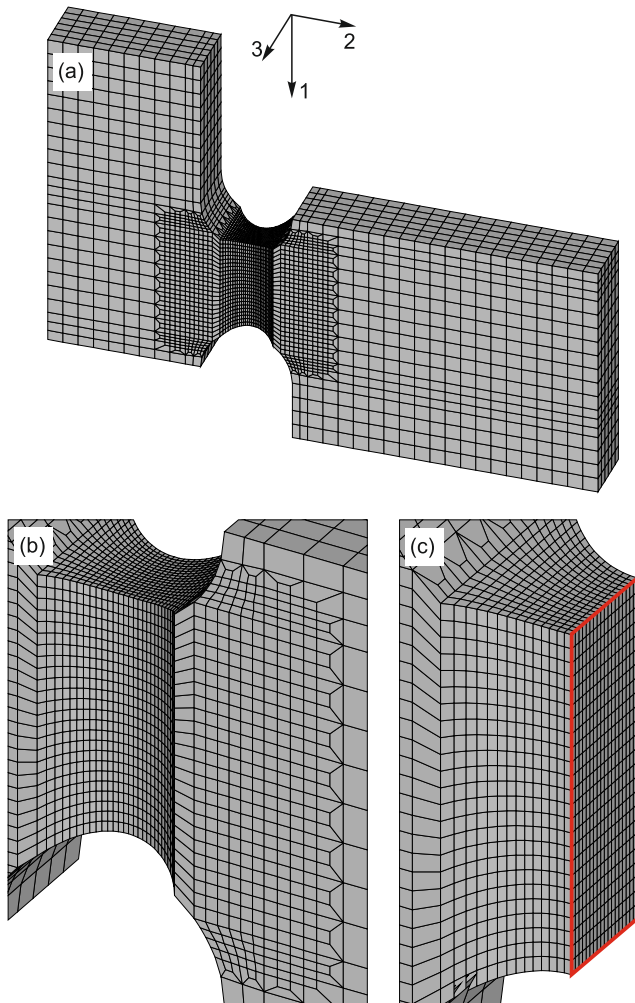
Figure 4.12: Mesh of the HC-specimen: (a) overview, (b) and (c) details of the notched part and the notched cross-section (Wei et al., 2023b).

response for different biaxial experiments. Moreover, the selected element dimensions at the center of the notched region for the shear and HC-specimens are $0.25\,\text{mm} \times 0.125\,\text{mm} \times 0.1\,\text{mm}$ along axes 1, 2, and 3, see Figs. 4.11(b) and 4.12(b). It is worth noting that the mesh sizes are determined based on mesh studies, which provide consistency with the distribution of the strain localization band measured from DIC, especially regarding the bandwidth on the notch surface. This approach yields reliable numerical results for comparing with experimental observations and predicting material behavior. Such predictions, including stress triaxialities and the evolution of plastic strains, cannot be directly measured experimentally. This contrasts with traditional mesh studies, which solely focus on identifying the mesh size that provides stable numerical results. However, these may not characterize the material behavior in the local strain fields with high accuracy.

Furthermore, the stress triaxiality η and the Lode parameter ω are widely used to capture the stress states during the numerical analysis. In accordance with previous studies, the stress triaxiality η and the Lode parameter ω are uniformly distributed with a gradient over the notched cross-section of the shear specimen (Wei et al., 2023d) and the H-specimen (Brünig et al., 2021c; Zistl et al., 2022a). To more accurately capture the stress state over the notched cross-section, the mean stress triaxiality $\bar{\eta}$ and the mean Lode parameter $\bar{\omega}$ (Wei et al., 2023b, 2022)

$$\bar{\eta} = \frac{1}{S} \int_0^S \eta ds \quad \text{and} \quad \bar{\omega} = \frac{1}{S} \int_0^S \omega ds \tag{4.3}$$

are introduced, where S represents the total area of the notched cross-section, as illustrated in Fig. 4.12(c).

4.2.2 Parameter calibration

Elastic and plastic hardening parameters

Based on the uniaxial tension test as shown in Fig. 4.13(a) (Wei et al., 2022), Young's modulus is measured as $E = 67500\,\text{MPa}$, and Poisson's ratio is given by $\nu = 0.29$. In addition, it is observed that the mean flow stress in tension $\sigma_m^t = 268.8\,\text{MPa}$ is lower than in compression $|\sigma_m^c| = 273.5\,\text{MPa}$, as shown in Fig. 4.13(b). Thus, the hydrostatic stress

coefficient is computed as
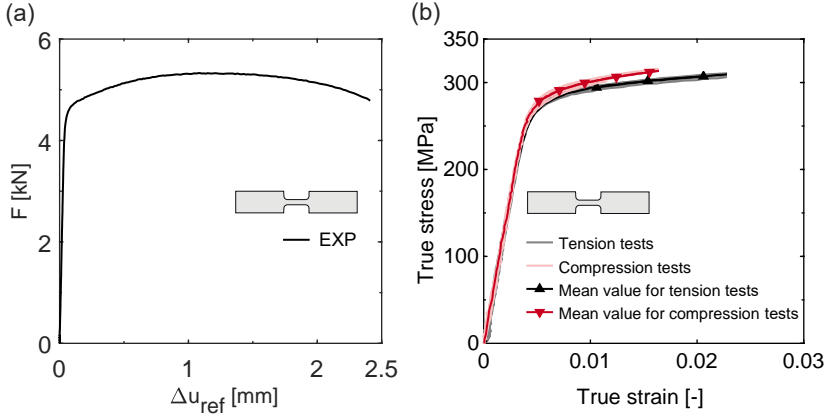
Figure 4.13: (a) The load-displacement curve for the uniaxial mono-
tonic tensile test and (b) the true stress-strain curves
for tension and compression tests with absolute values.
The tensile experimental curves are considered only up
to $\Delta u_{\mathrm{ref}} = 0.1\,\mathrm{mm}$ and all experimental data and corre-
sponding pictures are cited from Wei et al. (2022).

$$2a = S - D = 2 \times \frac{|\sigma_m^c| - \sigma_m^t}{|\sigma_m^c| + \sigma_m^t} \approx 1.7\%\,, \tag{4.4}$$

and the ratio $\frac{a}{c}$ keeps constant and is subsequently calculated as

$$\frac{a}{c} = \frac{a}{(1 + a)\sigma_m^t} = \frac{a}{(1 - a)\,|\sigma_m^c|} = 32\,\mathrm{TPa}^{-1} \tag{4.5}$$

according to Spitzig and Richmond (1984).

Moreover, the plastic and damage parameters can be independently cali-
brated as the plastic hardening and damage softening parameters do not
influence each other. Because damage is assumed to rapidly develop after
the significant localization of plastic strain (after the beginning of neck-
ing) in uniaxial tension tests, the plastic parameters are calibrated using
experimental data obtained before the occurrence of necking. Although

damage may occur earlier, before necking, its influence on material studies is often considered negligible. However, this effect can be reconsidered in the reverse fitting of damage parameters procedure.

As discussed in Wei et al. (2023d), the isotropic and kinematic hardening parameters can be identified by using the equivalent stress $\bar{c}$ – equivalent plastic strain γ curve (Fig. 4.14(a)) and the equivalent back stress $\bar{\alpha}$ – equivalent plastic strain γ curve (Fig. 4.14(b)). These curves are derived from the original load–displacement curve obtained during the uniaxial tension test (Fig. 4.13(a)). The fitting of material parameters is based on the least-square method provided in Matlab, which searches for the optimal parameter set that satisfies the following governing equation

$$\min_{\mathbf{x}} \|\mathbf{F}(\mathbf{x},\gamma) - y\|_2^2 = \min_{\mathbf{x}} \sum_i (\mathbf{F}(\mathbf{x},\gamma_i) - y_i)^2 \quad \text{with} \quad y \in \{\bar{c},\bar{\alpha}\}. \quad (4.6)$$

Different vector-based functions $\mathbf{F}(\mathbf{x},\gamma)$ are chosen based on the formulation of effective equivalent stress $\bar{c}$ in the isotropic hardening model (2.48) and the equivalent effective back stress $\bar{\alpha}$ for the integrated form of the kinematic hardening rule (2.51) for uniaxial tests, where $\bar{\alpha}$ is given by

$$\bar{\alpha} = \frac{b_1}{b_2}(1 - e^{-b_2\gamma}) + \frac{b_3}{b_4}(1 - e^{-b_4\gamma}) + b_5\gamma. \quad (4.7)$$

It is important to note that the uniaxial tension test provides an almost homogeneous stress state before necking. Therefore, the non-linear recovery term in $\dot{\bar{\boldsymbol{\alpha}}}_3$ (2.51) can be neglected under assumption that $b_6 = 0$. In addition, $\mathbf{x}$ represents the material parameter vector necessary for the used isotropic or kinematic hardening model.

Table 4.6: Plastic parameters.

c_0[MPa]	Q_1[MPa]	Q_2[MPa]	p_1[−]	p_2[−]	ρ_h[−]	
139	74.93	21.31	8.96	676.01	0.41	
b_1[MPa]	b_2[−]	b_3[MPa]	b_4[−]	b_5[MPa]	b_6[−]	$a/\bar{c}$ [TPa^{-1}]
61250	1750	895	15	115	7.5	32

As shown in Fig. 4.14, the numerically fitted curves agree well with the experimental ones and the corresponding plastic hardening parameters

are listed in Tab. 4.6. It is worth noting that the originally fitted kinematic hardening parameters b_1 and b_2 are 12250 MPa and 350, respectively. Taking into account the exponential Decay function χ (2.52) in the first back stress rate tensor $\dot{\bar{\alpha}}_1$ (2.51), parameters b_1 and b_2 should be multiplied by 5, resulting in $b_1 = 61250$ MPa and $b_2 = 1750$.
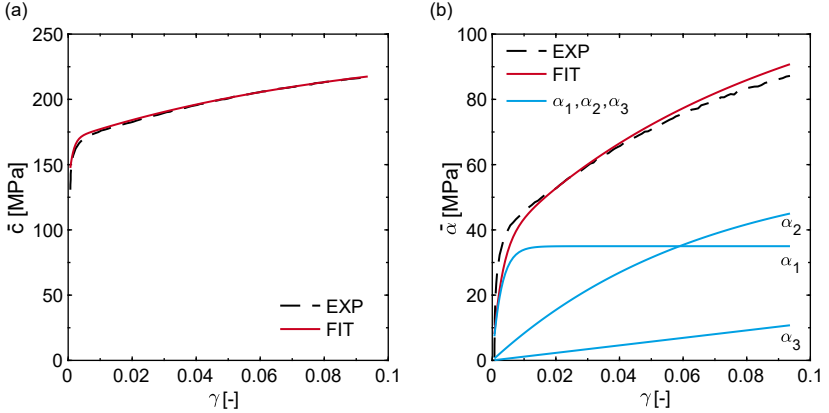

Figure 4.14: (a) Experimental and fitted $\bar{c} - \gamma$ curves and (b) experimental and fitted $\bar{\alpha} - \gamma$ curves (Wei et al., 2023d).

Additionally, the kinematic hardening parameter b_6 is inversely calibrated by solving governing equation

$$\kappa = \underset{\kappa}{\mathrm{argmin}} \left(\sum_j \left| \frac{F_j^{\mathrm{num}}(\kappa) - F_j^{\mathrm{exp}}}{F_j^{\mathrm{exp}}} \right| \right) \quad \text{with} \quad j \in D_{\mathrm{exp}} \tag{4.8}$$

with objective parameter defined as $\kappa = b_6$ and a set of identification experiments D_{exp}, including one-axial monotonic tension and shear tests. It is evident that no significant difference is observed in load–displacement curves before point A ($\Delta u_{\mathrm{ref}} = 0.6$ mm) when varying the b_6 parameters, as plotted in Fig. 4.15(a). This is attributed to the angle parameter $\cos^2 \theta$ (2.51 and 2.53), which is almost close to 1, as detailed in Wei et al. (2022). Nevertheless, as b_6 increases, the slope between points A and B on the load–displacement curve decreases. As depicted in Fig. 4.15(a), the nu-

merical result overestimates the experimental one when $b_6 = 0$, whereas the numerical result with $b_6 = 13.5$ underestimates it. Moreover, the numerically predicted results for the uniaxial tension test illustrated in Fig. 4.15(b) suggest that the kinematic hardening parameter b_6 has a minimal impact on the monotonic tensile load–displacement curves.
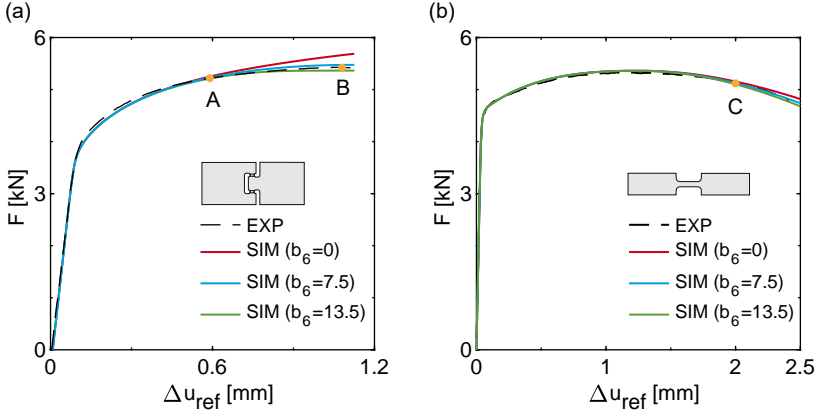

Figure 4.15: Experimental and numerical load–displacement curves for the one-axial shear test (a) and the uniaxial tension test (b) (Wei et al., 2023d).

Finally, the isotropic hardening ratio ρ_h can also be inversely determined considering the minimization function (4.8) with $\kappa = \rho_h$ through the uniaxial tension-compression (TC) test conducted within a small strain range ($\leq 5\%$), as shown in Fig. 4.16. This approach helps to avoid the influence of damage and buckling on the yield stress after reverse loading while also providing a homologous stress state. As depicted in Fig. 4.16, the numerically predicted yield stress after reverse loading with the isotropic hardening model ($\rho_h = 1$, Eq. (2.48)) is significantly greater than that one considering only the proposed kinematic hardening model ($\rho_h = 0$, Eq. (2.51)). It is evident that relying solely on a pure isotropic or kinematic hardening model results in either an overestimation or underestimation of the yield stress after reverse loading condition. On the other hand, the combined hardening approach with the hardening ratio $\rho_h = 0.41$ demonstrates a remarkable agreement with the experi-

mental one. Moreover, the pure extended double Voce-hardening (2.48) fails to capture the nonlinear properties under reverse loading condition. In contrast, the modified nonlinear Chaboche kinematic and combined hardening model, considering three back stress components, can aptly describe the nonlinearity after reverse loading, as illustrated in Fig. 4.16.
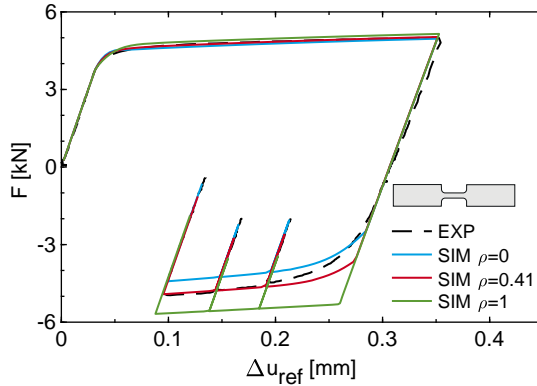

Figure 4.16: Experimental and numerical load–displacement curves for uniaxial tension-compression (TC) with three unloading patterns after compression (Wei et al., 2023d).

Damage softening parameters

The damage related parameters are listed in Table 4.7.

Table 4.7: Damage parameters.

$\tilde{\sigma}_0$ [MPa]	C_1[MPa]	C_2 [-]	d_1 [MPa]	d_2 [-]	$\eta_1...\eta_4$ [MPa]	$\rho_s[-]$
320	0.004207	92.97	-0.51	-84	-10000	0.41

As discussed in Section 2.5, the stress-state-dependent damage parameters $\hat{\alpha}$ and $\hat{\beta}$ (2.57) in the damage condition (2.56), as well as $\tilde{\alpha}$ (2.61) and $\tilde{\beta}$ (2.62) in the damage evolution equation (2.60), are calibrated by analyzing the mechanical behavior of a unit-cell containing 3% void volume in terms of the representative volume element (RVE) concept. The

details of the proposed approach and the corresponding material fitting pressure are discussed in Brünig et al. (2013, 2016). Most recently, Wei et al. (2023b) introduced this RVE approach to identify the damage softening parameter C_1, C_2, d_1, and d_2 (2.64 and 2.65). Thus, the equivalent damage stress $\tilde{\sigma}$ (2.65), the equivalent back damage stress α_{eq} (2.64), and the corresponding equivalent damage strain μ (2.65 and 2.64) can be calculated through numerical simulations involving monotonic and cycling loading conditions within the unit-cell. Subsequently, the softening parameters C_1, C_2, d_1, and d_2 can be determined using Eqs. (2.64) and (2.65). Most importantly, these softening parameters must be validated through a large number of proportional and non-proportional monotonic or cyclic experiments, see Wei et al. (2023a,b,c, 2024b). In addition, the elastic-damage material parameter $\eta_1...\eta_4 = -10000\,\text{MPa}$ (2.40) are inversely identified in Brünig et al. (2021c) and Wei et al. (2022), and the softening ratio ρ_s is assumed to be equal to the isotropic hardening ratio ρ_h.

5 Results and Discussions

As introduced in Chapter 4, digital image correlation (DIC) is employed to monitor changes in deformations and strains during the experiments. Consequently, the numerical results are compared with the experimental ones, focusing on global load–displacement curves and local strain fields. Additionally, scanning electron microscopy (SEM) images taken from fractured surfaces are utilized to validate the proposed damage mechanisms. The stress state, characterized by the mean stress triaxiality and the mean stress Lode parameter, along with the distribution of damage strains, is analyzed to elucidate the damage mechanism using SEM pictures.

5.1 Uniaxial tension tests

5.1.1 Global load–displacement curves

The experimental and numerical load–displacement curves for the monotonic and cyclic tension–compression tests are shown in Fig. 5.1. The numerical results agree well with the experimental ones. Notably, the proposed cyclic elastic-plastic-damage model accurately predicts the yield stresses after each reverse loading condition. Moreover, the monotonic tension test (TC-mon-T) failed at the displacement $\Delta u_{2,\mathrm{ref}} = 2.39\,\mathrm{mm}$ with a fracture force of $F_2^{\mathrm{fr}} = 4.82\,\mathrm{kN}$, see Fig. 5.1(a). The relative reverse fracture displacements $\Delta u_{2,\mathrm{rel}}^*$ for the TC-cyc-TCT and TC-cyc-TCTCT experiments are 1.94 mm and 1.66 mm, respectively. These values are significantly smaller than those observed in the TC-mon-T test. It should be noted that the relative reverse fracture displacement in axis 2 $\Delta u_{2,\mathrm{rel}}^*$ is defined from the point of zero force to the final fracture after the last reverse loading. In addition, the fracture forces F_2^{fr} are 4.91 kN and 5.01 kN for the TC-cyc-TCT and TC-cyc-TCTCT experiments, respectively. Furthermore, fracture occurred at $\Delta u_{2,\mathrm{ref}} = 2.22\,\mathrm{mm}$ for the TC-cyc-CT test, with the fracture force F_2^{fr} reaching 5.01 kN. In the

case of the TC-cyc-CTCT experiment, the relative reverse fracture displacement is $\Delta u_{2,\text{rel}}^* = 1.80\,\text{mm}$, and the corresponding fracture force F_2^{fr} reaches $5.04\,\text{kN}$.
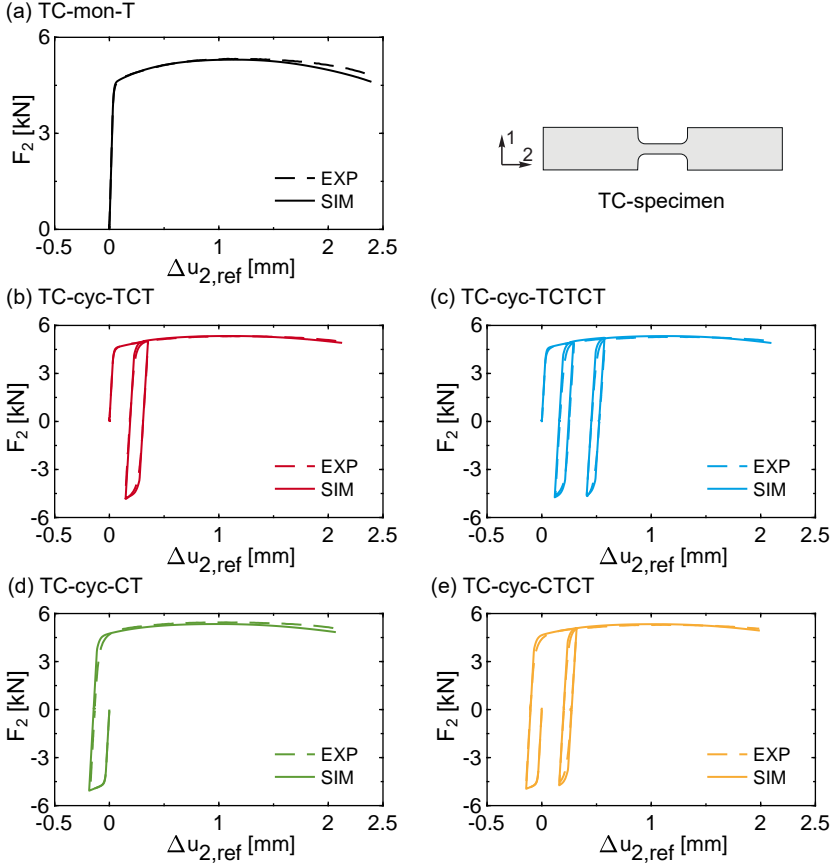

Figure 5.1: Experimental and numerical load–displacement curves for uniaxial monotonic (a) and cyclic (b)–(e) tension–compression tests.

Clearly, all uniaxial tension–compression cyclic experiments resulted in earlier failure compared to the monotonic loading. This finding indicates

that the material tends to become more brittle under cyclic loading conditions. Furthermore, the fracture forces under cyclic loading are greater than those observed under monotonic loading, attributed to strain hardening after reverse loading. In conclusion, loading histories and reverse loading conditions significantly influence the macroscopic material behavior.

5.1.2 Local strain fields

A comparison of the distribution of the first principal strains A_1 on the TC-specimen surfaces between experiments and numerical simulations is shown in Fig. 5.2. The numerically predicted A_1 shows good agreement with the experimental ones. Moreover, the necking effect can be observed in both experiments and numerical simulations. Among them, the experimentally observed and numerically predicted maximum first principal strains are highly localized on the center of TC-specimen surfaces, with their maximum values being $A_1 = 0.36$ for the TC-mon-T experiment and $A_1 = 0.35$ for the TC-cyc-TCTCT test, as illustrated in Figs. 5.2(a) and (c). Moreover, the numerically predicted orange-red region in the TC-cyc-TCT test is slightly wider than that one in the TC-cyc-CT test, see Figs. 5.2(b) and (d). However, the values of the maximum principal strains A_1 show no apparent differences, with $A_1 = 0.28$ for the TC-cyc-TCT test and $A_1 = 0.29$ for the TC-cyc-CT experiment, respectively. Additionally, the numerically predicted $A_1 = 0.37$ for the TC-cyc-CTCT experiment is deemed acceptable, although the predicted orange-red strain region is slightly narrower and darker than the experimental one. These findings clearly indicate that the loading patterns and reverse loading conditions significantly affect the plastic behavior, resulting in differences in the localization of the total strain field A_1.

5.1.3 Damage strains, fracture surfaces, and SEM images

The fracture pictures of the TC-specimens and the distribution of the damage strains A_1^{da} on the surfaces 12 and in the cross-sections 13 of the TC-specimens are shown in Fig. 5.3, respectively. It can be observed that the damage strains A_1^{da} are mainly localized in the cross-sections of the TC-specimens, where the maximum values of A_1^{da} are significantly
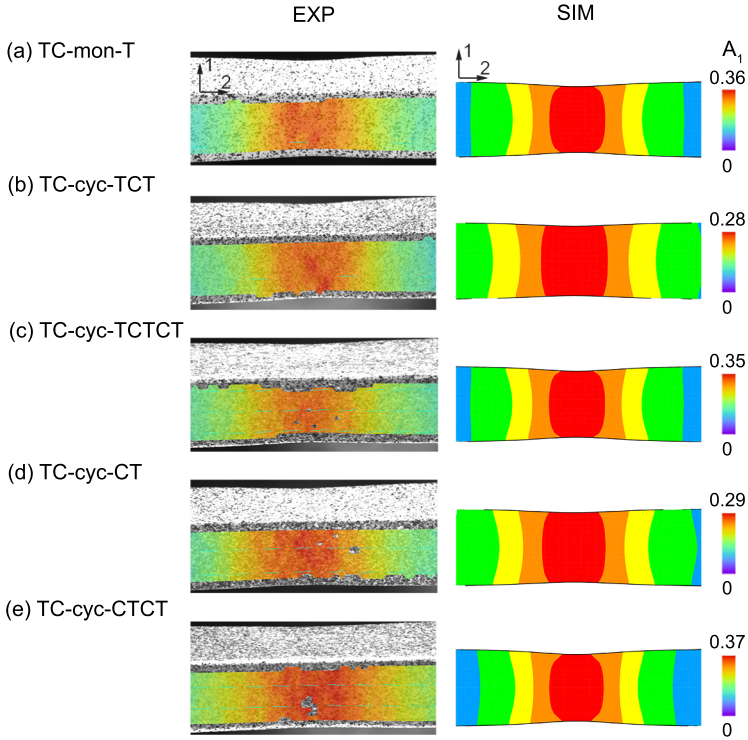
Figure 5.2: Experimental (EXP) and numerical (SIM) distribution of the first principal strains A_1 on the TC-specimen surfaces (surface 12, coordinate see Fig. 4.2).

greater in the cross-sections than that ones on the surfaces, see Fig. 5.3. This observation is supported by the experimental result of the typical tension test, where the specimen failed from the inner side towards the outside. In addition, the TC-mon-T test has the maximum predicted damage strain $A_1^{\mathrm{da}} = 7.04\%$ in the cross-section, and no damage strain is numerically predicted on the surface. Moreover, the maximum damage strain $A_1^{\mathrm{da}} = 0.37\%$ on the TC-specimen surface is observed in the TC-cyc-CTCT loading case, while $A_1^{\mathrm{da}} = 3.48\%$ is predicted in the cross-
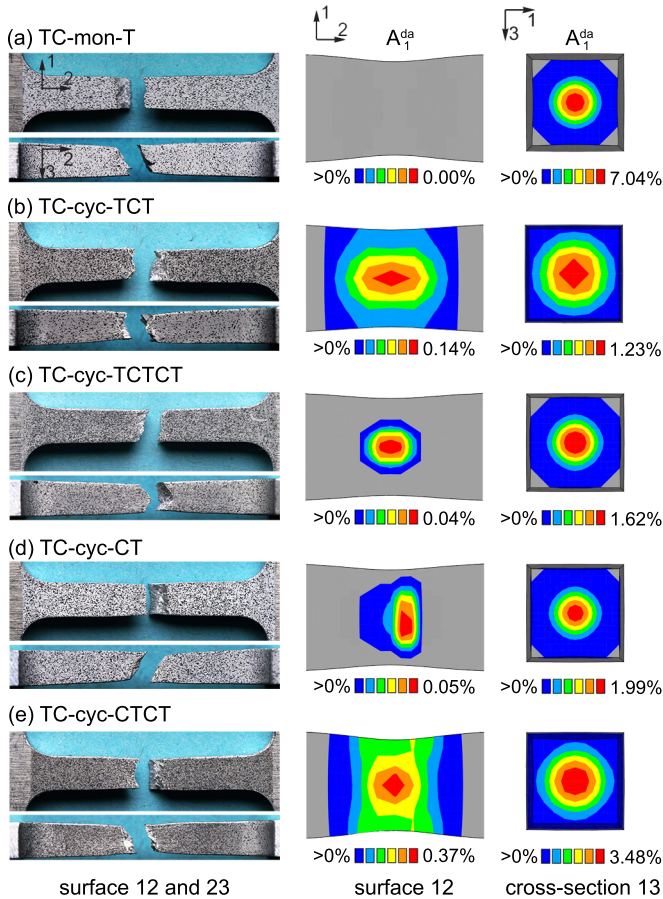
Figure 5.3: Fracture pictures for the TC-specimens (left) and numerically predicted damage strains A_1^{da} (right) on the surface 12 and in the cross-section 13 of the TC-specimens.

section. Similarly, the damage strains A_1^{da} in the TC-cyc-TCT test are distributed as widely on the surface as in the TC-cyc-CTCT experiment, but its maximum value is only 0.14%. The maximum damage strain $A_1^{\mathrm{da}} = 1.23\%$ is predicted in the cross-section. In the cases of the TC-

cyc-TCTCT and TC-cyc-CT, the maximum values of the damage strains A_1^{da} are nearly the same on the surface, around 0.05%, while in the cross-sections, they are 1.62% and 1.99%, respectively. Thus, different distributions of the numerically predicted damage strains A_1^{da} confirm that the loading patterns affect the damage behavior on the microscopic level.

Concerning the fracture pictures shown in Fig. 5.3 (left), different kinds of fracture lines are visible on the surfaces of TC-specimens. The fracture lines for the loading patterns TC-mon-T (Fig. 5.3(a)) and TC-mon-CT (Fig. 5.3(c)) appear smoother than those in the other loading cases. Moreover, the typical cup-cone fracture surfaces occur due to large plastic deformations and necking, as shown in strain fields in Fig. 5.1. Additionally, the fracture surfaces become more rough and irregular under cyclic loading conditions than that one observed under monotonic loading condition. Most interestingly, the numerically predicted A_1^{da} for loading paths TC-cyc-TCT and TC-cyc-TCTCT on the surface is distributed more widely than for the others, resulting in significantly rougher and more irregular fracture surfaces.

The stress triaxialities η are nearly the same for different loading cases, as observed in the numerical simulations of Wei et al. (2022). The stress triaxiality is -1/3 under compressive loading, and 1/3 is obtained in the tensile loading before necking occurs. After that, the stress triaxialities increase during the loading, up to 0.6 in the center of cross-section 13 (see Fig. 4.2). Furthermore, the SEM images taken from the fracture cross-sections are illustrated in Fig. 5.4. The micro-voids are visible for all loading patterns, caused by high stress triaxialities ($\eta > 1/3$). Larger micro-defects and dimples are observed under cyclic loading compared to those under monotonic loading condition. For example, a comparison of Figs. 5.4(a)-(c) reveals that the micro-defects become denser and larger, caused by the coalescence of the micro-voids when subjected to more tensile–compressive cyclic loading patterns. One possible explanation could be that compressive loading changes the size and shape of the micro-defects, causing them to become flatter (penny-shaped). These flatter micro-voids may be more susceptible to coalescing with neighboring ones, as explained by Kanvinde and Deierlein (2007). In addition, the depth of the dimples observed in Fig. 5.4(c) is shallower than of those shown in Fig. 5.4(a), indicating a more brittle material be-

(a) TC-mon-T

fracture surfce for SEM image

(b) TC-cyc-TCT

(c) TC-cyc-TCTCT

(d) TC-cyc-CT
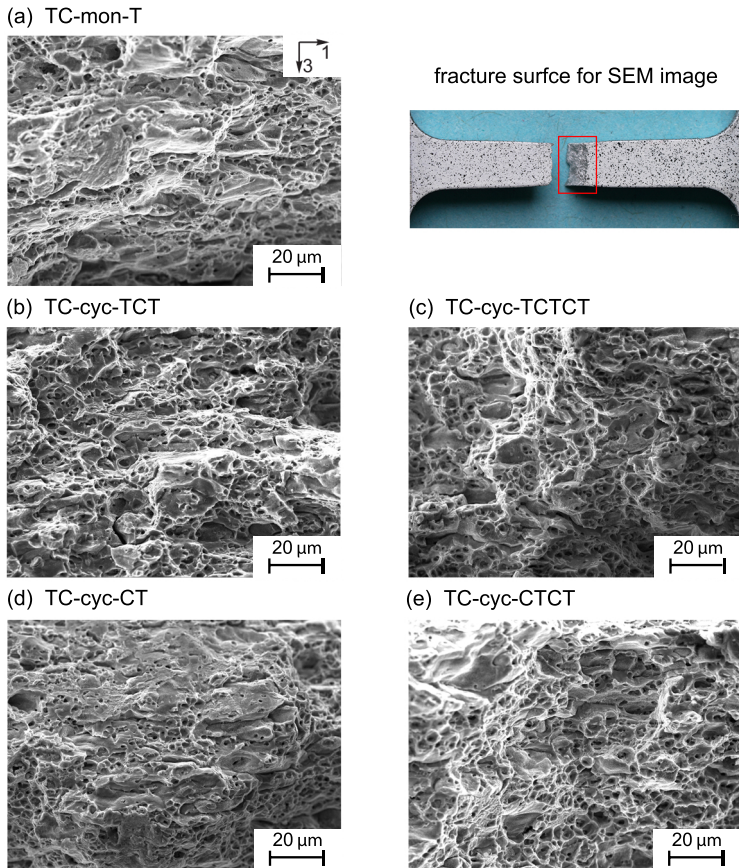
(e) TC-cyc-CTCT

Figure 5.4: SEM images taken from the fracture surfaces for the TC-specimens (Wei et al., 2022).

havior with an increasing number of cyclic loading patterns. The same trend is evident when comparing the experiments between TC-cyc-CT and TC-cyc-CTCT. These microscopic findings explain that the specimens fail earlier after reverse loading than monotonic loading. From the microscopic SEM perspective, it can be concluded that reverse loading

conditions significantly influence the damage and fracture behavior at the microscopic level.

5.1.4 Summary

The uniaxial monotonic and various cyclic experiments have been conducted to investigate plastic, damage, and fracture behavior. The identified material parameters and the proposed elastic-plastic-damage model, incorporating a combined hardening rule, demonstrated accurate predictions of load–displacement curves and local strain fields at the macroscopic level. In particular, the initial tensile and compressive yield stresses (the SD-effect), as well as the yield stresses after reverse loading (the Bauschinger-effect), can be accurately captured using the proposed material model. Plastic, damage, and fracture behavior have been found to be significantly influenced by loading patterns and reverse loading conditions. At the microscopic level, larger and coalesced micro-defects and dimples were observed after reverse loading. Furthermore, an increase in the number of loading cycles led to a more brittle behavior. One limitation of the uniaxial monotonic and cyclic experiments is that the stress triaxialities (η) are confined to a small range, e.g., $\eta = -1/3$ for compressive loading and $\eta = 1/3$ for tensile loading.

5.2 One-axial shear tests

5.2.1 Global load–displacement curves

The experimental and numerical simulation results are shown in Fig. 5.5. Moreover, for cyclic loading tests, the numerical results with the non-hardening correction (w/corr.) and without the non-hardening correction (wo/corr.) are additionally compared with the experimental ones in Figs. 5.5(b)-(e), respectively. It is evident that the numerical simulations with non-hardening correction accurately characterize the load–displacement curves after shear reverse loading for all shear cyclic loading patterns. This emphasizes the importance of considering the hardening change effect after shear reverse loading conditions, as discussed in Section 2.4.
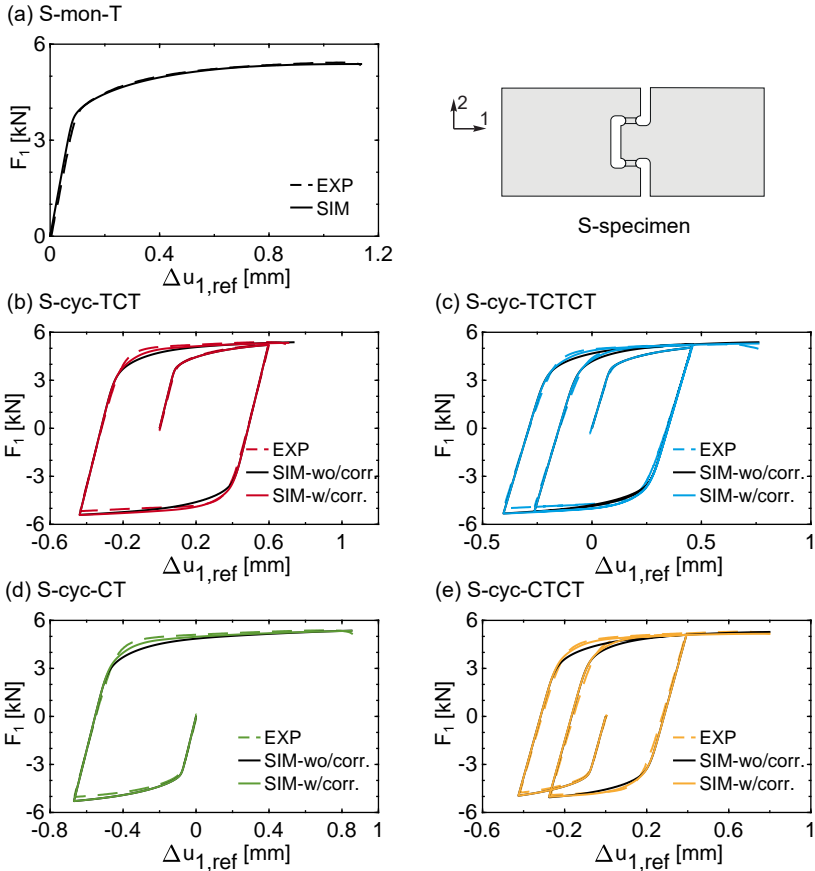
Figure 5.5: Experimental and numerical load–displacement curves for one-axial monotonic (a) and cyclic (b)–(c) shear tests.

In addition, the experimentally observed maximum forces F_1^{max}, fracture forces F_1^{fr} and corresponding fracture displacements $\Delta u_{1,\mathrm{rel}}^*$ and $\Delta u_{1,\mathrm{ref}}^{\mathrm{fr}}$ are listed in Table 5.1. Among them, the relative reverse fracture displacement $\Delta u_{1,\mathrm{rel}}^*$ is defined as the displacement in axis 1 from zero force to the final failure for the last loading pattern. As can be observed in Table 5.1 and Fig. 5.5, the shear monotonic test (S-mon-T) failed with

a maximum force $F_1^{\mathrm{max}} = 5.42\,\mathrm{kN}$, which is evidently larger than that ones observed under cyclic experiments. Regarding the relative fracture displacement $\Delta u_{1,\mathrm{rel}}^*$, it decreases with an increasing number of loading cycles for the cyclic tests, as shown in Table 5.1. Moreover, the specimens also failed earlier under cyclic loading tests than that ones undergoing monotonic loading test, excluding cyclic test S-cyc-CT. These findings clearly confirm that the monotonic and cyclic loading patterns, as well as the number of loading cycles, significantly influence the material responses in terms of macroscopic fracture forces and displacements.

Table 5.1: Maximum forces F_1^{max}, fracture forces F_1^{fr}, and fracture displacements $\Delta u_{1,\mathrm{rel}}^*$ and $\Delta u_{1,\mathrm{ref}}^{\mathrm{fr}}$.

Tests	FP			
	F_1^{max} [kN]	F_1^{fr} [kN]	$\Delta u_{1,\mathrm{ref}}^{\mathrm{fr}}$ [mm]	$\Delta u_{1,\mathrm{rel}}^*$ [mm]
S-cyc-T	5.42	5.34	1.16	1.16
S-cyc-TCT	5.39	5.13	0.72	1.03
S-cyc-TCTCT	5.25	4.97	0.77	0.91
S-cyc-CT	5.38	5.14	0.86	1.41
S-cyc-CTCT	5.30	5.11	0.83	0.98

5.2.2 Local strain fields

A comparison between the experimental distribution of the first principal strains A_1 obtained from the DIC and numerically predicted ones is illustrated in Fig. 5.6. It is evident that the numerically predicted shear bands show good agreement with the numerical results in terms of shape and corresponding maximum values. In addition, the first principal strains A_1 are more discontinuously distributed along the shear bands in the tests S-cyc-CT and S-cyc-CTCT compared to those in the S-mon-T, S-cyc-TCT, and S-cyc-TCTCT experiments. Moreover, monotonic loading results in the maximum first principal strain $A_1 = 0.63$ among all the loading patterns, as its loading direction does not change during the loading process. As observed during the experiments and simulations, strains change their directions and values due to the alteration of loading direction in cyclic loading tests. These facts indicate that the loading histories alter the distributions and maximum values of the first principal strains.
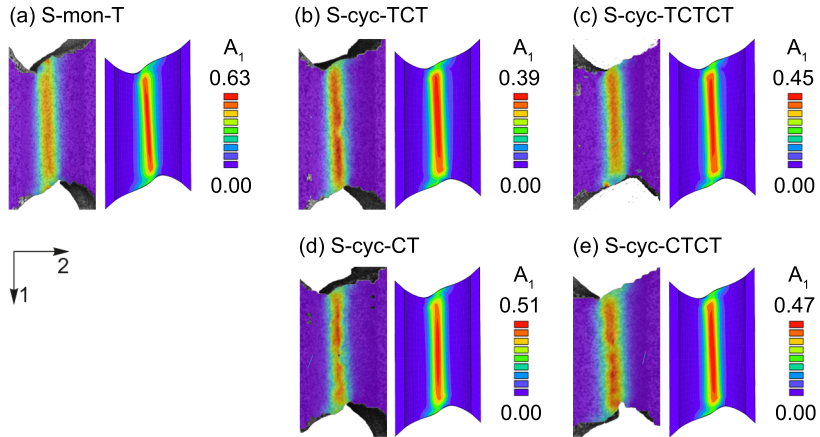
Figure 5.6: Experimental (left) and numerical (right) distribution of the first principal strains A_1 on the shear specimen surface (surface 12, coordinate see Fig. 4.2).

5.2.3 Stress triaxiality, stress Lode parameter and strain Lode parameter

The mean stress triaxiality $\bar{\eta}$ and the mean stress Lode parameter $\bar{\omega}$ are discussed in detail to study the dependency of the stress states on the damage and fracture behavior. As shown in Fig. 5.7(a), the mean stress triaxiality $\bar{\eta}$ increases from about 0.1 to 0.2 for the monotonic loading test S-mon-T. In the cyclic loading test, $\bar{\eta}$ and $\bar{\omega}$ show a significant increase at the beginning of the alternation of the loading direction, followed by a subsequent decrease. For cyclic experiments, the positive mean stress triaxialities $\bar{\eta}$ are generated undergoing the shear loads in the tensile loading direction, and the negative mean stress triaxialities are obtained for the shear loads in the compressive loading direction. In addition, the $\bar{\eta}$ at the end of the loading patterns TCT, TCTCT, CT, and CTCT are 0.14, 0.17, 0.16, and 0.2, respectively. Moreover, the evolution of the mean stress triaxialities $\bar{\eta}$ and the mean stress Lode parameters $\bar{\omega}$ are nearly similar for the same loading directions within various loading patterns. For example, changes in $\bar{\eta}$ (Fig. 5.7) and $\bar{\omega}$ (Fig. 5.8) in the S-
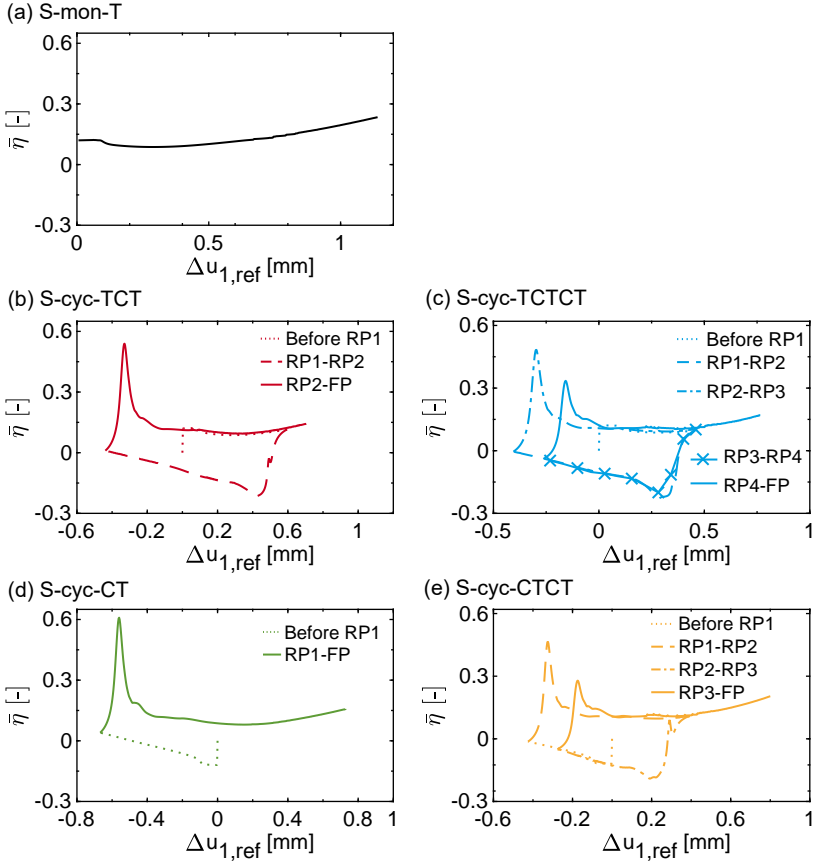
Figure 5.7: The mean stress triaxiality ($\bar{\eta}$) versus displacements $\Delta u_{1,\mathrm{ref}}$ during the loading processes.

cyc-TCTCT experiment are represented by blue dashed line (RP1-RP2, C to T) and solid line with x-marker (RP3-RP4, C to T), respectively, which show nearly consistent behavior. The same trends can be observed in Figs. 5.7 and 5.8. It is evident that only the mean stress triaxiality and the mean stress Lode parameter are challenged to distinguish between different cyclic loading patterns.

Thus, Wei et al. (2023b) proposed a novel strain Lode parameter $\bar{\omega}_\mathrm{A}$ to address the problem mentioned above. As can be observed in Fig. 5.8 (right), the mean strain Lode parameter changes significantly during the loading processes. For example, the mean stress Lode parameters $\bar{\omega}$ at RP1 and FP for the test S-cyc-TCT are both approximately 0.14, whereas the mean strain Lode parameters are 0.14 and 0.19, respectively. This distinction highlights the changes in loading patterns during the loading processes. Similar trends can also be observed in the other loading cases. Most importantly, there is no apparent difference between the $\bar{\omega}$ and $\bar{\omega}_\mathrm{A}$ for the monotonic loading S-mon-T, as shown in Fig. 5.8.

5.2.4 Damage strains, SEM images and damage mechanisms

The distribution of the first principal damage strains A_1^da on the surfaces and notched cross-sections are shown in Fig. 5.9. One can also see the fracture lines marked with red lines on the notch surfaces in Fig. 5.9. Different distribution of the damage strains A_1^da can be observed for various loading patterns. For example, the numerically predicted damage strains A_1^da are distributed along the shear band on the notch surface and localized at the edge of the notched cross-section for the monotonic loading S-mon-T, see Fig. 5.9(a). For cyclic loading patterns S-cyc-TCT and S-cyc-TCTCT, the damage strains A_1^da are localized on the bottom and the middle of the notch surfaces with maximum values of 2.28% and 1.72%, respectively. Moreover, the numerically predicted damage strains A_1^da are more uniform on the notched cross-sections compared to the ones observed in the monotonic loading case, leading to a more brittle behavior of the material, as shown in Figs. 5.9(a)–(c). Furthermore, the maximum damage strains A_1^da occur on the top of the notch surfaces for the S-cyc-CT and S-cyc-CTCT experiments, as observed in Figs. 5.9(d) and (e). In the case of the S-cyc-CT experiment, the damage strains A_1^da are mainly distributed at the edge of the notched surface (Fig. 5.9(d)), whereas the damage strains A_1^da appear and cover the middle to the bottom of the notched surface (Fig. 5.9(e)) in the S-cyc-CTCT test.

Furthermore, the evolution of the damage strain increments ΔA_1^da for the loading patterns S-cyc-TCT and S-cyc-CTCT are additionally illustrated in Fig. 5.10. The damage strains A_1^da occur and develop mainly on the notch surface and at the edge of the notched cross-section until
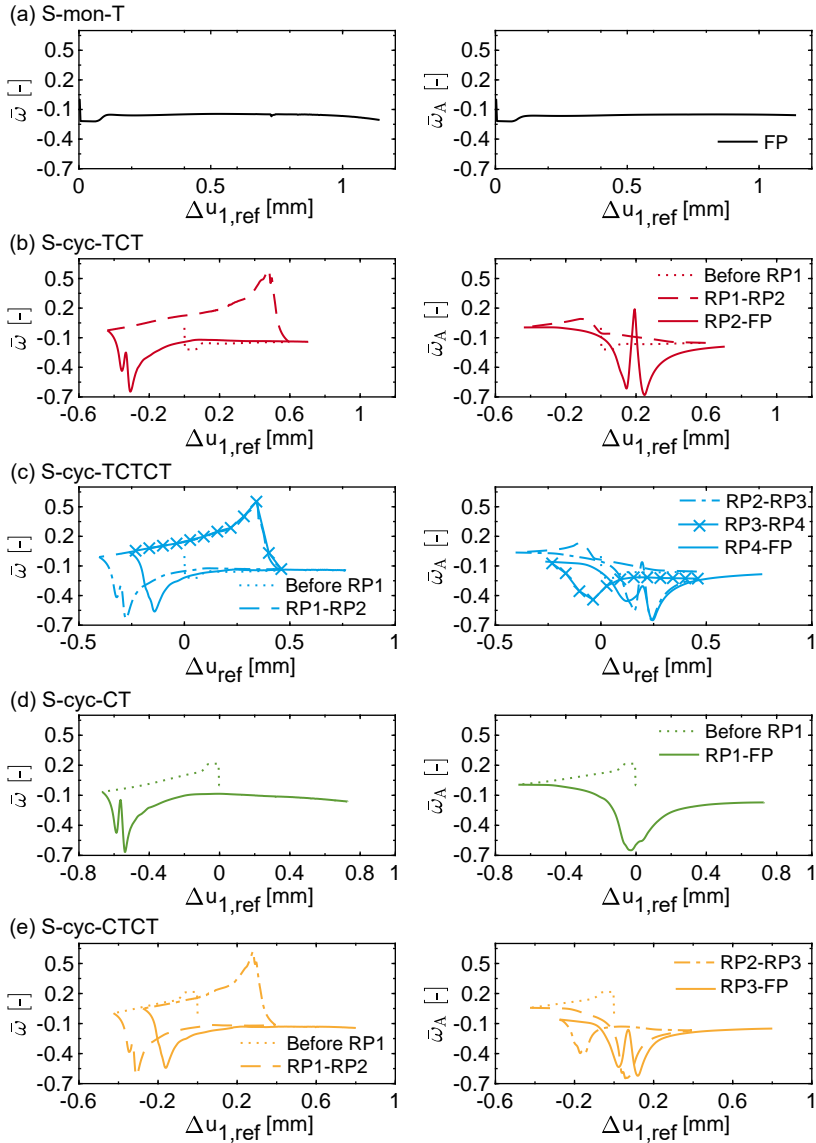
Figure 5.8: The mean stress Lode parameter $\bar{\omega}$ versus displacements $\Delta u_{1,\text{ref}}$ (left) and the mean strain Lode parameter $\bar{\omega}_{\text{A}}$ versus displacements $\Delta u_{1,\text{ref}}$ (right) during the loading processes.
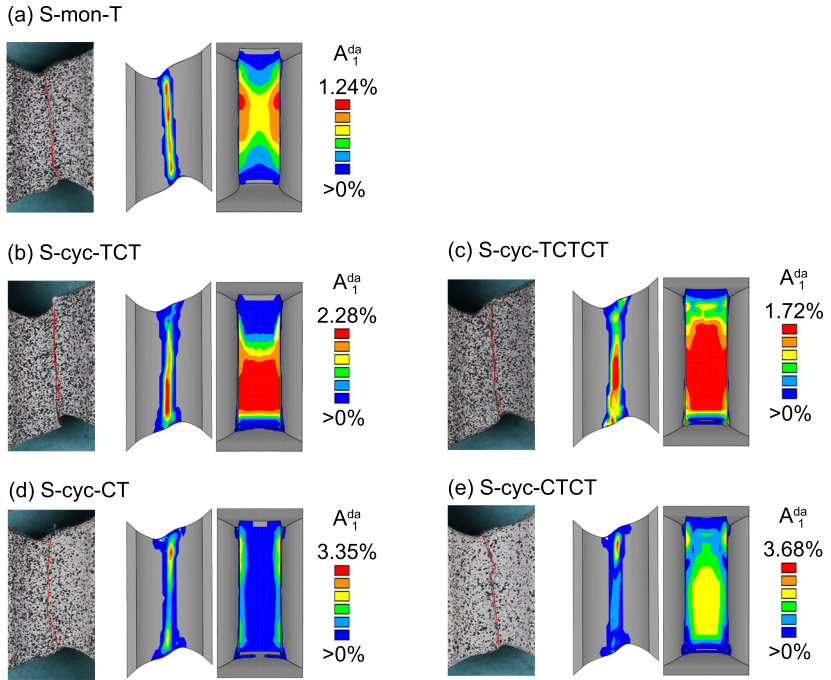
Figure 5.9: Fracture pictures for the shear specimens (left) and numerically predicted damage strains A_1^{da} on the surface 12 and in the cross-section 13 of the shear specimens.

reverse point 1 (RP1). During subsequent reverse loading, the damage strains increase significantly in the middle-bottom of the notched cross-section. Interestingly, the damage strains ΔA_1^{da} decrease mainly over the notch surface and notched cross-section from RP2 to FP, i.e., from shear in the compressive loading direction to the tensile loading direction. However, damage only increases on the top of the notch surface and in the middle-bottom of the notched cross-section, as shown in Fig. 5.10(a). In the first shear load in the compressive loading direction (C) of the S-cyc-CTCT, nearly no damage is numerically predicted in the notched surface and cross-section. From RP1 to RP2 and RP2 to RP3, the damage strains mainly appear and develop on the notch surface
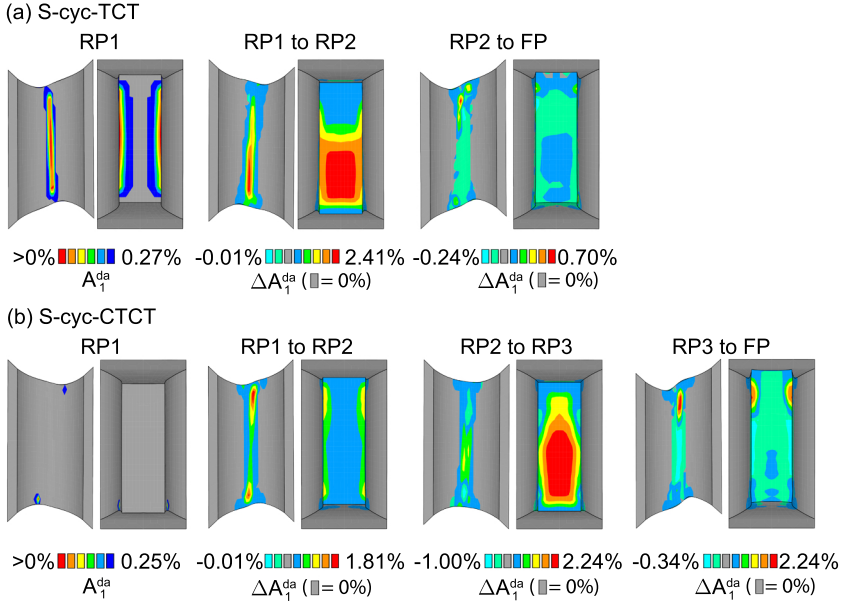
**Figure 5.10:** The changes in the first principal damage strain ΔA_1^{da} for the experiments S-cyc-TCT and S-cyc-CTCT at various reverse points (RPs) and fracture point (FP).

and the notched cross-section. Again, the damage strains reduce nearly everywhere and increase only on the top of the notch surface for the last tensile loading pattern (RP3 to FP). These findings confirm that loading patterns, reverse loading condition, and the number of loading cycles influence the occurrence and development of the damage strain.

The SEM images taken from the fracture surfaces for the shear specimens are shown in Fig. 5.11. Micro-shear-cracks are visible and dominated under monotonic and cyclic loading conditions. Moreover, as illustrated in Fig. 5.11, the micro-voids can also be observed in various loading patterns. As numerically predicted, the stress triaxialities for the monotonic and cyclic loading tests are generated appropriately from -0.2 to 0.2, see Fig. 5.7. Based on the proposed damage mechanism, damage is caused by the micro-defects under the low positive stress triaxialities $0 \leq \eta \leq 1/3$.

The SEM images provide clear evidence supporting the critical aspects of the proposed damage theory. In addition, larger and denser micro-voids and coalesced micro-shear-cracks can be seen in the cyclic loading patterns TCT, TCTCT, CT, and CTCT than the ones under monotonic loading (T). Moreover, the same trends can be observed by increasing the number of loading cycles, as seen in the comparison between

(a) S-mon-T

(b) S-cyc-TCT

(c) S-cyc-TCTCT

(d) S-cyc-CT

(e) S-cyc-CTCT
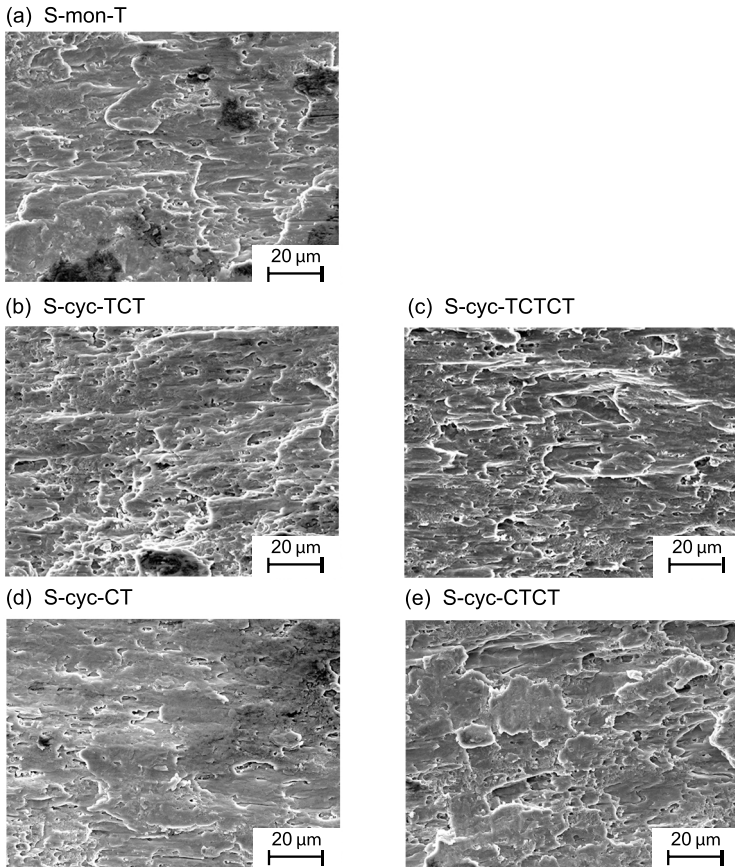
Figure 5.11: SEM images taken from the fracture surfaces for the shear specimens (Wei et al., 2022).

TCT and TCTCT. It indicates that micro-defects become more accessible to coalescence with neighboring ones, leading to further degradation of the material at the microscopic level after reverse loading. Also, the micro-defects are more uniformly distributed in the notch cross-section as observed in Figs. 5.11(b) and (c), which agree well with the numerical predictions of the damage strains in Figs. 5.9(b) and (c). It reveals that the proposed anisotropic continuum damage model demonstrates good predictive accuracy for the mechanical response at the microscopic level. Most importantly, the SEM images clearly show the influence of the reverse loading condition on the microscopic damage behavior.

5.2.5 Summary

Monotonic and cyclic one-axis shear tests were conducted to investigate the damage and fracture behavior under shear-dominated stress states. The designed one-axis-loaded shear specimens successfully generated low negative and positive stress triaxialities. As shown in the SEM pictures, damage is caused by the growth and coalescence of the micro-defects, with micro-shear-cracks dominating. More larger and denser micro-voids and coalesced micro-shear-cracks can be seen in the cyclic loading patterns than under monotonic loading. Furthermore, the change in the hardening ratio is obviously observed in the experiments. The novel straightforward hardening correction method effectively improves the numerical results. In addition, the stress triaxiality and the stress Lode parameter can not distinguish the different cyclic loading patterns within each loading case. However, the newly proposed strain Lode parameter addresses this issue. The experimental and numerical results regarding global load–displacement curves and local strain fields, the occurrence and evolution of the damage strains, as well as SEM images of the fracture surfaces, provide clear evidence of how the reverse loading condition and loading histories change the material behavior at macroscopic and microscopic levels. Although the newly designed one-axis-loaded shear specimen allows for broadening the range of stress triaxialities compared to the TC-specimen, it still covers a small range of stress triaxialities. Hence, biaxial non-proportional experiments are conducted to induce a broader range of stress states.

5.3 Single cyclic biaxial tests

5.3.1 Shear reverse experiments superimposed by tensile or compressive preloads

Fracture displacements, forces, and global load–displacement curves

The overview of the experimental load–displacement curves for monotonic loading is shown in Fig. 5.12. Moreover, the experimental mono-
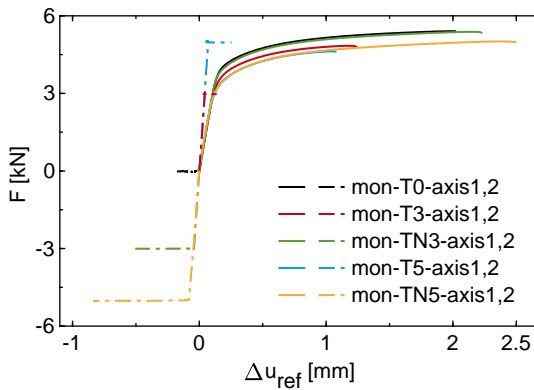

Figure 5.12: Overview of the experimental load–displacement curves for monotonic loading.

tonic and cyclic load–displacement curves are illustrated in Figs. 5.13(a1)-(e1), and Figs. 5.13(a2)-(e2) provide a comparison between the monotonic and first and second reversal load–displacement curves. Note that the load–displacement curves after reverse loading are aligned with the related monotonic experiments to compare the hardening rate change quickly. It can be observed that the yield stresses and the hardening rate are significantly altered after shear reverse loading conditions, as shown in Figs. 5.13(a2)-(e2). A similar phenomenon was detected by Daroju et al. (2022) in aluminum alloy AA6016-T4. In Fig. 5.13(a2), reversal yield stresses for experiments with 0 kN preload are nearly identical to the initial yield stress under monotonic loading, with only a slight change in the hardening rate. In contrast, the hardening rate significantly in-

creases after reverse loading for tests with negative preloads of $-3\,\text{kN}$ and $-5\,\text{kN}$, see Figs. 5.13(c2) and (e2). Comparing the second reversal load–displacement curves to the monotonic loading for tests with positive preload, a similar, although more minor, increase in the hardening rate is observed in Figs. 5.13(b2) and (d2).

Table 5.2: Fracture forces F_1^{fr} and fracture displacements $\Delta u_{1,\text{rel}}^*$, $\Delta u_{1,\text{ref}}^{\text{fr}}$, and $\Delta u_{2,\text{ref}}^{\text{sw}}$ (Wei et al., 2023b).

Tests HC-	preload F_2 [kN]	monotonic (mon-)			cyclic loading (cyc-)			
		$\Delta u_{1,\text{ref}}^{\text{fr}}$ [mm]	$\Delta u_{2,\text{ref}}^{\text{sw}}$ [mm]	F_1^{fr} [kN]	$\Delta u_{1,\text{ref}}^{\text{fr}}$ [mm]	$\Delta u_{1,\text{rel}}^*$ [mm]	$\Delta u_{2,\text{ref}}^{\text{sw}}$ [mm]	F_1^{fr} [kN]
T0	0	2.02	n/a	5.40	1.20	1.31	n/a	5.01
T3	3	1.24	0.09	4.78	0.59	0.58	0.14	4.57
TN3	-3	2.41	-0.46	5.36	2.27	2.23	-0.63	5.62
T5	5	1.08	0.19	4.61	0.44	0.48	0.26	4.23
TN5	-5	2.50	-0.75	4.97	2.01	1.99	-0.97	5.65

In addition, a comparison of the fracture displacement $\Delta u_{1,\text{ref}}^{\text{fr}}$ in axis 1, the relative displacement after the change of the loading axis $\Delta u_{2,\text{ref}}^{\text{sw}}$ in axis 2, the relative reverse fracture displacement for axis 1 $\Delta u_{1,\text{rel}}^*$, and the fracture force F_1^{fr} in axis 1 between different monotonic and cyclic loading tests is shown in Table 5.2. It can be observed that the material exhibits increased brittleness in tests with superimposed positive preloads ($3\,\text{kN}$ and $5\,\text{kN}$) compared to the experiment without preload ($0\,\text{kN}$). The fracture forces F_1^{fr} and the fracture displacements $\Delta u_{1,\text{ref}}^{\text{fr}}$ for the HC-mon-T3 and HC-mon-T5 tests differ by approximately 15% and 40%, respectively, compared to the HC-mon-T0 test.

Furthermore, the fracture displacement $\Delta u_{1,\text{ref}}^{\text{fr}}$ decreases with increasing positive preloads. Conversely, the negative preloads ($-3\,\text{kN}$ and $-5\,\text{kN}$) increase the ductility of the investigated material, resulting in fracture displacement $\Delta u_{1,\text{ref}}^{\text{fr}}$ approximately 20% larger than that one observed in the HC-mon-T0 test. Also, the ductility increases with increasing negative preloads. These findings highlight that the loading directions and degrees of preloads play a crucial role in altering material properties.

In the case of cyclic loading, the HC-specimens exhibit earlier failure compared to those under monotonic loading, as the relative reverse frac-
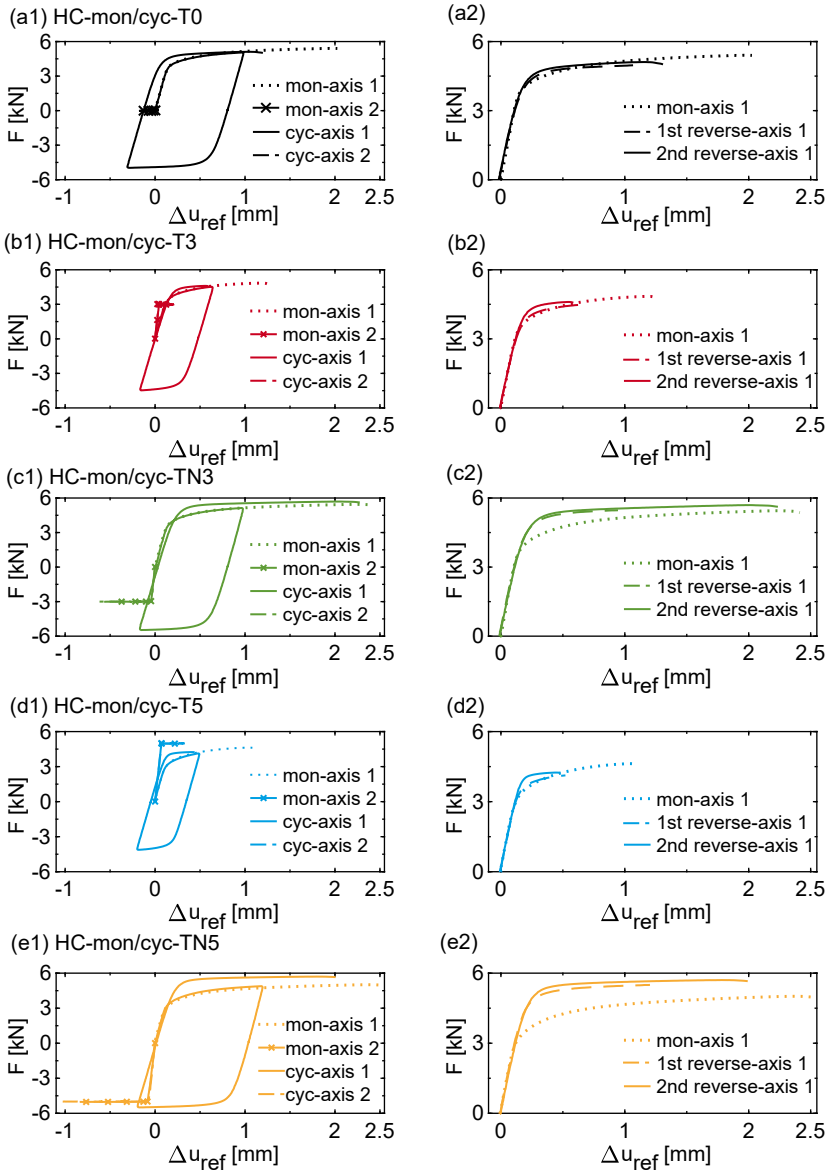
Figure 5.13: Monotonic and cyclic load–displacement curves, with a comparison of monotonic loading and 1st and 2nd reverse loading (Wei et al., 2023b).

ture displacements $\Delta u_{1,\text{rel}}^{*}$ for cyclic loading are significantly smaller than the corresponding fracture displacements $\Delta u_{1,\text{ref}}^{\text{fr}}$ observed during monotonic loading. In addition, the $\Delta u_{1,\text{ref}}^{\text{fr}}$ for cyclic loading with preloads of $3\,\text{kN}$ and $5\,\text{kN}$ differs by approximately 50% compared to the monotonic loadings. In contrast, the difference in $\Delta u_{1,\text{ref}}^{\text{fr}}$ between monotonic and cyclic loading for experiments superimposed with negative preloads ($-3\,\text{kN}$ and $-5\,\text{kN}$) is only 20%.

Furthermore, cyclic softening is observed in the cyclic experiments with preloads of $0\,\text{kN}$, $3\,\text{kN}$, and $5\,\text{kN}$, where the fracture forces F_1^{fr} differ from 4.3% to 8% between monotonic and cyclic loading conditions, as shown in Table 5.2. However, the fracture forces F_1^{fr} for the experiments with $-3\,\text{kN}$ and $-5\,\text{kN}$ preloads significantly increase after reverse loading compared to the corresponding monotonic loading conditions due to the increased hardening rate, as discussed in Figs. 5.13(c2) and (e2). It can be stated that the cyclic hardening or softening, as well as fracture behavior, are significantly influenced by the preloads.

The experimental and numerical load–displacement curves for monotonic loading are shown in Fig. 5.14. The numerical results agree well with the experimental ones in both axes. In addition, a comparison between numerical simulations with and without ($k_h = 1$ in Eq. (2.54)) considering the change hardening effect and experimental results are shown in Figs. 5.15(a1)-(e1) and (a2)-(e2), respectively. It is evident that the numerical results taken into hardening correction (see Eq. (2.54) in Section 2.4) can capture the load–displacement curves more accurately, as observed in the one-axial shear tests. This emphasizes again the importance of considering the hardening change effect after shear reverse loading conditions, as discussed in Section 2.4.

To conclude, single cyclic shear reverse experimental results reveal a significant change in the hardening rate after reverse loading. This phenomenon is also observed in the one-axial cyclic shear tests, as discussed in Section 5.2. Considering the hardening correction after reverse loading, the modified two-surface cyclic elastic-plastic-damage model can accurately predict the material behavior at the macroscopic load–displacement level. In addition, monotonic loading with tensile preload increases material brittleness, whereas negative preload enhances material ductility. Furthermore, the material exhibits increased brittleness under cyclic loading compared to monotonic loading. Cyclic softening is
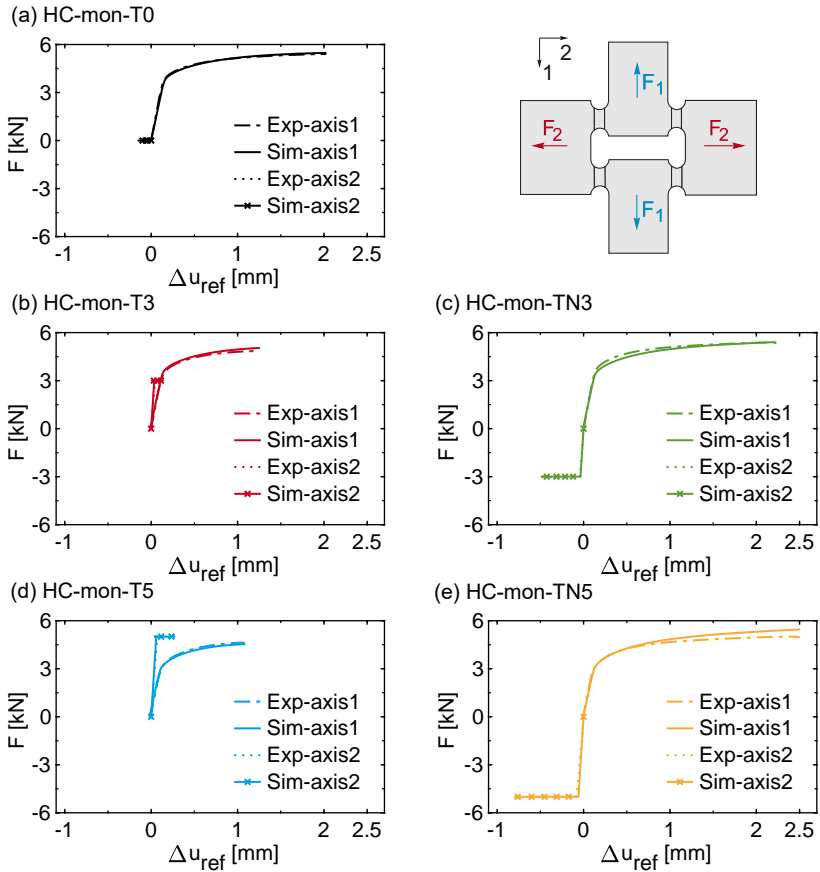
Figure 5.14: Numerical and experimental load–displacement curves for monotonic loadings (Wei et al., 2023b).

observed in the experiments with tensile preloads, while cyclic hardening is significant for the tests superimposed by compressive preloads. These findings indicate that the material behavior is significantly altered by the direction and magnitude of preloading, as well as by reverse loading conditions.
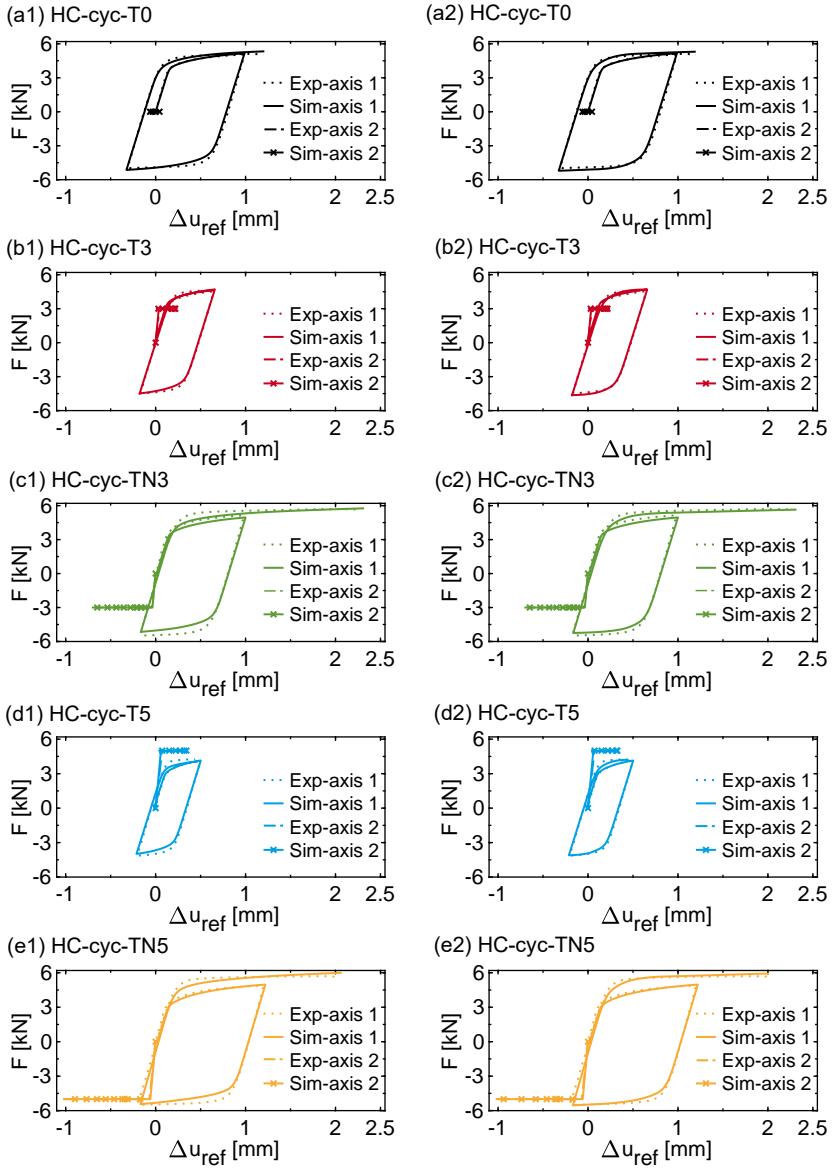
Figure 5.15: Numerical and experimental load–displacement curves without hardening correction (a1)-(e1) and with hardening correction (a2)-e(2) for cyclic loadings (Wei et al., 2023b).

Local strain fields

The experimental (obtained from DIC) and numerically predicted distribution of the first principal total strains A_1 on the notch surfaces are illustrated in Fig. 5.16. Moreover, comparisons of the experimental and numerical strain–displacement curves during the loading process are depicted in Fig. 5.17. Note that the first principal strains A_1 presented in Fig. 5.17 represent the mean value over a region of interest (ROI) of the rectangle (approximately $0.25\,\mathrm{mm} \times 0.50\,\mathrm{mm}$) on the center of the notch surface in DIC and numerical simulations. Different distributions of shear bands with varying maximum values are observed under monotonic and cyclic loading conditions with different preloads. Moreover, the numerical simulations agree well with the experimental results in both distributions and maximum values of A_1, as shown in Fig. 5.16, and in quantitative values and evolutionary trends of A_1, as presented in Fig. 5.17.

In the case of monotonic experiments, the shear bands distributed as counterclockwise with increasing tensile preloads, whereas the direction of the shears band alter along the clockwise with increase of the compressive preloads, as shown in Figs. 5.16(a1)-(e1). Moreover, the maximum values of the first principal strains A_1 for the test HC-mon-T3 and HC-mon-T5 are smaller in the experiments HC-mon-T0, HC-mon-TN3, and HC-mon-TN5, since the positive preloads increase the material brittleness and the compressive loads increase the material ductility, as discussed in Table 5.2. Additionally, the first principal strains A_1 monotonically increase during the loading process, as observed in Figs. 5.17(a)-(e).

For cyclic loading experiments, it can be observed that the strain directions and their maximum values alter at different loading stages (RP1, RP2 and FP), see Figs. 5.16(a2)-(e2). Furthermore, the distribution of A_1 at the fracture point (FP) under cyclic loading shows more a pronounced discontinuity along the shear band compared to the corresponding monotonic loading path. For example, the first principal strains A_1 for the HC-cyc-TN3 and HC-cyc-T5 experiments at RP1 continuously distribute along the shear bands with maximum values of 0.17 and 0.26, respectively. After subsequent reverse loading, the strains A_1 distribute in an X-shape, localizing in the right-top and left-bottom of the notch

(a1) HC-mon-T0 FP   (a2) HC-cyc-T0 RP1   RP2   FP

0.00 ▮▮▮▮▮▮▮ 0.61   0.00 ▮▮▮▮▮▮▮ 0.22   0.00 ▮▮▮▮▮▮▮ 0.13   0.00 ▮▮▮▮▮▮▮ 0.34

(b1) HC-mon-T3 FP   (b2) HC-cyc-T3 RP1   RP2   FP

0.00 ▮▮▮▮▮▮▮ 0.33   0.00 ▮▮▮▮▮▮▮ 0.17   0.00 ▮▮▮▮▮▮▮ 0.12   0.00 ▮▮▮▮▮▮▮ 0.25

(c1) HC-mon-TN3 FP   (c2) HC-cyc-TN3 RP1   RP2   FP

0.00 ▮▮▮▮▮▮▮ 0.57   0.00 ▮▮▮▮▮▮▮ 0.18   0.00 ▮▮▮▮▮▮▮ 0.13   0.00 ▮▮▮▮▮▮▮ 0.63

(d1) HC-mon-T5 FP   (d2) HC-cyc-T5 RP1   RP2   FP

0.00 ▮▮▮▮▮▮▮ 0.35   0.00 ▮▮▮▮▮▮▮ 0.12   0.00 ▮▮▮▮▮▮▮ 0.16   0.00 ▮▮▮▮▮▮▮ 0.21

(e1) HC-mon-TN5 FP   (e2) HC-cyc-TN5 RP1   RP2   FP

0.00 ▮▮▮▮▮▮▮ 0.64   0.00 ▮▮▮▮▮▮▮ 0.26   0.00 ▮▮▮▮▮▮▮ 0.22   0.00 ▮▮▮▮▮▮▮ 0.64
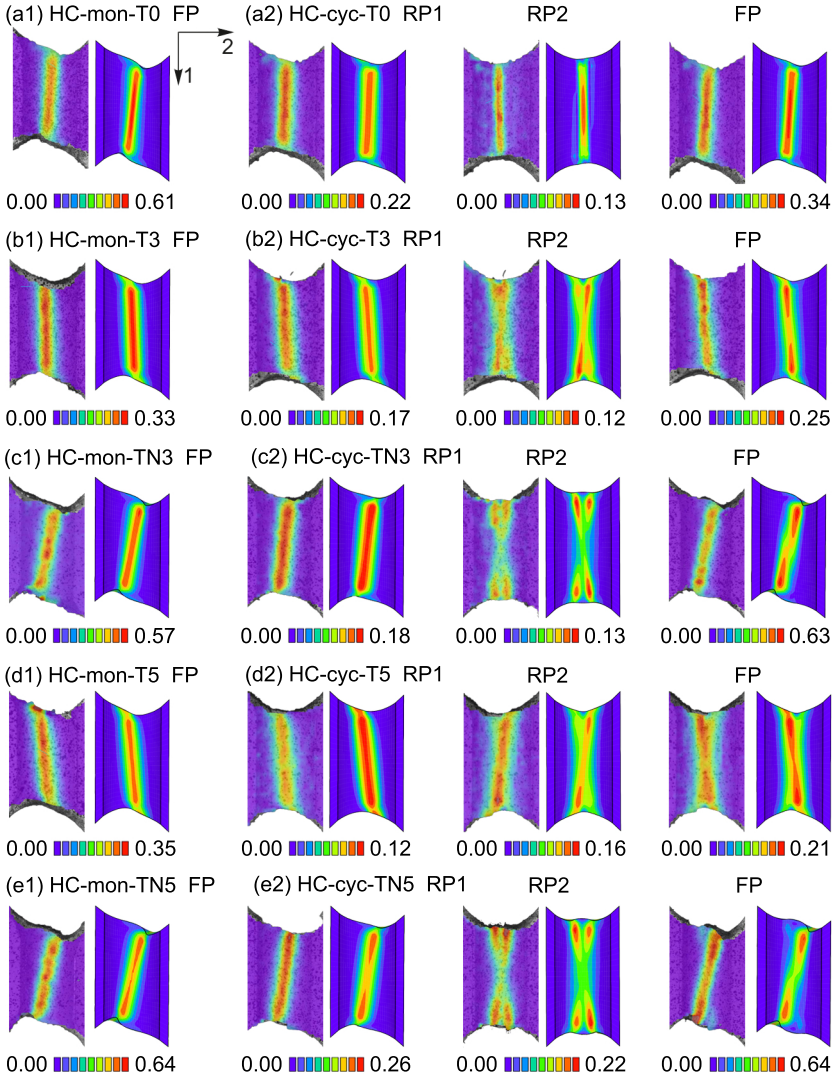
Figure 5.16: Experimental (left) and numerically predicted (right) first principal total strains A_1 on the notch surfaces (surface 12) at reverse point 1 (RP1), reverse point 2 (RP1), and fracture point (FP) (Wei et al., 2023b).
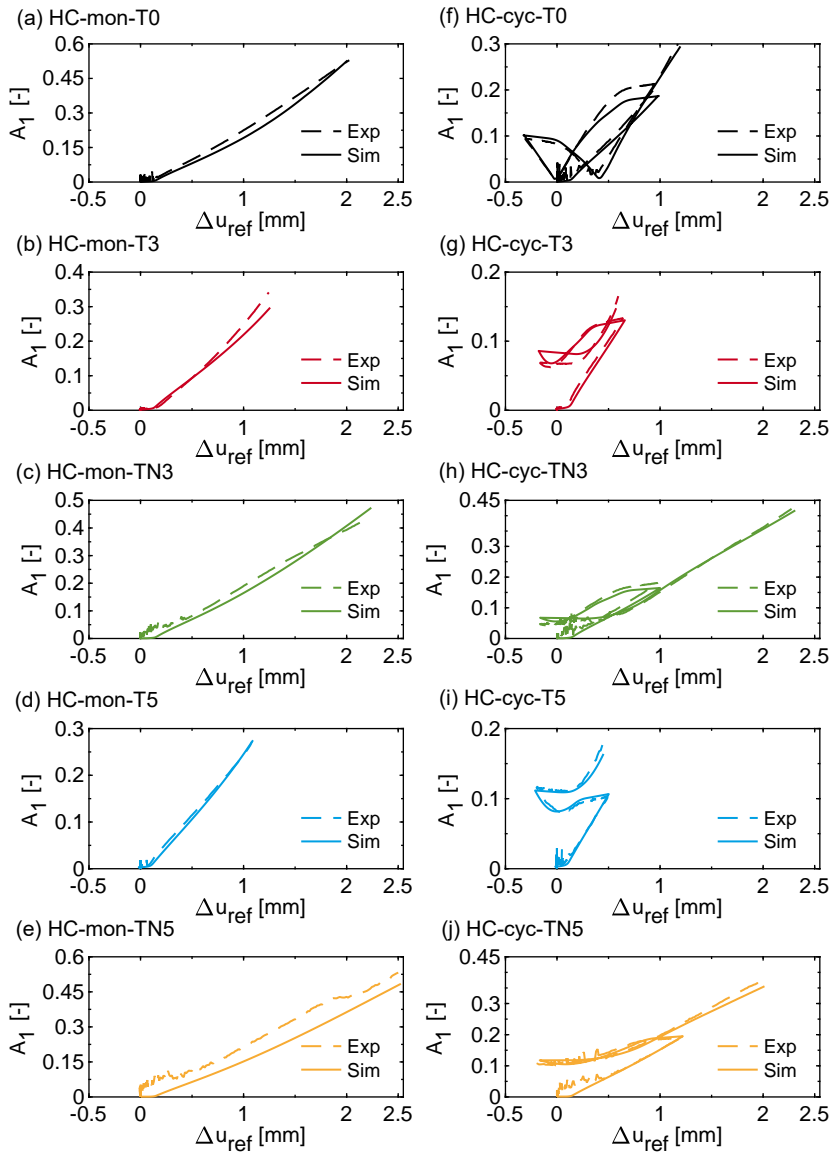
Figure 5.17: Experimental and numerically predicted first principal strains A_1 during the loading processes for monotonic tests (a)–(e) and cyclic loading tests (f)–(j) (Wei et al., 2023b).

part with decreased maximum values of 0.13 and 0.18, respectively. In the final loading pattern, the distribution of total strains along the shear band becomes discontinuous upon reversing the loading direction again. Moreover, an evident distortion is observed at the edge of the notched region due to large negative preloads superimposed during the experiments. A similar trend in strain change can be seen in the cyclic tests HC-cyc-T3 and HC-cyc-T5 (Figs. 5.16(b2) and (d2)).

Furthermore, the evolution path of the strains A_1 is strongly dependent on the loading patterns and different preloads, as illustrated in Figs. 5.17(f)-(j). Among them, the first principal strain A_1 decreases significantly at the beginning of the last loading stage, i.e., from RP1 to RP2, for the pure shear cyclic loading test (HC-cyc-T0), see Fig. 5.17(f). However, in other cyclic experiments after the second reverse loading, A_1 varied slightly at the beginning and then increased rapidly until the specimen failed. This facts reveal that the cyclic loading patterns and loading histories significantly influence the elastic-plastic behavior.

Briefly speaking, the proposed elastic-plastic-damage model can accurately characterize the distributions of first principle strains A_1 and their maximum values in different loading stages (RP1, RP2, and FP). Moreover, it successfully predicts the evolutionary trends of the first principal strains A_1 during the loading processes. Additionally, the aforementioned findings highlight the significant influence of monotonic and cyclic loading patterns, as well as different preloads, on the elastic-plastic behavior. Most importantly, reverse loading conditions can result in strain concentration and further significantly influence damage and fracture behavior.

Stress states and damage strains

As shown in Fig. 5.18(a), the mean stress triaxialities $\bar{\eta}$ for the monotonic loading tests remain nearly constant throughout the loading processes. Positive preloads (T3 and T5) and zero preload (T0) generate positive stress triaxialities, whereas negative stress triaxialities are induced by superimposing negative preloads (TN3 and TN5). Moreover, the stress triaxialities $\bar{\eta}$ increase with higher preloads; for example, $\bar{\eta}$ values for mon-T0, mon-T3, and mon-T5 are 0.08, 0.21, and 0.31, respectively. It is evident that different preloads generate different stress triaxialities.

These experiments bridge the gap between uniaxial tension-compression and one-axial shear tests.
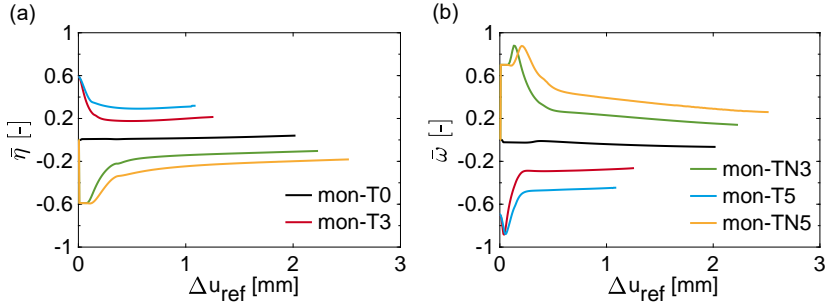

Figure 5.18: The mean stress triaxiality $\bar{\eta}$ and the mean stress Lode parameter $\bar{\omega}$ during loading processes for monotonic experiments (Wei et al., 2023b).

In addition, the evolution of the stress triaxialities $\bar{\eta}$ and of the stress Lode parameters $\bar{\omega}$ for cyclic loading paths are illustrated in Figs. 5.19(a)-(e) and Figs. 5.20(a1)-(e1), respectively. It can be observed that the values of the stress triaxialities $\bar{\eta}$ and the stress Lode parameters $\bar{\omega}$ increase quickly at the beginning of reversal loading, followed by a rapid decrease until the stress triaxialities and the stress Lode parameters stabilize again. Similar to the monotonic loading cases with various preloads, different stress triaxialities are induced under cyclic experiments. This indicates that the stress triaxiality is effective in distinguishing experiments with different preloads. However, $\bar{\eta}$ and $\bar{\omega}$ exhibit limitations in distinguishing between cases within the loading cases. For instance, at the FP for experiments superimposed by $5\,\text{kN}$ under both monotonic and cyclic loading, $\bar{\eta}$ values are 0.32 and 0.34, while $\bar{\omega}$ values are -0.44 for both cases. Similarly, the mean stress triaxialities and the stress Lode parameters at FP are nearly the same for the experiments HC-mon-TN5 and HC-cyc-TN5, i.e., $\bar{\eta} = -0.13$ and $\bar{\omega} = 0.15$. On the other hand, the mean stress Lode parameters $\bar{\omega}$ at RP1, RP2 and FP for the HC-cyc-T3 are -0.29, -0.21, and -0.20, respectively, as depicted in Fig. 5.19(b1). It presents challenges in distinguishing the stress state based on the stress triaxiality and the stress Lode parameter.
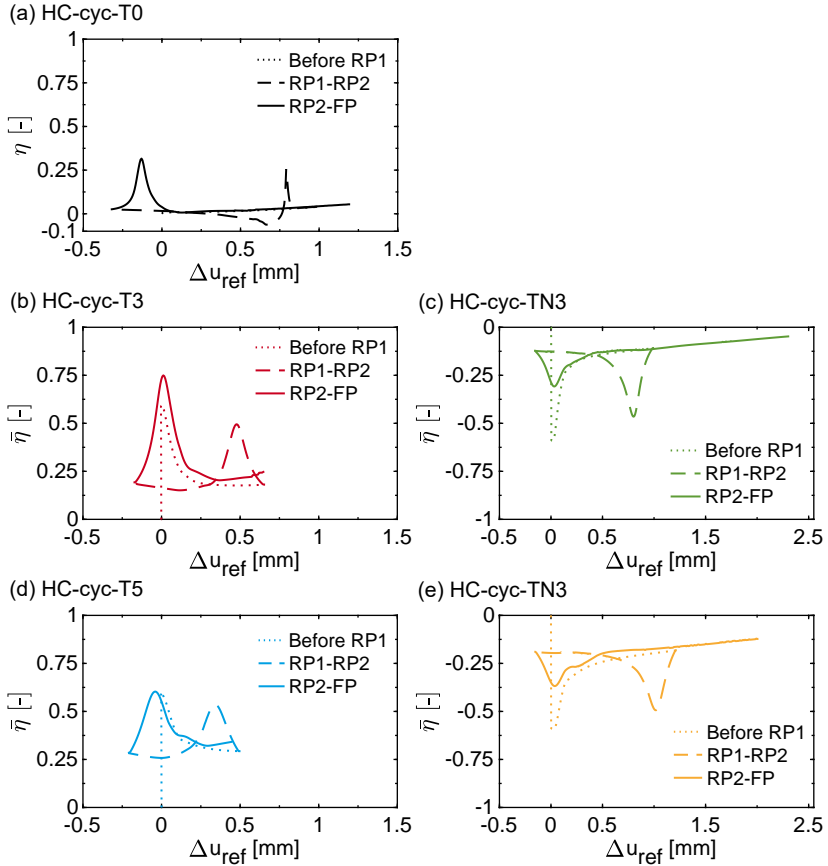
Figure 5.19: The mean stress triaxiality $\bar{\eta}$ during loading processes for cyclic experiments (Wei et al., 2023b).

As discussed in one-axial shear experiments, the strain Lode parameter $\bar{\omega}_A$ clearly enables the distinction of different loading histories. Thus, the evolution of the strain Lode parameter $\bar{\omega}_A$ under cyclic loading conditions is additionally plotted in Figs. 5.20(a2)-(e2). Apparent differences can be observed at different loading stages (RP1, RP2, and FP). As shown in Fig. 5.20(b2), the mean strain Lode parameters $\bar{\omega}_A$ at RP1, RP2 and
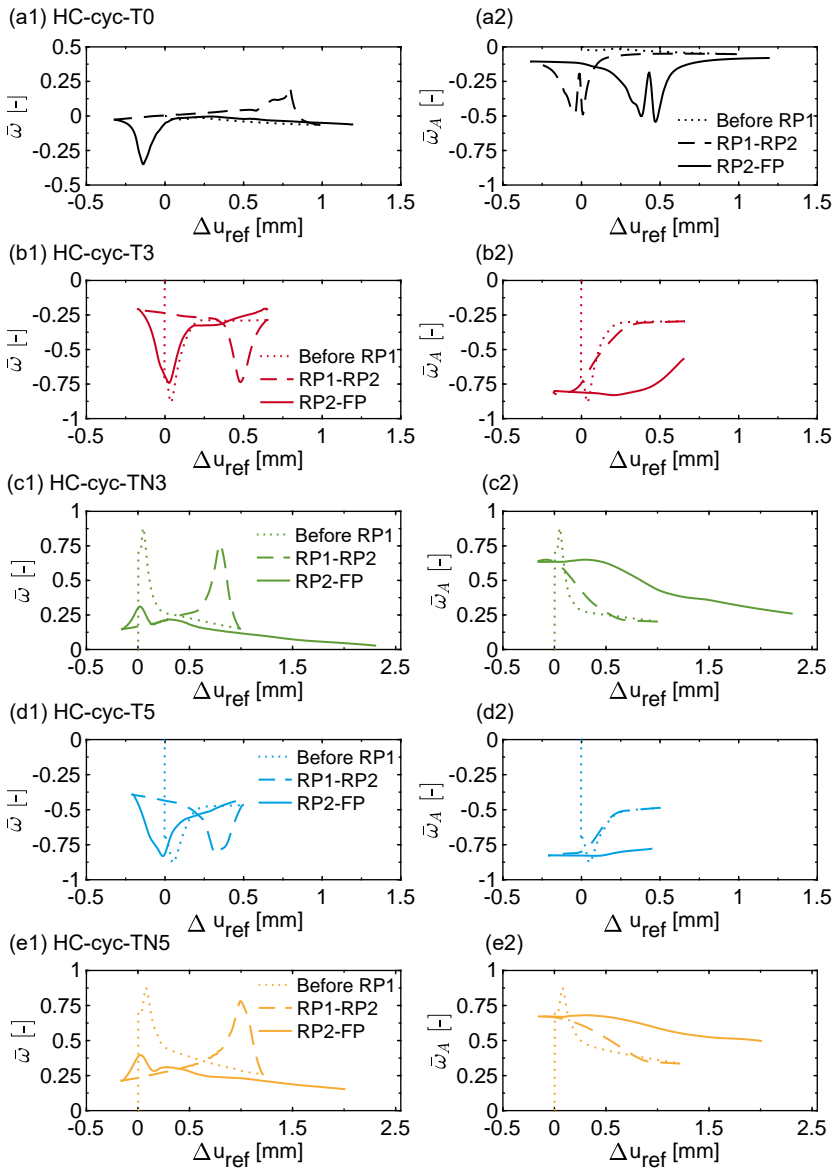
Figure 5.20: The mean stress Lode parameter $\bar{\omega}$ and the mean strain Lode parameter $\bar{\omega}_A$ during loading processes for cyclic experiments (Wei et al., 2023b).

FP for the HC-cyc-T3 are -0.30, -0.80, and -0.55, respectively. The same observations are evident in the other loading cases. It is obvious that the proposed strain Lode parameter can effectively recognize different loading histories in both one-axial and single biaxial cyclic shear experiments.

Damage strains, fracture surfaces and SEM images

The damage strains A_1^{da} for the monotonic loading experiments are shown in Fig. 5.21. As can be observed in Figs. 5.21(a), (b) and (d), it is evident that the shapes of the damage strain distributions A_1^{da} closely resemble those of the first principal strains A_1 shown in Figs. 5.16(a), (b) and (d), respectively. Moreover, the maximum values of the damage strains
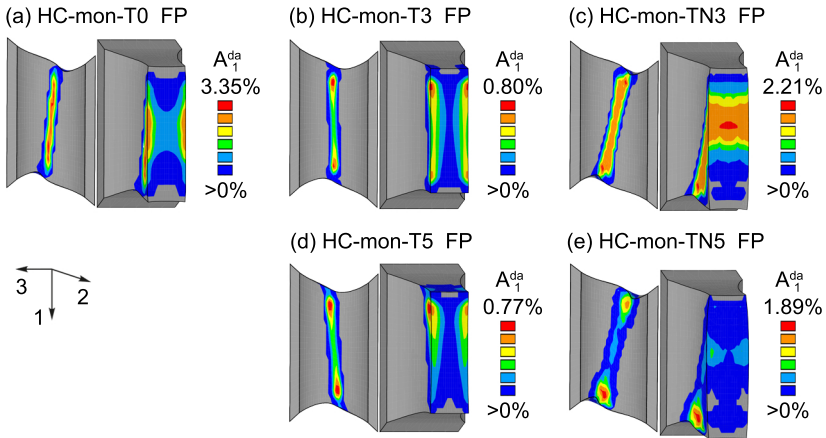

Figure 5.21: Numerically predicted damage strains A_1^{da} on the surfaces 12 and in the cross-sections 13 of the HC-specimens (Wei et al., 2023b).

A_1^{da} are numerically predicted on the notch surfaces. It is worth noting that the predicted damage strains distribution on the surface and notch cross-section for the HC-mon-T0 test is similar to the distribution of damage strains in the S-mon-T test (Fig. 5.9(a)). In the HC-mon-T3 and HC-mon-T5 experiments, the damage strains are highly localized on the top and bottom of the notch surfaces, with values of 0.80% and

0.77%, respectively, and the damage strains mainly appear at the edge of the notched cross-sections. Moreover, the maximum damage strain $A_1^{da} = 2.21\%$ occurs in the notched cross-section in the HC-mon-TN3 experiments, see Fig. 5.21(c). In addition, the damage strains are significantly larger on the notch surface than in the notched cross-section for the test HC-mon-TN5, with a maximum value of 1.89% on the right-top and left-bottom of the notch surface.

Furthermore, SEM images taken from the fracture surfaces under monotonic loading tests are illustrated in Figs. 5.23(a1)-(e1). On the one hand, micro-shear-cracks, predominantly caused by negative and low positive stress triaxialities, are observed in experiments HC-mon-T0, HC-mon-TN3, and HC-mon-TN5, with numerically predicted mean stress triaxialities of 0.08, -0.06, and -0.13, respectively, see Fig. 5.18(a). On the other hand, micro-voids and micro-shear-cracks are visible for the tests HC-mon-T3 and HC-mon-T5, see Figs. 5.23(b1) and (d1). The mean stress triaxialities for the HC-mon-T3 and HC-mon-T5 experiments are 0.22 and 0.32, respectively, resulting in deeper and larger micro-voids in the loading pattern HC-mon-T5 compared to the micro-voids in the HC-mon-T3 test. The above-mentioned microscopic findings confirm that the dependency of damage mechanism on stress states.

The development of damage strains A_1^{da} during the loading processes is shown in Fig. 5.23 to study how the reverse loading and loading histories affect the damage behavior. There is no damage numerically predicted on both the notch surfaces and notched cross-sections at RP1 for the tests superimposed by zero or positive preloads (3 kN and 5 kN). To contrast, damage strains with maximum values of $A_1^{da} = 0.81\%$ and $A_1^{da} = 1.80\%$ appear on the notch surfaces as points in experiments HC-cyc-TN3 and HC-cyc-TN5, respectively. Subsequently, damage strains occur and develop in significantly different manners for various loading patterns. For instance, damage strains increase by 0.23% on the top of the notch surface from RP1 to RP2, and then reach a maximum value of 0.40% on the bottom of the notch surface from RP2 to FP for the HC-cyc-T3 experiment. Compared to the HC-cyc-T3 test, the damage strains ($\Delta A_1^{da} = 0.44\%$) are mainly develop at the top edge of the notched surfaces in the last loading pattern in HC-cyc-T5 experiment, as shown in Fig. 5.23(d). Conversely, damage strains predominantly increase in the center of the notched cross-sections after the first reverse loading (RP1 to

(a1) HC-mon-T0 FP

(a2) HC-cyc-T0 FP

(b1) HC-mon-T3 FP

(b2) HC-cyc-T3 FP

(c1) HC-mon-TN3 FP

(c2) HC-cyc-TN3 FP

(d1) HC-mon-T5 FP

(d2) HC-cyc-T5 FP

(e1) HC-mon-TN5 FP

(e2) HC-mon-TN5 FP
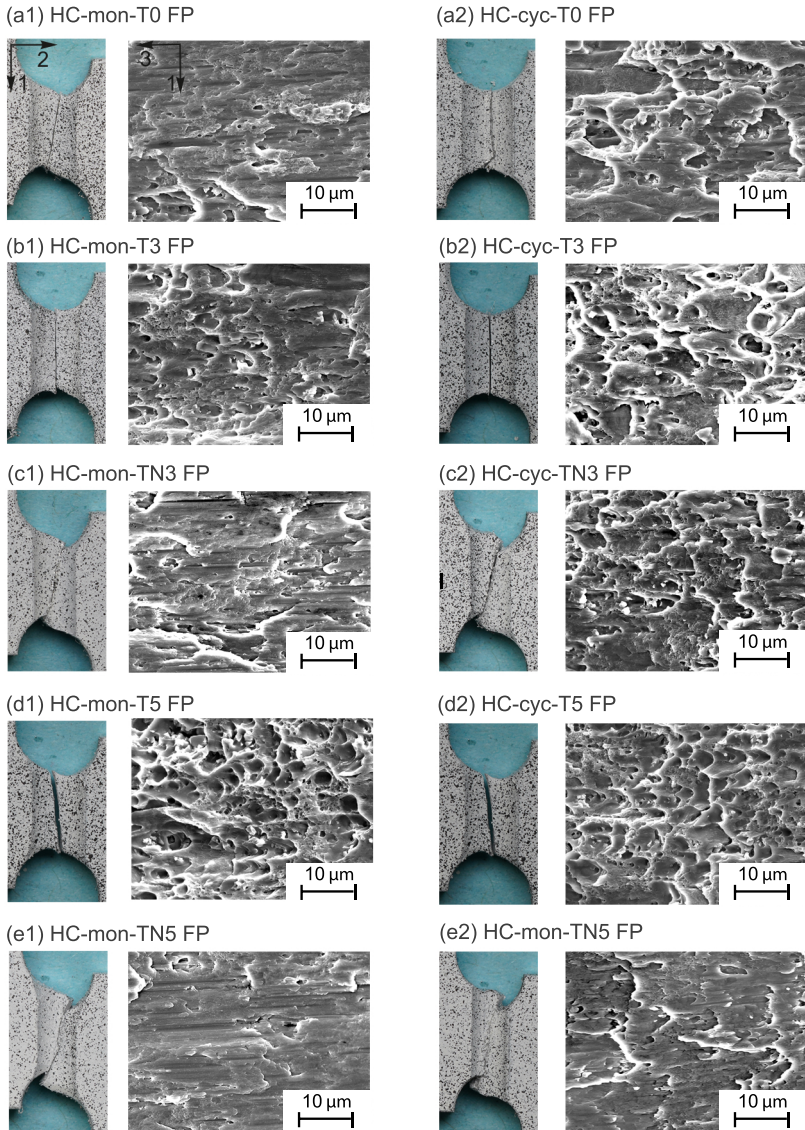
Figure 5.22: Fracture pictures and SEM images for the monotonic and cyclic loading tests superimposed by different tensile or compressive preloads (Wei et al., 2023b).
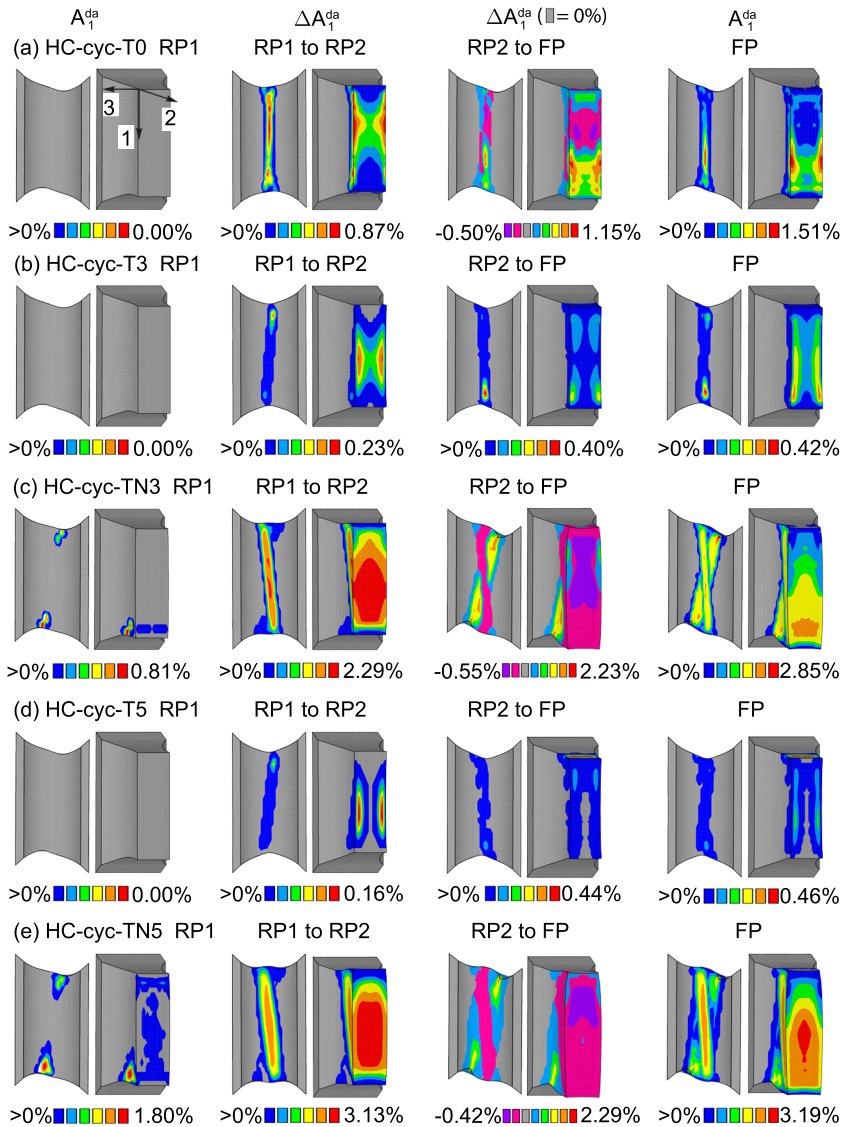
Figure 5.23: The changes in the first principal damage strains ΔA_1^{da} at various reverse points (RPs) and fracture point (FP) (Wei et al., 2023b).

RP2) for tests with negative preloads ($-3\,\mathrm{kN}$ and $-5\,\mathrm{kN}$). Subsequently, the damage strains then develop on the notch surfaces, as observed in Figs. 5.23(c) and (e). Obviously, the preloads and reverse loading conditions significantly influence the evolution of damage strains.

In addition, SEM images for cyclic experiments with different preloads are depicted in Figs. 5.22(a2)–(e2), respectively. It is evident that more larger coalesced micro-shear-cracks and micro-voids are visible under cyclic loading conditions than those undergoing monotonic loading conditions. Furthermore, the micro-voids exhibit greater depth with a preload of $5\,\mathrm{kN}$ compared to those with $3\,\mathrm{kN}$, given the higher mean stress triaxiality of $\bar{\eta} = 0.34$ for the HC-cyc-T5 test compared to $\bar{\eta} = 0.25$ in HC-cyc-T3. Also, micro-voids are significantly larger for the tests with positive preloads than those in the experiments with negative preloads. A potential explanation is that experiments with positive preloads induced predominantly positive stress triaxialities throughout the entire loading process (Figs. 5.19(b) and (d)), leading to the continuous growth of micro-voids and a positive incremental damage strain, as observed in Figs. 5.21(b) and (d). These facts prove that reverse loading conditions alter the matrix of the material at the microscopic level, leading to different macroscopic material behavior.

5.3.2 Summary

A series of non-proportional biaxial shear monotonic and cyclic loading experiments, superimposed with various tensile or compressive preloads, were conducted to investigate plastic, damage, and fracture behavior. Experiments with tensile preloads result in positive stress triaxialities ranging from 0.2 to 0.34, while tests with negative or zero preloads induce stress triaxialities in the range of -0.25 to 0. These experiments effectively bridge the gap between uniaxial tension-compression tests and one-axial shear cyclic experiments. The alteration in the hardening ratio after shear reverse loading, akin to the observations in the one-axial shear experiments, is effectively addressed by the proposed most straightforward hardening correction method, ensuring accurate improvement in numerical results. In addition, the strain Lode parameter, along with the stress triaxiality and the stress Lode parameter, is suggested to distinguish the stress state for different loading cases and loading histories,

particularly within different shear cyclic conditions.

An increase in compressive preloads enhances the ductility of the material, whereas an increase in tensile preloads leads to increased brittleness. Micro-shear-cracks predominantly initiate damage when negative or zero preloads are superimposed, whereas micro-defects contribute to damage in experiments with positive preloads. Larger and coalesced micro-defects are more prominent under cyclic loading than monotonic loading, contributing to a more pronounced material degradation. These SEM images provide apparent evidence that the stress states and reverse loading conditions significantly influence the damage behavior at the microscopic level. Moreover, analyzing the numerical results for global load–displacement curves, local total strain fields, and damage strain fields provides insights into how preloads, loading histories, and reverse loading influence plastic, damage, and fracture behaviors at both macro- and microscopic levels.

5.3.3 Tensile reverse experiments superimposed by shear preloads

Global load–displacement curves

The experimental and numerical load–displacement curves are shown in Fig. 5.24. It is obvious that the numerical results show good agreements with the experimental ones, see Figs. 5.24(b)–(f). However, the numerically predicted load–displacement curves for the final tensile reverse loading pattern exhibit a slight discrepancy compared to the experimental ones. The experimental and numerical results for the shear reverse experiments superimposed by tensile or compressive preloads in Section 5.3.1 demonstrate a considerable change in the hardening ratio (non-hardening effect) after shear reverse loading conditions. Conversely, the numerically predicted results for tensile reverse experiments without non-hardening correction can accurately capture the reversal yield stresses and the load–displacement curves after the first tensile reverse loading condition, indicating the insignificant role of the non-hardening effect under tensile reverse loading conditions. Therefore, the non-hardening effect is not considered under biaxial tensile reverse conditions.

Furthermore, the load–displacement curves in axis 2 (tension axis) for monotonic and cyclic loading tests are illustrated in Fig. 5.24(a), where
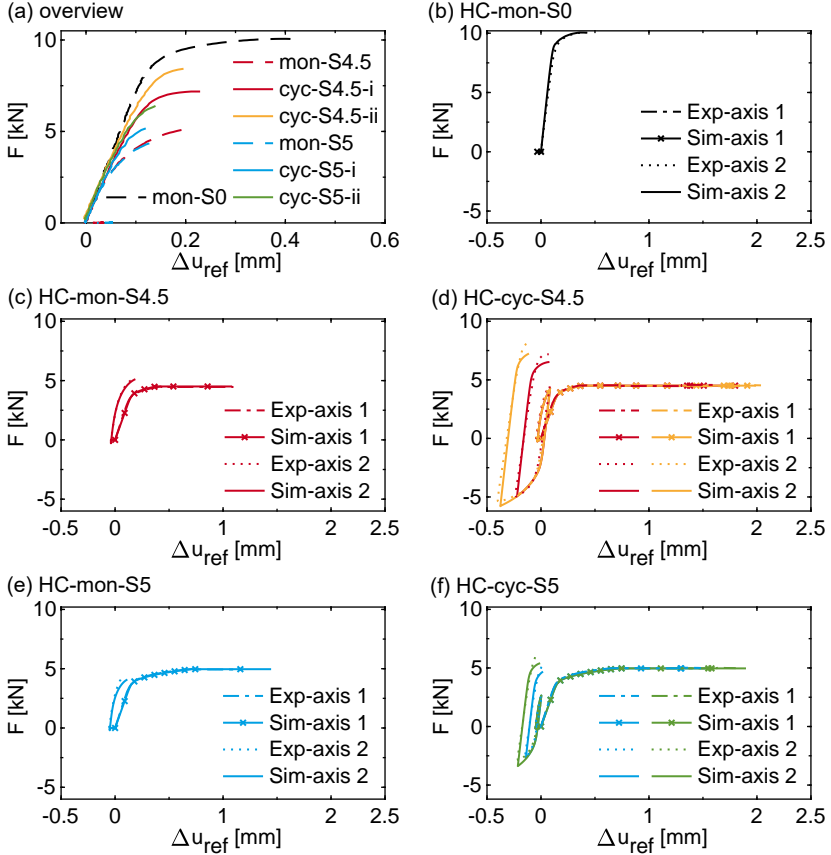
Figure 5.24: Numerical and experimental load–displacement curves for monotonic and tensile cyclic tests (Wei et al., 2024b).

all curves are aligned with starting points in the zero displacements. In addition, the fracture forces F_2^{fr} and fracture displacements $\Delta u_{1,\mathrm{ref}}^{\mathrm{sw}}$, $\Delta u_{2,\mathrm{rel}}^{*}$, and $\Delta u_{2,\mathrm{ref}}^{\mathrm{fr}}$ are listed in Table 5.3. The non-proportional fracture displacement $\Delta u_{1,\mathrm{ref}}^{\mathrm{sw}}$ describes the displacement increment of axis 1 (shear axis) from the second loading stage (after preloading) up to the specimen failure, see Table 5.3. Additionally, the relative reverse frac-

ture displacement $\Delta u_{2,\mathrm{rel}}^*$ denotes the displacement increment from zero force to final fracture after the second tensile reverse loading. It can be observed that fracture displacements $\Delta u_{2,\mathrm{ref}}^{\mathrm{fr}}$ and the corresponding fracture forces F_2^{fr} obviously decrease with an increasing shear preloads F_1 under monotonic loading conditions, as shown in Fig. 5.24(a) and Table 5.3. This observation reveals that the shear preload increases the brittleness of the investigated ductile aluminum alloy.

Table 5.3: Fracture forces F_2^{fr} and fracture displacements $\Delta u_{1,\mathrm{ref}}^{\mathrm{sw}}$, $\Delta u_{2,\mathrm{rel}}^*$, and $\Delta u_{2,\mathrm{ref}}^{\mathrm{fr}}$ (Wei et al., 2024b).

Preload F_1 [kN]	monotonic (mon-)			cyclic loading (cyc-)				
	$\Delta u_{2,\mathrm{ref}}^{\mathrm{fr}}$ [mm]	$\Delta u_{1,\mathrm{ref}}^{\mathrm{sw}}$ [mm]	F_2^{fr} [kN]	Loading paths	$\Delta u_{2,\mathrm{ref}}^{\mathrm{fr}}$ [mm]	$\Delta u_{2,\mathrm{rel}}^*$ [mm]	$\Delta u_{1,\mathrm{ref}}^{\mathrm{sw}}$ [mm]	F_2^{fr} [kN]
0	0.42	n/a	10.05	n/a	n/a	n/a	n/a	n/a
4.5	0.22	0.66	5.16	S4.5-i	0.07	0.23	1.29	7.18
				S4.5-ii	-0.10	0.21	1.52	8.17
5	0.13	0.43	4.27	S5-i	0.01	0.12	0.81	5.17
				S5-ii	-0.03	0.14	1.09	6.22

In the case of cyclic experiments, the relative reverse fracture displacements $\Delta u_{2,\mathrm{rel}}^*$ also reduce by increasing the shear preload, as observed undergoing monotonic loading conditions. Although the relative fracture displacements show no apparent difference between monotonic and cyclic loading experiments, the fracture forces for the cyclic experiments are evidently greater than those undergoing monotonic loading conditions. As depicted in Fig. 5.24(a), the material exhibits increased brittleness during tensile reverse loading compared to monotonic loading, leading to rapid failure as the specimens reach the reverse tensile yield limit. Moreover, the fracture force $F_2^{\mathrm{fr}} = 8.17\,\mathrm{kN}$ for the HC-cyc-S4.5-ii is higher than $F_2^{\mathrm{fr}} = 7.18\,\mathrm{kN}$ in the HC-cyc-S4.5-i experiment, and the same trend can also be observed between experiments HC-cyc-S5-ii and HC-cyc-S5-i. It is worth noting that in loading patterns HC-cyc-S4.5-ii and HC-cyc-S5-ii, only a higher compressive load is imposed compared to HC-cyc-S4.5-i and HC-cyc-S5-i, respectively, resulting in a obviously greater fracture force, see Figs. 5.24(d) and (f). It indicates that the reversal yield stress and fracture force are significantly affected by the tensile reverse loading histories. In addition, the non-proportional fracture displacement $\Delta u_{1,\mathrm{ref}}^{\mathrm{sw}}$

for the mon-S5 experiment is greater than that one in the mon-S4.5 test. This results in a more limited range of compressive loading patterns for the cyclic experiments with $F_1 = 5\,\text{kN}$ that can be chosen in the present study.

The experimental analysis of fracture displacements and forces emphasizes the significant impact of shear preload, its magnitude, and different cyclic loading patterns on increasing the brittleness of the material. Additionally, the influence of tensile reverse loading conditions and the extent of compressive loading patterns is clearly evident in plastic, damage, and fracture behavior compared to monotonic loading.

Local strain fields

The distribution of the first principal strains A_1 and strain increments ΔA_1 during the loading processes are illustrated in Fig. 5.25, respectively. The numerically predicted strain fields align well with the experimental results obtained from DIC. The first principal strain A_1 distribution on the notch surface takes the form of an ellipse, reaching a maximum value of 0.13 in the HC-mon-S0 test. With an increase in shear preload, the principal strains along the shear band on the notch surfaces exhibit higher maximum values, such as $A_1 = 0.26$ for HC-mon-S4.5 and $A_1 = 0.32$ for HC-mon-S5. Furthermore, the shear band in the HC-mon-S5 test appears straighter compared to that in the HC-mon-S4.5 experiment. These observations suggest that shear preloads significantly affect the distribution of the first principal total strains A_1 and alter the strain states during the monotonic experiments.

In the case of cyclic loading, the maximal value of the first principal strain A_1 at FP is 0.49 for the loading pattern HC-cyc-S4.5-ii, exceeding that one of the HC-cyc-S4.5-i loading pattern ($A_1 = 0.41$), as depicted in Figs. 5.25(b2) and (b3). Moreover, the larger compressive loading pattern (cyc-S4.5-ii) not only localizes strains but also causes the shear band to become more discontinuous, deformed, and twisted. Additionally, the strain increment ΔA_1 from RP1 to RP2 is twice as large under the loading path cyc-S4.5-ii compared to the one in the cyc-S4.5-i loading pattern, where strains are highly localized in the top and bottom of the shear band. However, an opposite trend is predicted during the RP2 to FP, see Figs. 5.25(b2) and (b3). A similar trend can be seen for the cyclic
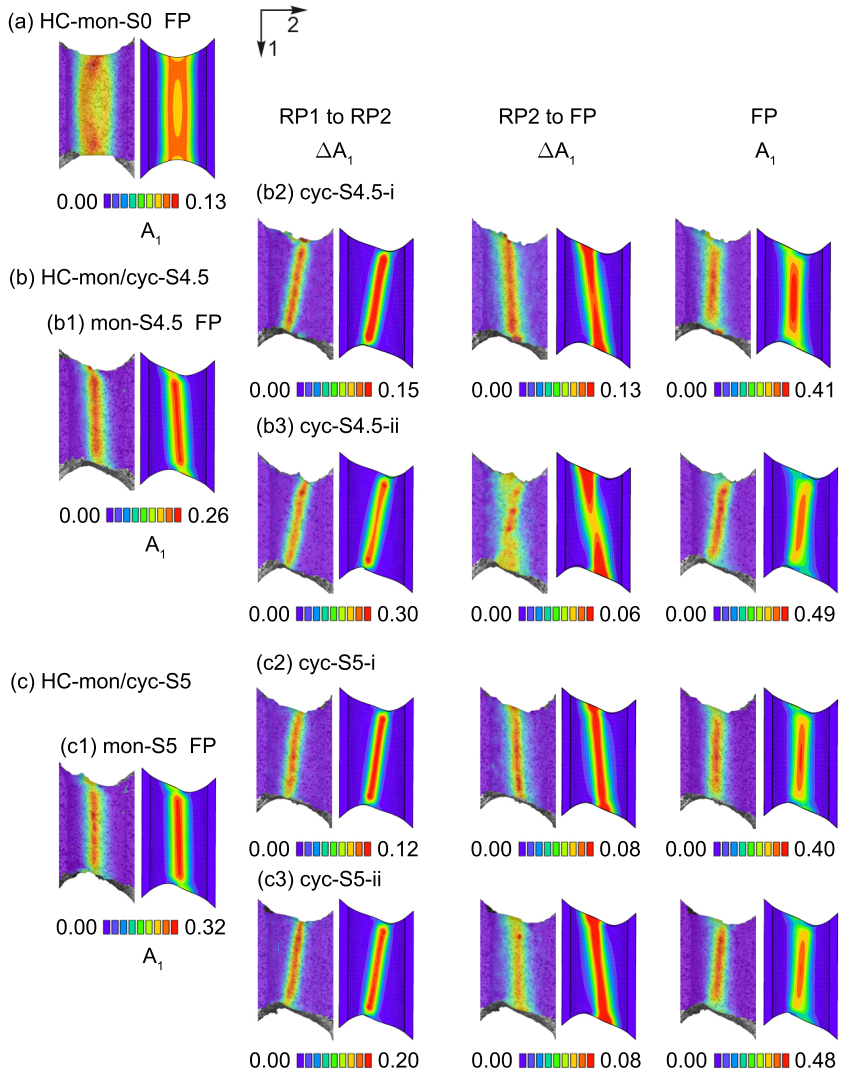
Figure 5.25: Experimental (left) and numerically predicted (right) first principal total strains A_1 and strain increments ΔA_1 on the notch surfaces (surface 12) at reverse point 1 (RP1) and fracture point (FP), and RP1 to reverse point 2 (RP2) and RP2 to FP (Wei et al., 2024b).

loading experiments HC-cyc-S5-i and HC-cyc-S5-ii in Figs. 5.25(c2) and
(c3). Moreover, the change in the loading direction results in alterations
in the direction of the shear band.

Based on both experimental and numerical analyses of strain fields, it
is evident that the loading patterns and histories employed substantially
influence plastic behavior and resultant strain states. In particular, a
larger compressive load in the second loading stage leads to a more dis-
continuous distribution of the strain on the notch surface.

5.3.4 Damage strains, stress states and SEM pictures

The mean stress triaxiality $\bar{\eta}$ and the mean stress Lode parameter $\bar{\omega}$
over the notched cross-section are shown in Figs. 5.26(a)–(c). Moreover,
Fig. 5.26(d) depicts the relationship between the mean strain Lode pa-
rameter $\bar{\omega}_A$ and the mean equivalent strain $\bar{\varepsilon}_{\mathrm{eq}}$ at the RP1, RP2 and
FP. In addition, Fig. 5.27 illustrates the occurrence and development of
the damage strains during the loading processes to analyze the influence
of loading histories on damage. Finally, Fig. 5.28 shows the fracture
pictures and SEM images to verify the damage mechanisms.

As shown in Fig. 5.26(c), experiment HC-mon-S0 exhibits the maxi-
mum mean stress triaxiality $\bar{\eta} = 0.71$, leading to a large damage strain
$A_1^{\mathrm{da}} = 8.67\%$ localized in the notched cross-section, see Fig. 5.27(a).
Moreover, many large and deep micro-voids and dimples can be seen in
the fracture surface, along with jagged fracture lines visible on the notch
surface, indicative for high stress triaxialities, as observed in SEM image
Fig. 5.28(a). In addition, the numerical predictions show maximum dam-
age strains of $A_1^{\mathrm{da}} = 0.32\%$ and $A_1^{\mathrm{da}} = 0.13\%$ in the notched cross-section
for experiments HC-mon-S4.5 and HC-mon-S5, respectively. Compared
to the loading case HC-mon-S0, damage strains are additionally numer-
ically predicted for the experiments HC-mon-S4.5 and HC-mon-S5 on
the notch surfaces. As shown in Fig. 5.26(c), the mean stress triaxial-
ity $\bar{\eta}$ decreases with increasing shear preloads. For example, the mean
stress triaxiality for tests HC-mon-S4.5 and HC-mon-S5 are 0.33 and
0.28, respectively. In SEM images, Figs. 5.28(b)–(c), both micro-voids
and micro-shear-cracks are visible, with the depth of the micro-voids
significantly shallower than those in the pure tensile test HC-mon-S0.
Moreover, larger coalesced micro-voids are observed in the HC-mon-S4.5
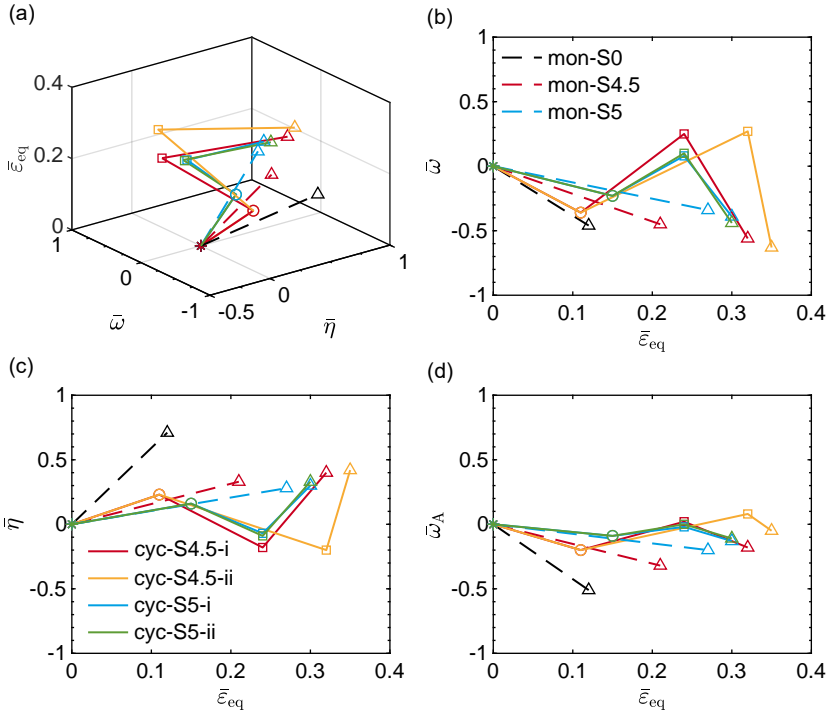
Figure 5.26: Figs. (a)–(c) illustrate the mean equivalent strain $\bar{\varepsilon}_{\mathrm{eq}}$ versus the mean stress triaxiality $\bar{\eta}$ and the mean stress Lode parameter $\bar{\omega}$ over the notched cross section for monotonic and cyclic experiments, and (d) depicts the relation between the mean equivalent strain $\bar{\varepsilon}_{\mathrm{eq}}$ and the mean strain Lode parameter $\bar{\omega}_A$. The symbols $\bigcirc$ = RP1, $\square$ = RP2, and $\triangle$ = FP (Wei et al., 2024b).

experiment compared to the HC-mon-S5 test. Smooth shear-band-like fracture lines are detected in Figs. 5.28(b)–(c) compared to the experiment HC-mon-S0. These findings highlight that damage is caused by the growth and coalescence of micro-voids under high stress triaxialities, and stress states could also further affect the depth of the micro-voids

and the occurrence of micro-shear-cracks.

Concerning the cycling loading, the stress states significantly alter during the loading processes. For the loading case HC-cyc-S4.5-i, the stress triaxialities change from 0.24 at RP1 to -0.18 during the compressive loading pattern, and finally, it reaches 0.40. Experiment HC-cyc-S4.5-ii generates similar stress triaxialities at RP1, RP2, and FP, with values of 0.24, -0.20, and 0.40, respectively, as illustrated in Figs. 5.26(a)–(c). Also, the stress triaxialities decrease with increasing shear preloads, as observed in the monotonic loading test. The stress triaxialities for the loading pattern HC-cyc-S5-i are 0.16, -0.07, and 0.30 at RP1, RP2, and FP, respectively. In addition, the corresponding values are 0.16, -0.09, and 0.33, respectively, for the experiment HC-cyc-S5-ii. It is evident that the alteration of the stress triaxialities results in different damage evolutions, as illustrated in Fig. 5.27.

As shown in Figs. 5.27(b2)–(b3), the damage strains A_1^{da} are numerically predicted on the notched surface, with a maximum value of 0.08% in the notched cross-section at RP1. Although different compressive displacements are imposed for loading patterns HC-cyc-S4.5-i and HC-cyc-S4.5-ii, the maximum damage strain increments ΔA_1^{da} show no apparent difference. One possible reason could be that the stress triaxialities from RP1 to RP2 are close to the cut-off value of $-1/3$, resulting in nearly no further damage occurring and developing. During the last loading stage, i.e., RP2 to FP, damage mainly develops in the notched cross-section and at the edge of the notched cross-section for the loading cases HC-cyc-S4.5-i and HC-cyc-S4.5-ii. Their related damage strains are 0.08% and 0.01%. However, the mean stress triaxialities and the stress Lode parameters differ only by 0.02 and 0.07 between experiments HC-cyc-S4.5-i and HC-cyc-S4.5-ii, respectively. Moreover, the damage strains just before failure (FP) are 1.65% and 1.62%, respectively, evidently greater than those observed in monotonic tests. It indicates that the loading histories significantly influence the development of damage. In addition, some coalesced larger micro-voids and micro-shear-cracks are obviously visible in SEM pictures Figs. 5.28(b2)–(b3). As discussed, negative stress triaxialities from RP1 to RP2 induce these micro-shear-cracks and their coalescence during loading. Furthermore, the depth of the micro-voids becomes deeper under cyclic loading conditions compared to monotonic loading, particularly in the HC-cyc-S4.5-i experiment.
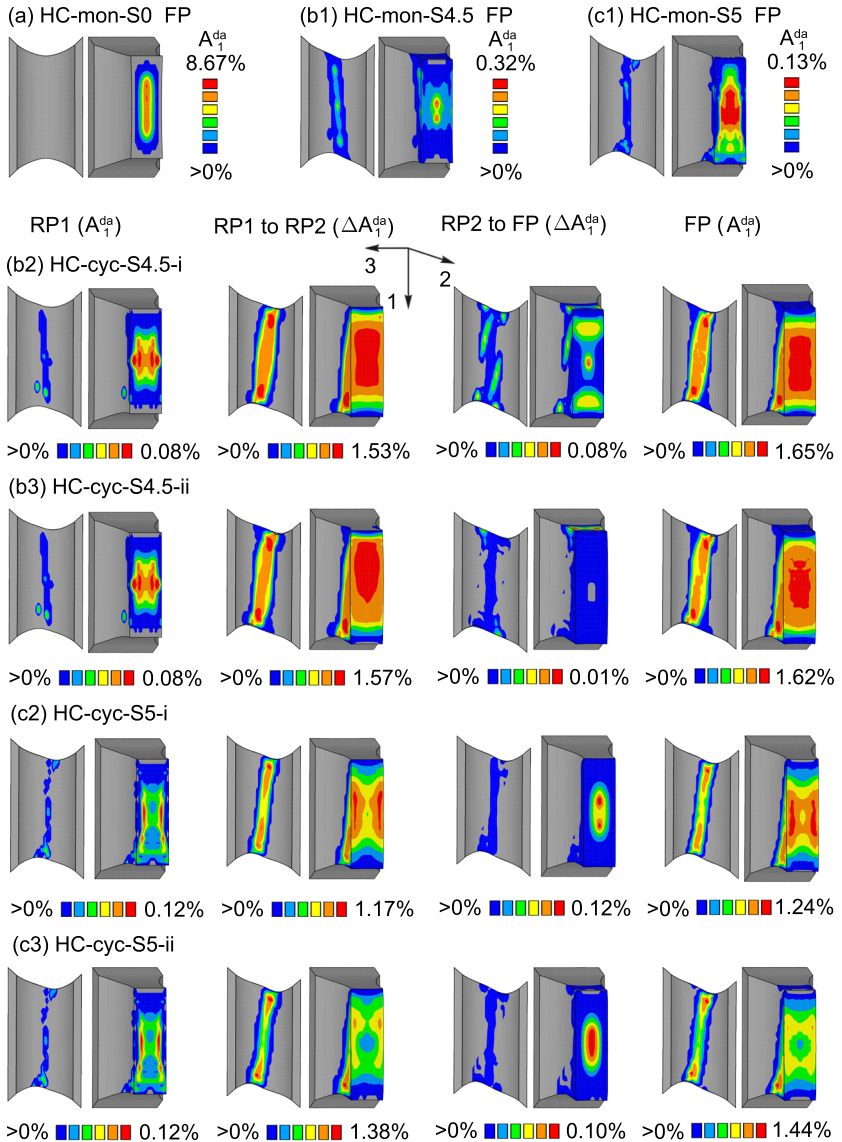
**Figure 5.27:** The first principal damage strains A_1^{da} and their increments ΔA_1^{da} on the notched surfaces (surface 12) and notched cross-sections (surface 13) for the monotonic and cyclic loading tests (Wei et al., 2024b).

For cyclic experiments with $5\,\mathrm{kN}$ shear preload, damage strains are observed on the notch surface and notched cross-section at RP1, where the numerically predicted maximum damage strain A_1^{da} is 0.12% at the edge of the notched cross-section. Subsequently, different distributions and values are detected between loading patterns HC-cyc-S5-i and HC-cyc-S5-ii after the first compressive reverse loading, see Figs. 5.27(c2)–(c3). However, the stress states are nearly the same at RP2, i.e., $\bar{\eta} = -0.07$ and $\bar{\omega} = 0.08$. It must be emphasized that there are no apparent differences in the development of the damage strains, even when larger compressive displacements are imposed in the HC-cyc-4.5-ii experiment compared to the loading pattern HC-cyc-4.5-i. Thus, this highlights the influence of stress state on the damage behavior. In the last loading path (RP2–FP), damage strains mainly develop and are localized as an ellipse in the notched cross-sections. Moreover, the maximum damage strain $A_1^{\mathrm{da}} = 1.24\%$ appears in the notched cross-section for the HC-cyc-S5-i experiment, whereas $A_1^{\mathrm{da}} = 1.44\%$ are observed on the notch surface in the test HC-cyc-S5-ii. Compared to monotonic loading (Fig. 5.27(c)), a few larger micro-voids and predominate micro-shear-cracks are observed in Figs. 5.27(c1) and (c2). Micro-shear-cracks are formed and developed during the loading stage from RP1 to RP2, where micro-shear-cracks in loading pattern HC-cyc-S5-ii are more significantly visible in the SEM images than in the HC-cyc-S5-i loading case. This is caused by larger compressive displacement imposed in the HC-cyc-S5-ii test, where the near-zero stress triaxialities further result in the coalescence of micro-shear-cracks. Moreover, some larger micro-voids can also be observed under cyclic conditions compared to the related monotonic loading tests.

5.3.5 Summary

Biaxial tensile reverse experiments superimposed by different shear preloads are performed to study the plastic, damage, and fracture behavior. The high stress triaxiality $\eta = 0.71$ is generated in the monotonic tensile test HC-mon-S0. Most importantly, the stress states significantly change during compressive and tensile reverse loading conditions, resulting in different damage mechanisms during the loading processes. In the numerical simulations, damage strains and their increments clearly reveal how the loading histories and stress states influence the occurrence and

(a) HC-mon-S0 FP
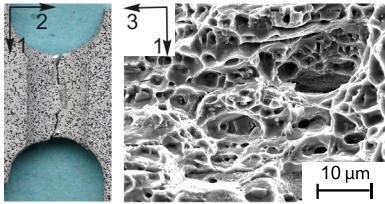
(b) HC-mon-S4.5 FP
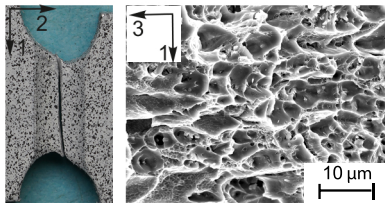
(c) HC-mon-S5 FP
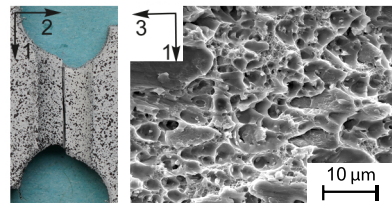
(b1) HC-cyc-S4.5-i FP
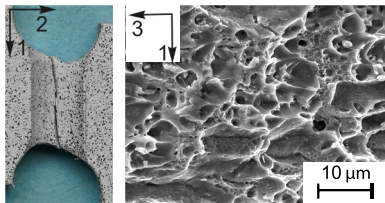
(c1) HC-cyc-S5-i FP
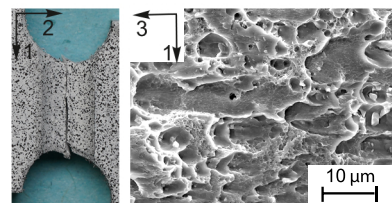
(b2) HC-cyc-S4.5-ii FP
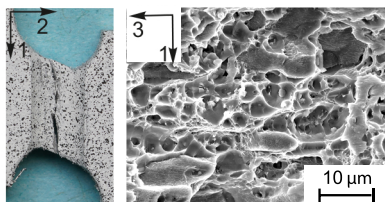

(c2) HC-cyc-S5-ii FP
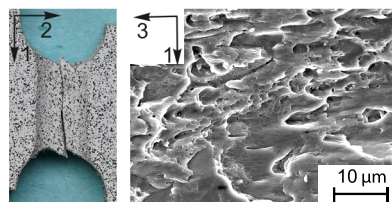
Figure 5.28: Fracture pictures taken from fractured notched surfaces (surface 12) and SEM pictures taken from fractured notched cross-sections (surface 13) for monotonic and cyclic experiments (Wei et al., 2024b).

development of damage. Based on the global load–displacement curves, the change of the hardening ratio after tensile reverse loading is not significant compared to that one after shear reverse loading. However, the reverse yield stresses increase significantly after compressive reverse loading, where the degrees of compressive loading patterns also affect the reverse yield stresses by comparing different loading patterns -i and -ii with the same shear preloads. As discussed in Wei et al. (2023c, 2024b), one possible explanation is that the preformed micro-shear-cracks expand in the direction of increasing hydrostatic pressure after compressive reverse loading condition. This change in direction causes deformed voids and cracks to become more challenging.

Furthermore, the material becomes brittle with increasing shear preloads or under cyclic loading conditions. Also, the generated stress triaxialities decrease by superimposing a higher shear preloads. On the one hand, as observed in SEM image for the pure tension test (HC-mon-S0), the damage is caused by the growth and coalescence of the micro-voids. On the other hand, micro-shear-cracks and micro-voids are both visible in the tensile reverse experiments with different shear preloads. Moreover, larger and coalesced micro-defects are observed under cyclic loading conditions compared to those in the monotonic tests with different shear preloads, and the micro-voids are deeper with increasing stress triaxialities. These findings highlight the dependence of the stress states on the damage mechanisms.

5.4 Bi-cyclic biaxial tests

Global force-displacement curves

The experimental and numerical load–displacement curves for bi-cyclic biaxial experiments are illustrated in Fig. 5.29. It is evident that the numerically predicted load–displacement curves agree well with the experimental ones. The comparison of fracture displacements in Table 5.4 indicates that pure negative cyclic loading patterns (CCC, without reverse loading in axis 2) lead to an increase in the ductility of the material compared to experiments with pure positive loading patterns (TTT, without reverse loading in axis 2). Moreover, the fracture displacements ($\Delta u_{1,\mathrm{ref}}^{\mathrm{fr}}$ and $\Delta u_{1,\mathrm{rel}}^{*}$) and forces F_1^{fr} are listed in Table 5.4. In addition,
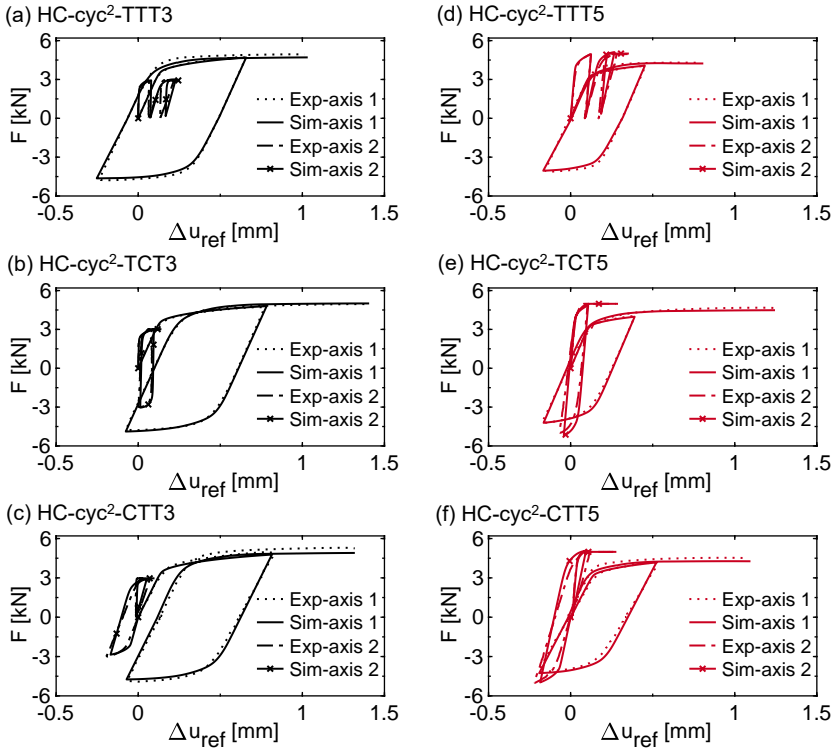
Figure 5.29: Numerical and experimental load–displacement curves for
bi-cyclic biaxial tests (Wei et al., 2024a).

applying an increased superimposing positive load (HC-cyc^2-xxT3 and
-xxT5) in the final loading stage enhances the brittleness of the mate-
rial. Conversely, applying an increased superimposing negative load (HC-
cyc^2-xxC3 and -xxC5) in the last loading stage increases the ductility of
the material, as shown in Table 5.4. On the other hand, cyclic load-
ing patterns incorporating reverse loading increase ductility compared
to those without reverse loading. However, the forces causing fracture
demonstrate divergent trends under positive (HC-cyc^2-xxT3 and -xxT5)
and negative (HC-cyc^2-xxC3 and -xxC5) final superimposed loads. For
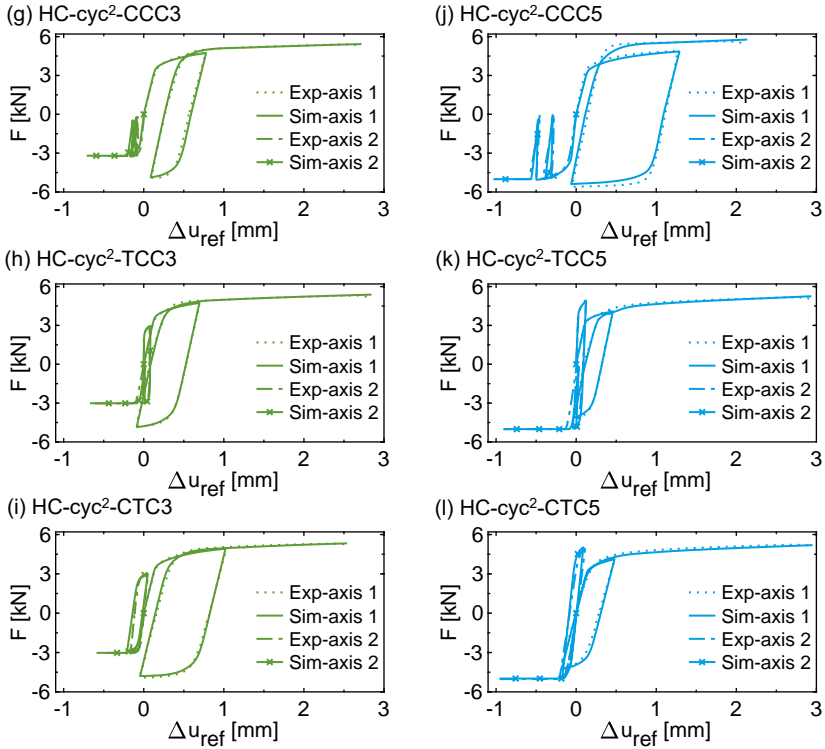
Figure 5.29: Numerical and experimental load–displacement curves for
bi-cyclic biaxial tests (continuation) (Wei et al., 2024a).

instance, the fracture forces increase in experiments with superimposed
final positive loads but decrease in tests involving final negative loads,
as observed in Table 5.4. Furthermore, cyclic loading patterns TCT
and CTT, as well as TCC and CTC, exhibit distinct irregular influences
on the global load–displacement curves, along with varying effects on
fracture forces and displacements. However, this underscores that the
loading sequences evidently influence the macro-level material behavior,
particularly in terms of fracture displacements and forces. In conclusion,

the variations in loading patterns and magnitudes of superimposed load markedly alter macroscopic material behavior.

Table 5.4: Fracture forces F_1^{fr} and fracture displacements $\Delta u_{1,\mathrm{ref}}^{\mathrm{fr}}$ and $\Delta u_{1,\mathrm{rel}}^*$ (Wei et al., 2024a).

Tests HC-	positive superimposed loads at last loading stage			Tests HC-	negative superimposed loads at last loading stage		
	$\Delta u_{1,\mathrm{ref}}^{\mathrm{fr}}$ [mm]	$\Delta u_{1,\mathrm{rel}}^*$ [mm]	F_1^{fr} [kN]		$\Delta u_{1,\mathrm{ref}}^{\mathrm{fr}}$ [mm]	$\Delta u_{1,\mathrm{rel}}^*$ [mm]	F_1^{fr} [kN]
cyc^2-TTT3	1.01	1.08	4.94	cyc^2-CCC3	2.68	2.42	5.31
cyc^2-TCT3	1.39	1.29	4.95	cyc^2-TCC3	2.79	2.71	5.20
cyc^2-CTT3	1.32	1.19	5.25	cyc^2-CTC3	2.52	2.36	5.24
cyc^2-TTT5	0.79	0.80	4.29	cyc^2-CCC5	2.09	1.93	5.42
cyc^2-TCT5	1.24	1.25	4.66	cyc^2-TCC5	2.92	2.82	5.03
cyc^2-CTT5	1.07	1.08	4.49	cyc^2-CTC5	2.95	2.95	5.07

Local strain fields

Fig. 5.30 displays the first principal strains A_1 on the notch surfaces at RP1, RP2, and FP for experiments with superimposed positive and negative loads in the final loading stage. The numerical simulations align closely with the measured experimental strains at different loading stages. It is observed that the first principal strains A_1 just before failure (FP), particularly in experiments subjected to negative loads in the final loading stage (Figs. 5.30(g)–(l)), are significantly larger than those in tests with positive loading at the same stage, see Figs. 5.30(a)–(f). This indicates that the material becomes more ductile under negative superimposed loads. Furthermore, it is observed that the strains distribute in a counterclockwise direction with an increased superimposed positive load (HC-cyc^2-xxT3 and -xxT5) and in a clockwise direction with increasing negative load (HC-cyc^2-xxC3 and -xxC5), as also detected in the single biaxial cyclic experiments, see Fig. 5.16 in Section 5.3.1. On the one hand, the maximum values of the first principal strains A_1 exhibit slight differences between RP1 and RP2 in experiments with non-reverse cyclic loading patterns along axis 2 (tension axis), namely TTT and CCC. However, the distribution of the first principal strains changes significantly in shape and direction; for example, strains distribute in a X-shape at RP2

for loading patterns HC-cyc^2-CCCx and -TTTx. On the other hand, A_1 becomes nearly zero in experiments involving reverse cyclic loading patterns along axis 2, see Figs. 5.30(b)–(c), (e)–(f), (h)–(i), and (k)–(l). It enables the study of how different previous loading patterns influence material behavior.

For experiments superimposed with positive load in the last loading pattern, the changes in A_1 from RP2 to FP for non-reverse cyclic loads (TTT) along axis 2 are significantly greater than those observed in tests with reverse cyclic patterns in axis 2 (TCT and CTT). For instance, the strain increases ΔA_1 are approximately 0.36 for experiments HC-cyc^2-TCT3, -CTT3, -TCT5, and -CTT5, respectively. This value is greater than the 0.25 observed in the loading pattern HC-cyc^2-TTT3, and the 0.20 detected in the experiment TTT5, see Figs. 5.30(g)–(l). This trend is also observed in tests superimposed with negative loads in the final loading stage, as illustrated in Fig. 5.30. This observation can be attributed to the reverse loading in axis 2 during the second loading stage. Interestingly, the strain increments ΔA_1 from RP2 to FP in experiments with tensile load in the third loading stage are marginally higher than those observed in single biaxial cyclic tests (H-mon-T3 and H-mon-T5, as shown in Fig. 5.16). Similarly, the strain increments ΔA_1 from RP2 to FP in experiments HC-cyc^2-TCC3/5 and -CTC3/5 are greater than those observed in tests HC-mon-TN3 and HC-mon-T5, respectively. These findings suggest that specimens under reverse loading, resulting in a near-zero strain state, may cause the material to become slightly stronger than when it is unloaded. Most importantly, this near-zero strain state can only be achieved in bi-cyclic biaxial tests rather than in single cyclic biaxial tests discussed in Section 5.3.1.

Furthermore, strain increments ΔA_1 from RP1 to RP2, as well as from RP2 to FP, and strains A_1 at failure (FP) show no apparent differences between loading patterns TCT and CTT, as depicted in Figs. 5.30(b)–(c) and (e)–(f). However, significant differences are observed in experiments with final negative superimposed loads (TCC and CTC), indicating that loading sequences alter material behavior. In addition, the material shows greater ductility in tests with the same bi-cyclic loading direction in both axes, e.g., HC-cyc^2-TCT and -TCC (see loading sketch in Fig. 4.10), compared to those subjected to opposite loading directions in axis 1 and axis 2 (HC-cyc^2-CTT and -CTC) during the first and sec-
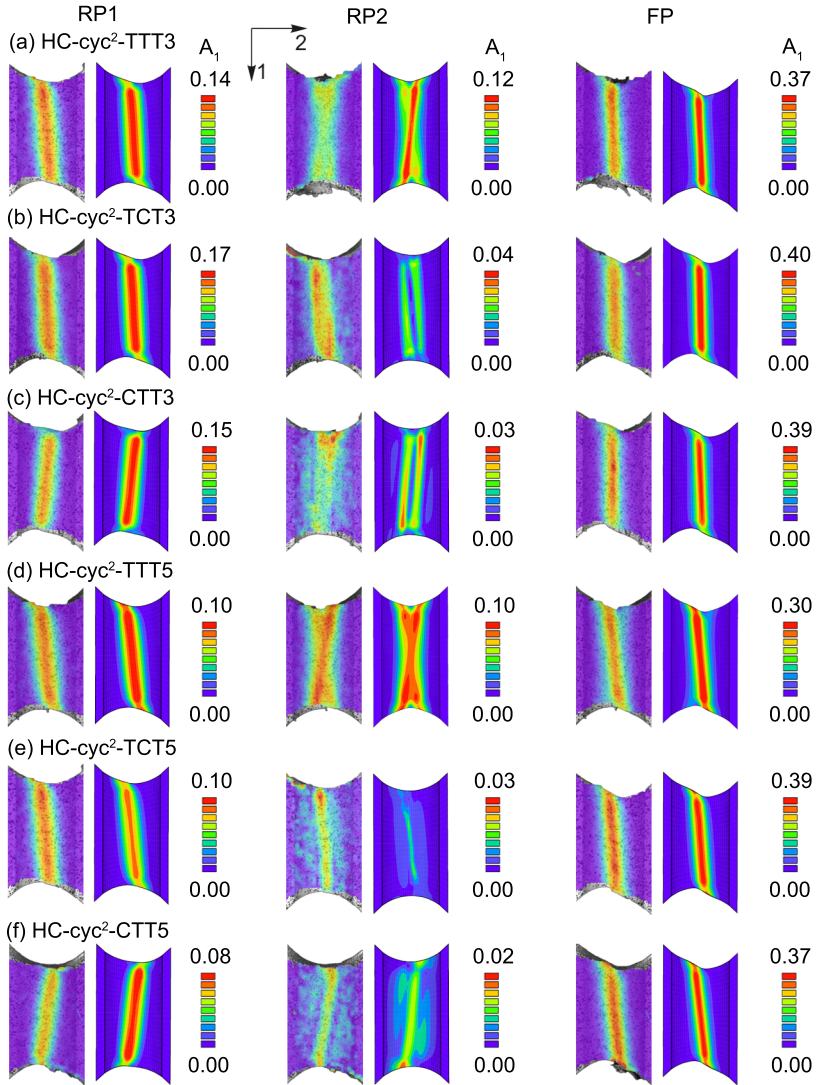
Figure 5.30: Experimental (left) and numerically predicted (right) the first principal strains A_1 on the notch surfaces at RP1, RP2 and FP (Wei et al., 2024a).
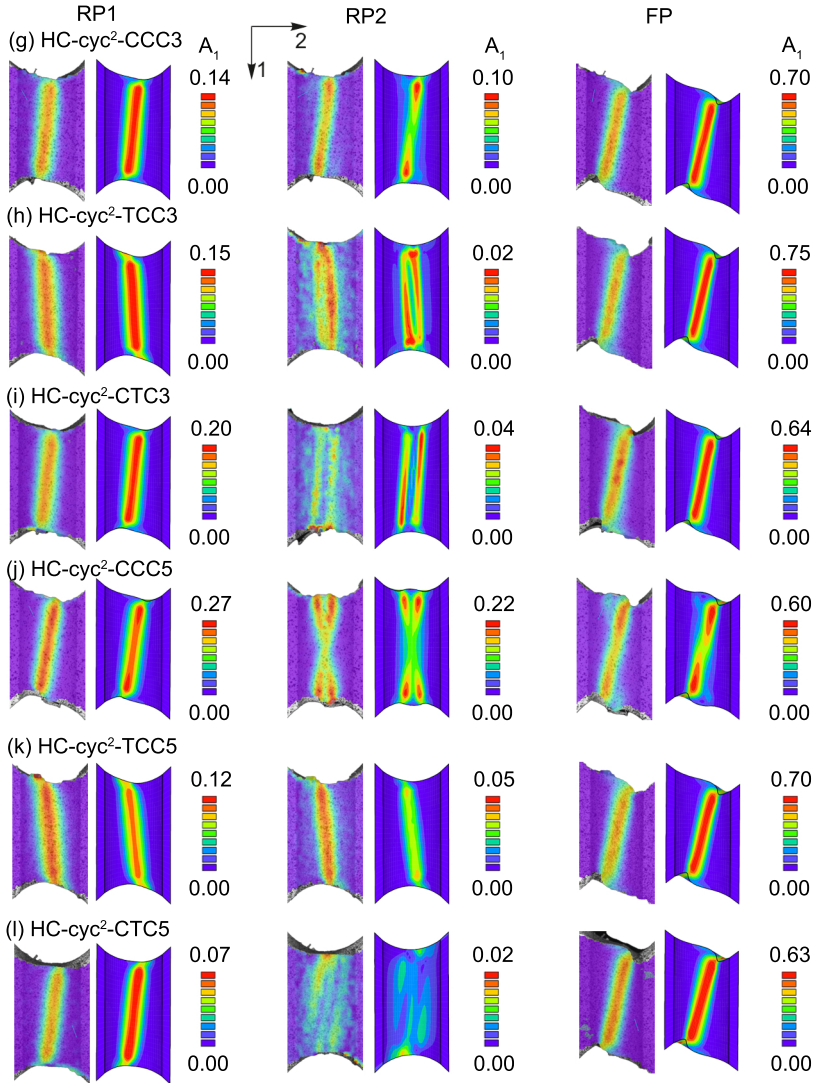
Figure 5.30: Experimental (left) and numerically predicted (right) the first principal strains A_1 on the notch surfaces at RP1, RP2 and FP(continuation) (Wei et al., 2024a).

ond loading stages. This is evident when comparing the strains at FP in Fig. 5.30. Based on the observations of the first principal strains, it is highlighted that loading sequences and histories significantly influence material behavior, particularly in terms of the different evolutions of the strain fields.

Damage strains, stress states, and SEM image

The mean stress triaxiality and the mean stress Lode parameter during the loading processes are depicted in Table 5.5 and Table 5.6, respectively. Positive stress triaxialities are generated when the tension axis (axis 2) is subjected to tensile loads at the last loading stage, while negative stress triaxialities result from negative loads imposed on the tension axis. Furthermore, an increase in either tensile or compressive loads in axis 2 leads to a corresponding increase in stress triaxiality and stress Lode parameter. Similarly, near-zero stress triaxialities are observed in the test with $-3\,\mathrm{kN}$ in the final loading stage, as seen in the single cyclic test HC-cyc-TN3 (Fig. 5.18), which had a compressive preload of $-3\,\mathrm{kN}$ on the tension axis. In addition, high stress triaxialities can be observed for the test with $5\,\mathrm{kN}$ in the final loading stage. Thus, the designed experiments enable the generation of different stress triaxialities and stress Lode parameters, significantly altering these triaxialities by changing the loading directions.

Table 5.5: Mean stress triaxialities over the notched cross-section for bi-cyclic loadings (Wei et al., 2024a).

Tests HC-cyc^2	positive superimposed loads at last loading stage			Tests HC-cyc^2	negative superimposed loads at last loading stage		
	RP1	RP2	FP		RP1	RP2	FP
-TTT3	0.18	0.20	0.28	-CCC3	-0.12	-0.14	-0.03
-TCT3	0.19	-0.16	0.28	-TCC3	0.18	-0.15	-0.03
-CTT3	-0.11	0.18	0.26	-CTC3	-0.10	0.19	-0.05
-TTT5	0.29	0.28	0.38	-CCC5	-0.18	-0.20	-0.12
-TCT5	0.29	-0.27	0.31	-TCC5	0.28	-0.26	-0.11
-CTT5	-0.24	0.28	0.35	-CTC5	-0.24	0.28	-0.11

The evolution of the damage strains A_1^{da} and strain increments ΔA_1^{da}

Table 5.6: Mean stress Lode parameters over the notched cross-section for bi-cyclic loadings (Wei et al., 2024a).

Tests HC-cyc^2	positive superimposed loads at last loading stage			Tests HC-cyc^2	negative superimposed loads at last loading stage		
	RP1	RP2	FP		RP1	RP2	FP
-TTT3	-0.28	-0.20	-0.22	-CCC3	0.17	0.21	0.00
-TCT3	-0.28	0.20	-0.23	-TCC3	-0.28	0.21	-0.01
-CTT3	0.16	-0.21	-0.22	-CTC3	0.14	-0.20	-0.02
-TTT5	-0.47	-0.41	-0.41	-CCC5	0.26	0.24	0.16
-TCT5	-0.46	0.40	-0.41	-TCC5	-0.46	0.42	0.12
-CTT5	0.38	-0.42	-0.39	-CTC5	0.38	-0.42	0.13

are shown in Fig. 5.31. It is observed that no damage occurs in the test with a positive load applied to axis 2 during the first loading stage. Conversely, damage appears as discrete points on the top and bottom of the notch surface when axis 2 is subjected to the negative load in the first loading stage. This is typical due to the localization of plastic strains, as evidenced by the larger first principal strains observed at RP1 in the Fig. 5.30. In addition, different evolutionary patterns are presented under various loading histories during subsequent loading stages.

As illustrated in Figs. 5.31(a)-(c), damage mainly develops in the notch cross-section in the second loading pattern (from RP1 to RP2). Subsequently, the changes of damage are predominant in the notch surfaces. Interestingly, negative damage strain increments are numerically predicted in the loading pattern HC-cyc^2-TCT3 in its notched cross-section center, with a value of $\Delta A_1^{\mathrm{da}} = -0.2\%$. The same phenomenon is observed in the test HC-cyc^2-TCT5, where negative damage strain increments are numerically predicted in previously damaged regions, as shown in Fig. 5.31(e). This indicates that the previous micro-shear-cracks, caused by negative stress triaxialities induced by simultaneous negative loading in both axes 1 and 2, change their deformation directions in the final loading pattern. Furthermore, the maximum damage strains are 0.47%, 0.44%, and 0.40% for the tests HC-cyc^2-TTT3, -TCT3, and -CTT3, respectively. Compared to the experiments mentioned above with 3 kN, significantly larger maximum damage strains are numerically predicted for the experiments HC-cyc^2-TTT5, -TCT5, and -CTT5, with

values of 0.54%, 2.21%, and 0.68%, respectively. The locations of damage also differ from each other. For instance, in the tests with $3\,\mathrm{kN}$ in the final loading stage, damage is localized in the notch cross-sections, whereas the maximal damage appears on the notched surfaces for experiments superimposed by $5\,\mathrm{kN}$. It is worth noting that the distribution of damage strains for tests HC-cyc^2-TTT3 and -TTT5 is nearly identical to that in single cyclic loading with superimposed tensile preloads of $3\,\mathrm{kN}$ and $5\,\mathrm{kN}$ (HC-cyc-T3 and -T5), as shown in Figs. 5.23(b) and (d). The reason for this is that if non-reverse cyclic loads are imposed on axis 2, e.g., TTT and CCC, the stress triaxialities remain positive and similar to the tests with constant superimposed loads on axis 2. These findings highlight that loading histories, especially reverse loading, and loading sequences, along with the magnitude of the loads, significantly influence damage development.

In the case of experiments with superimposed negative loads in the last loading stage, significant damage is observed in tests with negative loads on both axes, namely HC-cyc^2-CCCx and -TCCx. Negative stress triaxialities are generated, as seen in Table 5.5, leading to growth and coalescence of micro-shear-cracks. Consequently, this results in larger values of the first principal strains, as shown in Figs. 5.31(g)–(l). It must be noted that the quantity of the damage strains in this case indicates that the micro-shear-cracks are highly deformed in the loading direction. However, this does not mean earlier failure compared to experiments with a tensile load in the last loading stage. Moreover, negative strain increments are observed when previously formed micro-shear-cracks deform in the opposite direction compared to the previous loading stage. This suggests a reversal in the deformation pattern of these micro-shear-cracks under changing loading conditions. This phenomenon highlights the sensitivity of micro-shear-cracks to loading history and direction. The numerically predicted final maximum damage strains are present on the top and bottom of the notch surfaces under all loading cases, as depicted in Figs. 5.31(g)–(l), where obvious distortions and deformations are observed. Among these, the distributions of damage strains under loading patterns CCC3 and CCC5 are similar to those observed in the single cyclic tests with negative preloads, e.g., HC-cyc-TN3 and HC-cyc-TN5, as illustrated in Figs. 5.23(c) and (e), respectively. Moreover, the damage strains demonstrate a broader range when compared to
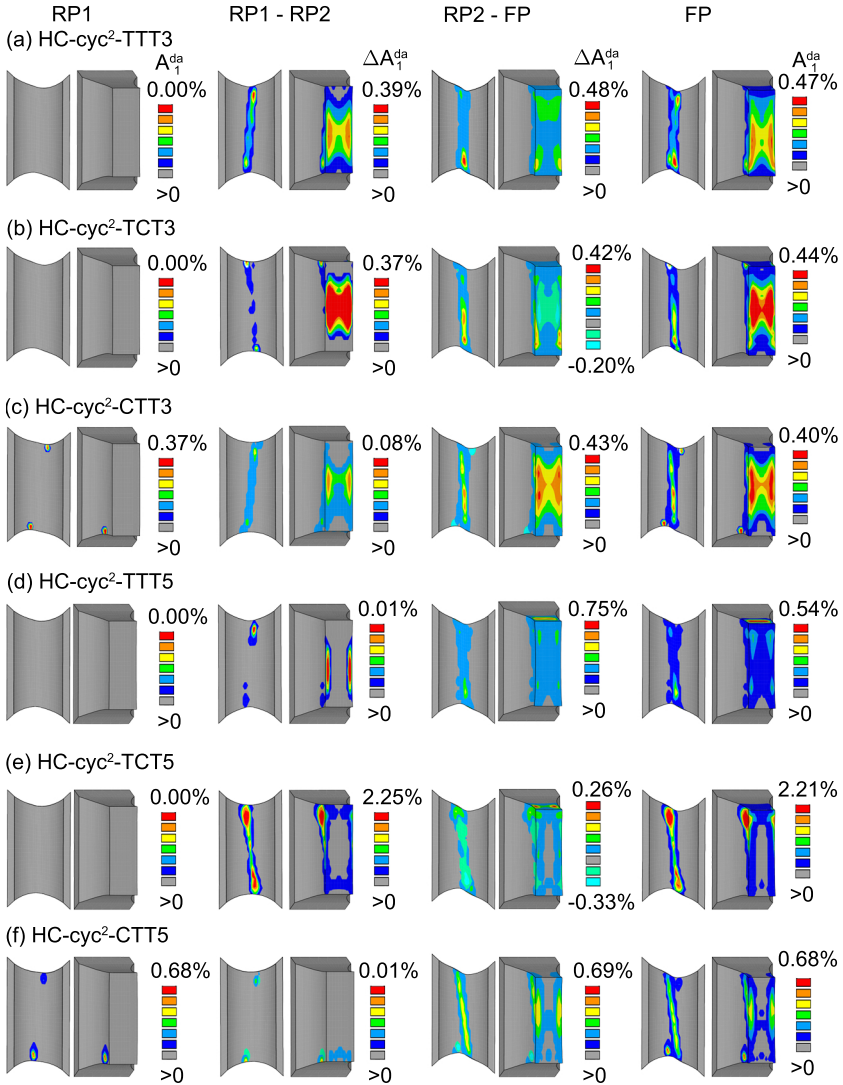
Figure 5.31: The changes in the first principal damage strain ΔA_1^{da} at various reverse points (RPs) and fracture point (FP) (Wei et al., 2024a).
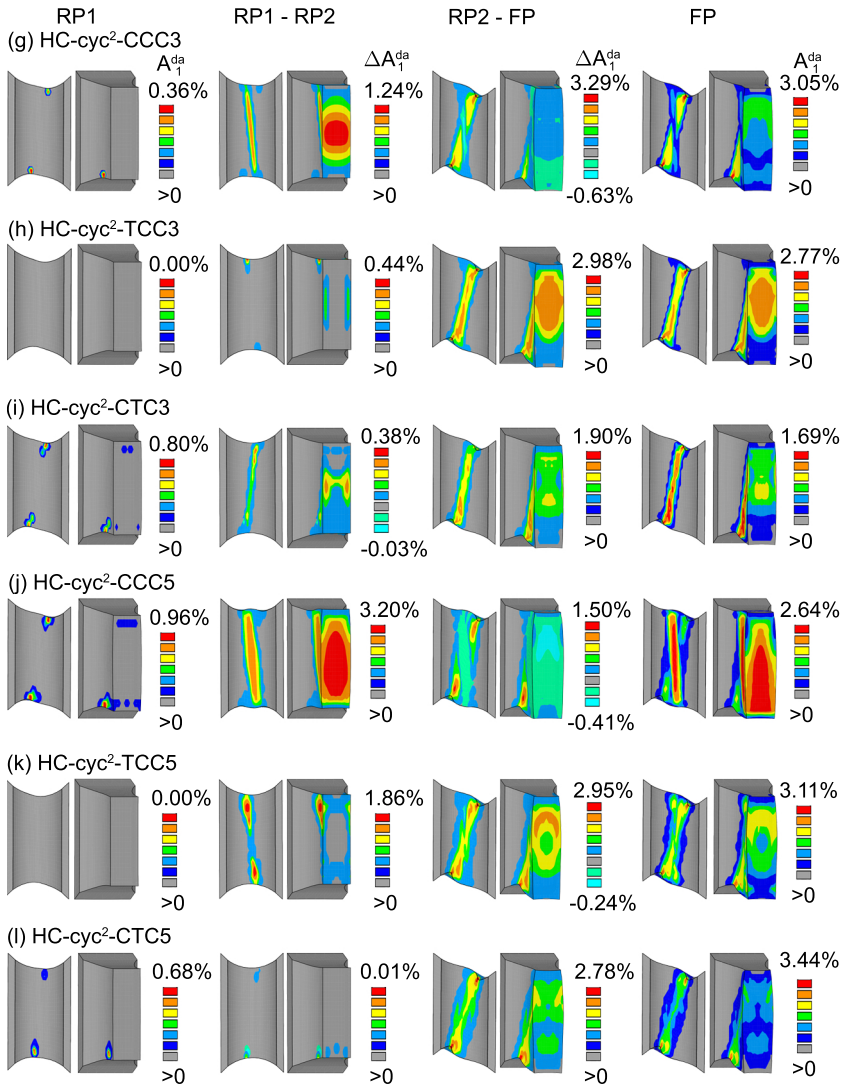
Figure 5.31: The changes in the first principal damage strain ΔA_1^{da} at various reverse points (RPs) and fracture point (FP) (continuation) (Wei et al., 2024a).

experiments conducted under positive loads, as shown in Figs. 5.31(a)–(f). Among these tests, those superimposed by $-3\,\mathrm{kN}$ in the last loading pattern (Figs. 5.31(g)–(i)) exhibit a narrower damage shear band compared to the experiments conducted with $-5\,\mathrm{kN}$ (Figs. 5.31(j)–(l)) in the final loading stage. The above findings confirm the influence of loading histories, loading sequences, and reverse loading paths on damage behavior.

Furthermore, SEM images taken from fracture surfaces (notched cross-sections) and fracture pictures on the notch surfaces are shown in Fig. 5.32 and Fig. 5.33, respectively. Micro-voids are prominently visible in specimens imposed by tensile loads during the final loading stage, as seen in Figs. 5.32(a)–(f), whereas micro-shear-cracks predominate in tests conducted under negative loads in the last loading stage, as depicted in Figs. 5.32(g)–(l). These SEM images confirm that high positive stress triaxialities lead to growth and coalescence of micro-voids, while negative and low positive stress states result in the growth and coalescence of micro-shear-cracks. The size and depth of the micro-voids in Figs. 5.32(d)–(f) are slightly greater than those in Figs. 5.32(a)–(c), indicating that higher stress triaxialities increase the depth of micro-voids. Notably, larger maximum damage strain values are predicted in the numerical simulations (Fig. 5.31), consistent with SEM observations. Furthermore, the numerically predicted damage strain increments from RP1 to RP2 under the loading pattern TCT in both axes significantly increase (Figs. 5.32(b) and (e)), attributed to larger negative stress triaxialities, leading to the development of micro-shear-cracks. Consequently, micro-shear-cracks are distinctly observed in the corresponding SEM images in Figs. 5.31(b) and (e), respectively. Specimens subjected to non-reverse cyclic loading (TTT) exhibit fewer coalesced micro-shear-cracks compared to those imposed by reversed cyclic loading (TCT and CTT). In addition, the fracture lines depicted in Figs. 5.33(a)–(f) align with the distribution of the numerically predicted total strain A_1 and damage strain A_1^{da} on the notch surfaces, as illustrated in Figs. 5.30 and 5.31, respectively.

Additionally, SEM images Figs. 5.32(g)–(i) and (j)–(l) show only slight differences for the specimens subjected to negative loads in the last loading patterns. One possible reason could be that, on the one hand, the first tensile loading pattern with TCC shows no distribution for the oc-

(a) HC-cyc²-TTT3 (b) HC-cyc²-TCT3 (c) HC-cyc²-CTT3

20 µm   20 µm   20 µm

(d) HC-cyc²-TTT5 (e) HC-cyc²-TCT5 (f) HC-cyc²-CTT5

20 µm   20 µm   20 µm

(g) HC-cyc²-CCC3 (h) HC-cyc²-TCC3 (i) HC-cyc²-CTC3

20 µm   20 µm   20 µm

(j) HC-cyc²-CCC5 (k) HC-cyc²-TCC5 (l) HC-cyc²-CTC5

20 µm   20 µm   20 µm
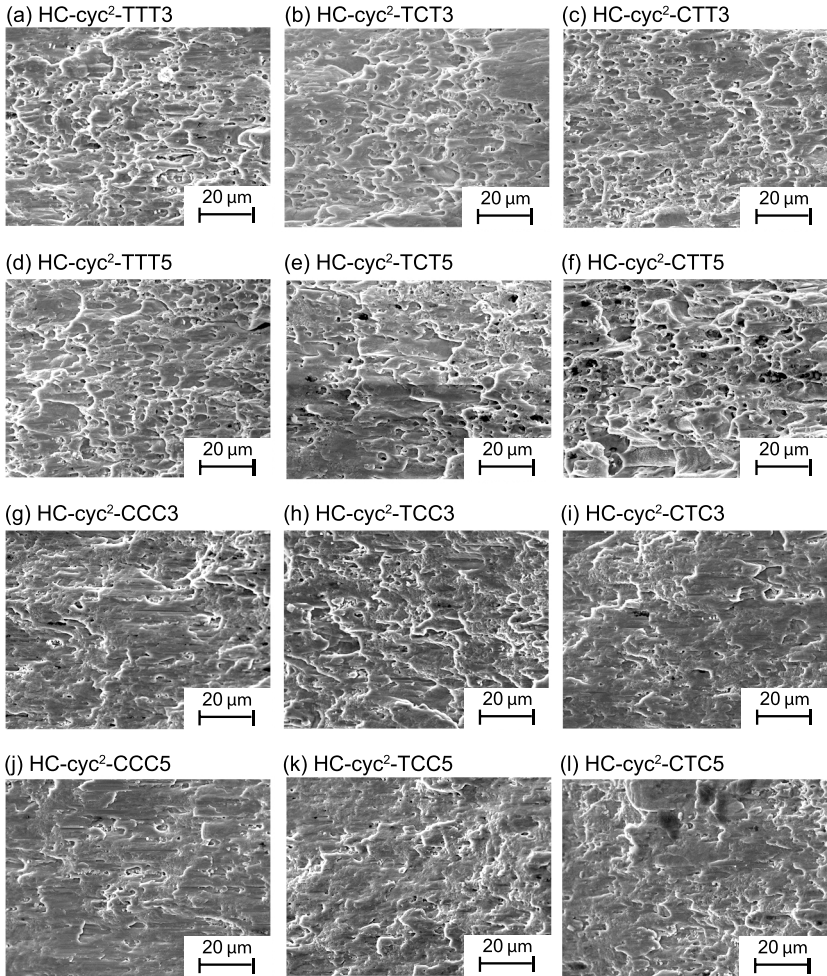
Figure 5.32: SEM images for bi-cyclic biaxial loadings.

currence and development of damage. Numerically predicted results indicate the absence of damage in these loading cases. On the other hand, the tensile loading pattern in the second loading phase results in positive

stress triaxialities, leading the previously formed micro-shear-cracks to
grow more challenging in the hydrostatic stress increasing direction, as
observed and discussed in Section 5.3.3. Furthermore, a near-zero stress
triaxiality is observed for the test superimposed by $-3\,\mathrm{kN}$, leading to
fracture behavior similar to shear tests. Compared to the specimens with
$-5\,\mathrm{kN}$, more small single voids can be observed in Figs. 5.32(g)–(i), given
that the generated stress triaxialities are nearly -0.01 for the experiments
superimposed by $-3\,\mathrm{kN}$. Moreover, rough fracture layers can be seen in
Figs. 5.32(j)–(l), indicating a more ductile behavior. Figs. 5.33(g)–(i)
visually demonstrates that specimens partially break into distinct parts
along the shear band, aligning closely with the numerical predictions
presented for the total strains in Figs. 5.30(g)–(i). In contrast, the speci-

(a) TTT3   (b) TCT3   (c) CTT3   (d) TTT5   (e) TCT5   (f) CTT5

(g) CCC3   (h) TCC3   (i) CTC3   (j) CCC5   (k) TCC5   (l) CTC5
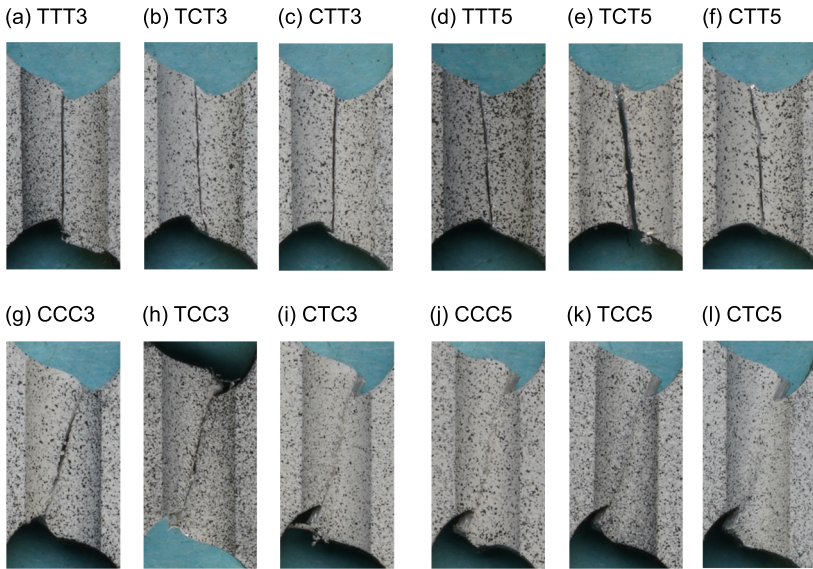
Figure 5.33: Fracture pictures on the notch surfaces for bi-cyclic biaxial
loadings.

mens subjected to $-5\,\mathrm{kN}$ do not break into parts; instead, only noticeable
fracture lines are observed on the top and bottom of the notched surface,
where SEM images are taken.

Summary

Bi-cyclic loading tests involve non-reverse (HC-cyc^2-TTT and -CCC), and reverse cyclic loads in axis 2 are discussed. Experiments subjected to both simultaneous reverse loads achieve nearly zero strain states at the end of the loading pattern. Different stress states are successfully generated, with stress triaxialities ranging from approximately -0.3 to 0.4. Stress states remain nearly constant for the specimens with loading patterns TTT and CCC, while the stress triaxialities alter from positive to negative or negative to positive for experiments with reverse cyclic loadings. It enables the study of the evolution of damage under different stress triaxialities. Moreover, SEM images highlight that micro-voids predominantly contribute to damage under high stress triaxialities in the tests superimposing positive loads in the last loading pattern. Conversely, micro-shear-cracks are responsible for damage in the tests with negative loads. In addition, the tensile loads superimposed in the last loading pattern increase the brittleness of the material, while compressive loading enhances its ductility. These findings conclude that loading patterns and directions significantly alter the material behavior.

Concerning the numerical simulations, the numerically predicted load–displacement curves and local strain fields give good agreements with the experimental ones. Notably, the numerical results accurately capture the strain fields throughout the loading processes, not just those immediately before failure. The evolution of the first principal total strains and of the damage strains clearly show and explain how the loading patterns and sequences influence plastic, damage, and fracture behavior.

6 Conclusions and outlook

The ductile damage and fracture behavior of the 4 mm thick sheet of aluminum EN AW6082-T6 under non-proportional and reverse loading conditions is discussed. Different one-axial and biaxial experiments are conducted to investigate the plastic, damage, and fracture behavior at both macro- and micro-levels using digital image correlation (DIC) technique and scanning electron microscopy (SEM). Corresponding numerical simulations are performed in Ansys with a novel modified two-surface anisotropic cyclic elastic–plastic–damage continuum model. This model is implemented in Ansys as a user-defined subroutine (UMAT) to capture the mechanical responses accurately, to elucidate the experimentally observed phenomena, and to reveal mechanisms which cannot be detected by experiments alone. The proposed material model accurately characterizes the material behavior in global load–displacement curves and local in strain states during the loading processes. One of the most significant advantages is that the proposed model shows excellent performance in modeling the experiments under complex loading conditions without changing the fitted material parameters. In addition, the proposed damage mechanisms provide a good explanation for the occurrence and development of damage during reverse loading conditions and different kinds of damage mechanisms, allowing judgment of safety and prediction of service lifetime of structures.

Concerning the numerical aspects, the combined hardening law is incorporated in the Drucker-Prager yield condition to capture the Bauschinger effect and strength-differential (SD) effect. A most straightforward approach is proposed to characterize the change in hardening ratio after shear reverse loading conditions by introducing a scalar hardening correction factor. In addition, a novel softening law based on damage strain rate tensor is used to model the transformation of the damage surface. Moreover, the numerical implementation details of the proposed constitutive model are discussed in detail. The numerical integration algorithm is realized by the plastic predictor–elastic corrector in the effective ficti-

tious configurations, and the inelastic (plastic–damage) predictor–elastic corrector in the damaged configurations. In addition, different consistent tangent moduli respective to the numerical integration approach are expressly provided to meet the requirements of the global Newton–Raphson scheme. An active set strategy is employed to satisfy different constraints under the effective fictitious undamaged and damaged configurations, respectively. This approach enforces the Kuhn–Tucker conditions in the respective configurations, ensuring the efficiency and robustness of the proposed numerical scheme.

For the experimental aspects, uniaxial tension–compression, one-axial shear, and single biaxial and bi-cyclic biaxial reverse tests are proposed to generate a wide range of stress triaxialities to validate the elastic-plastic-damage material model. Hence, the newly designed tension-compression specimen (TC-specimen), one-axis-loaded shear specimen, and biaxially loaded HC-specimen are employed. Notably, the HC-specimen features four symmetric 2 mm thick notches at its center. When loads are applied along the horizontal axes (tension axis or axis 2), tension or compression stresses are generated. In contrast, loading along the vertical axis (shear axis or axis 1) results in shear stresses. Non-proportional reverse experiments can be achieved by altering the loading direction and axes, allowing for varied loading conditions and directional changes in testing procedures.

Monotonic and different cyclic uniaxial tension-compression and shear tests are used to study the damage behavior caused by the growth and coalescence of micro-voids and micro-shear-cracks, respectively. Limited stress triaxialities are generated in the uniaxial tension-compression and one-axial shear tests, i.e., $1/3$ for the tension test, $-1/3$ for the compression test, and approximately -0.2 to 0.2 for cyclic shear tests. The Bauschinger effect and the SD effect are observed under monotonic and cyclic uniaxial tension-compression loading conditions, respectively. Most importantly, the experimental data enable the identification of material parameters in the proposed continuum model, providing good accuracy. One of the most significant contributions of the one-axial shear cyclic tests is the noticeable change in hardening after shear reverse loading, providing effective experimental data to model this observed non-hardening effect and calibrate its material parameters. Moreover, both experimental and numerical results show that cyclic loading conditions

increase the material brittleness of the investigated material compared to monotonic loading, as larger and more coalesced micro-defects are formed. In addition, the various cyclic loading patterns clearly demonstrate that damage occurs and develops in the earlier loading cycles, providing a significant difference compared to the monotonic loading case. Therefore, only the tension-compression-tension (TCT) loading pattern is chosen for the biaxial reverse experiments as it is representative to study the influence of the reverse loading condition with a large number of non-proportional loading paths.

Furthermore, single and bi-cyclic biaxial reverse experiments are conducted to broaden the range of stress triaxialities. On the one hand, single biaxial reverse experiments include shear reversals with tensile or compressive preloads, and tensile reversals with shear preloads. The loading processes are divided into two distinct stages: initially, tensile/compressive or shear preloads are imposed on the horizontal or vertical axis, respectively, until the desired force is attained. Without unloading, shear or tensile cyclic loads (loading pattern: TCT) are then additionally superimposed on the vertical or horizontal axis, respectively. On the other hand, bi-cyclic biaxial experiments involve imposing cyclic loads on both axes simultaneously. Different non-reversal and reversal cyclic loads applied to the horizontal axis are selected to be superimposed with the shear cyclic loading (loading pattern: TCT) on the vertical axis. Particularly, the loads on the horizontal axis will be kept constant when the maximum or minimum forces are reached in the final loading stage. These single and bi-cyclic biaxial experiments successfully generate a wider range of stress triaxialities, approximately from -0.33 to 0.75. Moreover, constant positive or negative stress triaxialities are induced in shear experiments with different tensile or compressive preloads, and in bi-cyclic biaxial experiments with non-reversal cyclic loads on the horizontal axis. Conversely, stress triaxialities that change from positive to negative or vice versa are generated by the tensile reverse experiments with shear preloads, and by bi-cyclic biaxial experiments with reversal cyclic loading on the horizontal axis. Therefore, different plastic, damage and fracture behaviors can be observed in experimental results or numerical simulations.

Based on analyses of global load–displacement curves, along with corresponding fracture displacements and forces, it is emphasized that the

directions of preloading, their magnitude, as well as the loading sequence and patterns, considerably influence material behavior at the macro-level. For instance, tensile and shear preloads increase the brittleness of the investigated material, whereas compressive preloads enhance the ductility of the ductile aluminum alloy. Additionally, the material's brittleness is further enhanced with increasing tensile or shear preloads. Similarly, its ductility increases with increasing compressive preloads. Additional observations indicate that cyclic loading conditions also result in the material becoming more brittle compared to those under monotonic loading conditions. In the case of bi-cyclic biaxial experiments, those with non-reversal cyclic loading on the horizontal axis have been seen to reduce the ductility of the material compared to that ones with reversal cyclic loading. Furthermore, a noticeable change in the hardening ratio (non-hardening effect) after shear reverse loading is observed in experiments with tensile or compressive preloads, similar to findings in one-axial shear cyclic experiments. However, this phenomenon is not as significant in tensile reverse experiments with shear preloads. Additionally, the re-yielding stresses after the second reverse loading pattern increase significantly under tensile cyclic conditions compared to monotonic loading. The experimental results also reveal that the degree of enhancement in re-yielding stress depends on the previously imposed compressive (C) displacements in the second loading stage of the cyclic loading pattern TCT. Large compressive displacements result in higher re-yielding stresses.

Loading histories, patterns, and sequences significantly affect the occurrence and evolution of damage behavior at the micro-level, as evidenced by the numerical analysis of damage strains and observation of SEM images. On the one hand, the numerical results show that damage might develop, transferring from the notch surface to the notched cross-section or vice versa due to reverse loading conditions. Negative damage strain increments are numerically predicted for cyclic tests, inducing changes from negative stress triaxialities to low positive stress triaxialities or maintaining negative stress triaxialities. Given the observed damage mechanism, one possible explanation could be that negative stress triaxialities cause the occurrence and development of micro-shear-cracks. These previously formed micro-shear-cracks are then more likely to deform easily in the opposite direction following the alteration of the loading direction. However, the growth of previously formed micro-shear-cracks becomes chal-

lenging under high stress triaxialities, especially in the direction of increasing hydrostatic stress. Thus, this leads to increase in the re-yielding stresses, as observed in the tensile reverse experiments with shear loads. On the other hand, damage is observed to be caused by growth and coalescence of micro-defects under positive stresses. This is evident in the shear reverse experiments with tensile preloads, tensile reverse experiments with shear preloads, and bi-cyclic biaxial reverse experiments where a tensile superimposed load is applied in the final loading stage. Conversely, micro-shear-cracks lead to damage under negative stress triaxialities, as demonstrated in the shear reverse experiments with negative preloads and bi-cyclic biaxial reverse experiments where a negative superimposed load is imposed on the final loading stage. SEM images also highlight that larger micro-voids and coalesced micro-shear-cracks appear under cyclic loading conditions compared to monotonic loading. In addition, the depth of the micro-defects might increase with increasing stress triaxialities. Most importantly, the SEM images confirmed the proposed damage mechanism and are consistent with the respective numerical predictions.

The stress triaxiality and the Lode parameter can effectively distinguish the stress state for different loading patterns under monotonic loading conditions. However, they need an extra parameter to properly differentiate between different stress states under various loading patterns during cyclic loading. To address this challenge, the strain Lode parameter is proposed for use in conjunction with the stress triaxiality and the stress Lode parameters.

This study utilizes a linear combination of the first I_1 and second stress invariants J_2 in the yield function, considering the observed slight strength-differential (SD) effect in the investigated aluminum alloy. To broaden the applicability of the proposed material model and capture a more significant SD effect, an additional term involving the third stress invariant J_3 should be considered. Similarly, it is suggested to incorporate the influence of the third stress invariant J_3 into the damage function to more accurately capture the initiation of damage under various complex negative stress states. To capture the stress-state-dependent parameters on the damage condition, a series of one-axial and biaxial experiments need to be conducted under loading and reloading (without reverse loading) to measure the change in Young's modulus. Additionally, specimens can

be examined metallographically with micrographs at different loading-reloading stages to more accurately characterize the initiation of damage compared to the indirect numerical method. The stress-state-dependent material parameters in the damage strain rate tensor are fitted by studying mechanical behavior of the unit-cell containing one 3% volume void under monotonic loading. Although the fitted material parameters are confirmed by the experimental results, the void behavior under different cyclic loadings should continue to be studied. As mentioned above, the stress triaxiality and the stress Lode parameter could not correctly capture the stress states under cyclic loading; thus, the newly carried out micro-numerical simulations should focus on how stress-state-dependent parameters are also affected by the strain Lode parameter after different reverse loadings. Due to advancements in experimental technology and calculation capabilities, it is suggested using X-ray tomography and electron backscatter diffraction (EBSD) to measure the size of voids for the investigated material. The measured size can be utilized in the simulations, considering a random spatial void distribution within the unit-cell. Developing fracture criteria based on damage strain is crucial for future research. This newly proposed fracture criterion should accurately describe fracture behavior under a wide range of stress states, distinguishing between monotonic and cyclic loading conditions. From a numerical perspective, it should also be designed for ease of implementation by different users.

The concept of non-proportional loading, such as shear to tension or tension to shear, can be further explored to investigate how damage behavior changes under cyclic loading. Similar to non-proportional loading, where monotonic shear loading is initially applied along the vertical axis and then unloaded to zero, the specimens could be subjected to shear cyclic loading along the horizontal axis until failure. In this new experimental program, cyclic loading is first imposed on the horizontal axis with a certain number of loading cycles until zero force is reached. Subsequently, cyclic loading is applied along the vertical axis with a different loading pattern. The different numbers of loading cycles in the first loading stage demonstrate when these micro-defects develop and to what extent they are more favorable or hindered in influencing the subsequent stages of the loading axis. Similar experiments can be conducted by changing the loading axis, for example, from shear cyclic to tensile cyclic. These ex-

periments allow to observe how the previously formed micro-voids and micro-shear-cracks evolve. Additionally, experiments with different loading cycles (e.g., 15, 30, and 50 large loading strain cycles or more) are suggested to understand the distinction between ductile and fatigue damage. A new one-axis-loaded tension-compression specimen with only one notch in its rectangular shape is needed to achieve this with one-axial tensile cyclic loading tests. Similar specimens can be found in (Gao et al., 2010).

Bibliography

Abu Al-Rub, R. K. and G. Z. Voyiadjis (2003). "On the coupling of anisotropic damage and plasticity models for ductile materials". *Int. J. Solids Struct.* 40, 2611–2643.

Algarni, M., Y. Bai, M. Zwawi, and S. Ghazali (2019). "Damage evolution due to extremely low-cycle fatigue for Inconel 718 alloy". *Metals* 9, 1109.

Ansys, Inc. (2013). *Ansys Mechanical APDL Programmers Reference 15.0.*

Badreddine, H. and K. Saanouni (2017). "On the full coupling of plastic anisotropy and anisotropic ductile damage under finite strains". *Int. J. Damage Mech.* 26, 1080–1123.

Bai, Y. and T. Wierzbicki (2008). "A new model of metal plasticity and fracture with pressure and Lode dependence". *Int. J. Plast.* 24, 1071–1096.

Balieu, R. and N. Kringos (2015). "A new thermodynamical framework for finite strain multiplicative elastoplasticity coupled to anisotropic damage". *Int. J. Plast.* 70, 126–150.

Bao, Y. and T. Wierzbicki (2004). "On fracture locus in the equivalent strain and stress triaxiality space". *Int. J. Mech. Sci.* 46, 81–98.

Bao, Y. and T. Wierzbicki (2005). "On the cut-off value of negative triaxiality for fracture". *Eng. Fract. Mech.* 72, 1049–1069.

Barlat, F., J. M. Ferreira Duarte, J. J. Gracio, A. B. Lopes, and E. F. Rauch (2003). "Plastic flow for non-monotonic loading conditions of an aluminum alloy sheet sample". *Int. J. Plast.* 19, 1215–1244.

Barsoum, I. and J. Faleskog (2007). "Rupture mechanisms in combined tension and shear experiments". *Int. J. Solids Struct.* 44, 1768–1786.

Betten, J. (1982). "Net-stress analysis in creep mechanics". *Ing. Arch.* 52, 405–419.

Betten, J. (1983). "Damage tensors in continuum mechanics". *J. méc. théor. appl.* 2, 13–32.

Boger, R. K., R. H. Wagoner, F. Barlat, M. G. Lee, and K. Chung (2005). "Continuous, large strain, tension/compression testing of sheet material". *Int. J. Plast.* 21, 2319–2343.

Brünig, M. (1999a). "Large strain elastic-plastic theory and nonlinear finite element analysis based on metric transformation tensors". *Comput. Mech.* 24, 187–196.

Brünig, M. (1999b). "Numerical simulation of the large elastic–plastic deformation behavior of hydrostatic stress-sensitive solids". *Int. J. Plast.* 15, 1237–1264.

Brünig, M. (2001). "A framework for large strain elastic–plastic damage mechanics based on metric transformations". *Int. J. Eng. Sci.* 39, 1033–1056.

Brünig, M. (2003a). "An anisotropic ductile damage model based on irreversible thermodynamics". *Int. J. Plast.* 19, 1679–1713.

Brünig, M. (2003b). "Numerical analysis of anisotropic ductile continuum damage". *Comput. Methods Appl. Mech. Eng.* 192, 2949–2976.

Brünig, M., S. Berger, and H. Obrecht (2000). "Numerical simulation of the localization behavior of hydrostatic-stress-sensitive metals". *Int. J. Mech. Sci.* 42, 2147–2166.

Brünig, M., O. Chyra, D. Albrecht, L. Driemeier, and M. Alves (2008). "A ductile damage criterion at various stress triaxialities". *Int. J. Plast.* 24, 1731–1755.

Brünig, M., S. Gerke, and D. Brenner (2015). "Experiments and numerical simulations on stress-state-dependence of ductile damage criteria". In: *Inelastic behavior of materials and structures under monotonic and cyclic loading.* Ed. by H. Altenbach and M. Brünig. Vol. 57. Springer International Publishing, 17–33.

Brünig, M., S. Gerke, and V. Hagenbrock (2013). "Micro-mechanical studies on the effect of the stress triaxiality and the Lode parameter on ductile damage". *Int. J. Plast.* 50, 49–65.

Brünig, M., S. Gerke, and V. Hagenbrock (2014). "Stress-state-dependence of damage strain rate tensors caused by growth and coalescence of micro-defects". *Int. J. Plast.* 63, 49–63.

Brünig, M., S. Gerke, and S. Koirala (2021a). "Biaxial experiments and numerical analysis on stress-state-dependent damage and failure behavior of the anisotropic aluminum alloy EN AW-2017A". *Metals* 11, 1214.

Brünig, M., S. Gerke, and M. Schmidt (2016). "Biaxial experiments and phenomenological modeling of stress-state-dependent ductile damage and fracture". *Int. J. Fract.* 200, 63–76.

Brünig, M., S. Gerke, and M. Schmidt (2018). "Damage and failure at negative stress triaxialities: experiments, modeling and numerical simulations". *Int. J. Plast.* 102, 70–82.

Brünig, M., S. Gerke, and M. Zistl (2019a). "Experiments and numerical simulations with the H-specimen on damage and fracture of ductile metals under non-proportional loading paths". *Eng. Fract. Mech.* 217, 106531.

Brünig, M., S. Koirala, and S. Gerke (2023). "A stress-state-dependent damage criterion for metals with plastic anisotropy". *Int. J. Damage Mech.*, 105678952311608.

Brünig, M. and A. Michalski (2017). "A stress-state-dependent continuum damage model for concrete based on irreversible thermodynamics". *Int. J. Plast.* 90, 31–43.

Brünig, M., M. Schmidt, and S. Gerke (2021b). "Numerical analysis of stress-state-dependent damage and failure behavior of ductile steel based on biaxial experiments". *Comput. Mech.*, 1–11.

Brünig, M., M. Zistl, and S. Gerke (2019b). "Modeling of damage of ductile materials". In: *State of the art and future trends in material modeling*. Ed. by H. Altenbach and A. Öchsner. Vol. 100. Springer International Publishing, 49–78.

Brünig, M., M. Zistl, and S. Gerke (2021c). "Numerical analysis of experiments on damage and fracture behavior of differently preloaded aluminum alloy specimens". *Metals* 11, 381.

Cao, J., W. Lee, H. S. Cheng, et al. (2009). "Experimental and numerical investigation of combined isotropic-kinematic hardening behavior of sheet metals". *Int. J. Plast.* 25, 942–972.

Chaboche, J.-L. (1984). "Anisotropic creep damage in the framework of continuum damage mechanics". *Nucl. Eng. Des.* 79, 309–319.

Chaboche, J.-L. (1986). "Time-independent constitutive theories for cyclic plasticity". *Int. J. Plast.* 2, 149–188.

Chaboche, J.-L. (1988a). "Continuum damage mechanics: part I—general concepts". *J. Appl. Mech.* 55, 59–64.

Chaboche, J.-L. (1988b). "Continuum damage mechanics: part II—damage growth, crack initiation, and crack growth". *J. Appl. Mech.* 55, 65–72.

Chaboche, J.-L. (1992). "Damage induced anisotropy: On the difficulties associated with the active/passive unilateral Condition". *Int. J. Damage Mech.* 1, 148–171.

Chaboche, J.-L. (2008). "A review of some plasticity and viscoplasticity constitutive theories". *Int. J. Plast.* 24, 1642–1693.

Chaboche, J.-L. and G. Rousselier (1983). "On the plastic and viscoplastic constitutive equations—Part I: rules developed with internal variable concept". *J. Pressure Vessel Technol.* 105, 153–158.

Chu, C. C. and A. Needleman (1980). "Void nucleation effects in biaxially stretched sheets". *J. Eng. Mater. Technol.* 102, 249–256.

Cortese, L., F. Nalli, and M. Rossi (2016). "A nonlinear model for ductile damage accumulation under multiaxial non-proportional loading conditions". *Int. J. Plast.* 85, 77–92.

Daroju, S., T. Kuwabara, R. Sharma, et al. (2022). "Experimental characterization and crystal plasticity modeling for predicting load reversals in AA6016-T4 and AA7021-T79". *Int. J. Plast.* 153, 103292.

Demmerle, S. and J.-P. Boehler (1993). "Optimal design of biaxial tensile cruciform specimens". *J. Mech. Phys. Solids* 41, 143–181.

Drucker, D. C. and W. Prager (1952). "Soil mechanics and plastic analysis or limit design". *Q. Appl. Math.* 10, 157–165.

Dunand, M. and D. Mohr (2011). "On the predictive capabilities of the shear modified Gurson and the modified Mohr–Coulomb fracture models over a wide range of stress triaxialities and Lode angles". *J. Mech. Phys. Solids* 59, 1374–1394.

Faleskog, J. and I. Barsoum (2013). "Tension–torsion fracture experiments—Part I: Experiments and a procedure to evaluate the equivalent plastic strain". *Int. J. Solids Struct.* 50, 4241–4257.

Faleskog, J., X. Gao, and C. F. Shih (1998). "Cell model for nonlinear fracture analysis – I. Micromechanics calibration". *Int. J. Fract.* 89, 355–373.

Frederick, C. O. and P. J. Armstrong (2007). "A mathematical representation of the multiaxial Bauschinger effect". *Mater. High Temp.* 24, 1–26.

Gao, X., G. Zhang, and C. Roe (2010). "A study on the effect of the stress state on ductile fracture". *Int. J. Damage Mech.* 19, 75–94.

Gao, X., T. Zhang, J. Zhou, et al. (2011). "On stress-state dependent plasticity modeling: Significance of the hydrostatic stress, the third

invariant of stress deviator and the non-associated flow rule". *Int. J. Plast.* 27, 217–231.

Gerke, S., Z. Wei, and M. Brünig (2023). "Experiments on low-cycle ductile damage and failure under biaxial loading conditions". *Exp. Mech.*, (accepted).

Gerke, S., P. Adulyasak, and M. Brünig (2017). "New biaxially loaded specimens for the analysis of damage and fracture in sheet metals". *Int. J. Solids Struct.* 110-111, 209–218.

Graham, S. M., T. Zhang, X. Gao, and M. Hayden (2012). "Development of a combined tension–torsion experiment for calibration of ductile fracture models under conditions of low triaxiality". *Int. J. Mech. Sci.* 54, 172–181.

Gurson, A. L. (1977). "Continuum theory of ductile rupture by void nucleation and growth: part I—yield criteria and flow rules for porous ductile media". *J. Eng. Mater. Technol.* 99, 2–15.

Haltom, S. S., S. Kyriakides, and K. Ravi-Chandar (2013). "Ductile failure under combined shear and tension". *Int. J. Solids Struct.* 50, 1507–1522.

Hayakawa, K., S. Murakami, and Y. Liu (1998). "An irreversible thermodynamics theory for elastic-plastic-damage materials". *Eur. J. Mech. A Solids* 17, 13–32.

Hoffman, O. (1967). "The brittle strength of orthotropic materials". *J. Compos. Mater.* 1, 200–206.

Holmen, J. K., B. H. Frodal, O. S. Hopperstad, and T. Børvik (2017). "Strength differential effect in age hardened aluminum alloys". *Int. J. Plast.* 99, 144–161.

Hou, Y., M.-G. Lee, J. Lin, and J. Min (2022). "Experimental characterization and modeling of complex anisotropic hardening in quenching and partitioning (Q&P) steel subject to biaxial non-proportional loadings". *Int. J. Plast.* 156, 103347.

Jones, E., M. Iadicola, R. Bigger, et al. (2018). *A good practices guide for digital image correlation.* Ed. by International Digital Image Correlation Society.

Kanvinde, A. M. and G. G. Deierlein (2007). "Cyclic void growth model to assess ductile fracture initiation in structural steels due to ultra low cycle Fatigue". *J. Eng. Mech.* 133, 701–712.

Khan, A. S. and H. Liu (2012). "A new approach for ductile fracture prediction on Al 2024-T351 alloy". *Int. J. Plast.* 35, 1–12.

Khan, I. A., A. A. Benzerga, and A. Needleman (2023). "A shear modified enhanced Gurson constitutive relation and implications for localization". *J. Mech. Phys. Solids* 171, 105153.

Kiefer, B., T. Waffenschmidt, L. Sprave, and A. Menzel (2018). "A gradient-enhanced damage model coupled to plasticity—multi-surface formulation and algorithmic concepts". *Int. J. Damage Mech.* 27, 253–295.

Kong, X., T. F. Morgeneyer, D. Missoum-Benziane, and G. Rousselier (2023). "A polycrystalline damage model applied to an anisotropic aluminum alloy 2198 under non-proportional load path changes". *Int. J. Plast.* 168, 103674.

Koplik, J. and A. Needleman (1988). "Void growth and coalescence in porous plastic solids". *Int. J. Solids Struct.* 24, 835–853.

Krajcinovic, D. (1983). "Constitutive equations for damaging materials". *J. Appl. Mech.* 50, 355–360.

Krajcinovic, D. and G. U. Fonseka (1981). "The continuous damage theory of brittle materials, part 1: general theory". *J. Appl. Mech.* 48, 809–815.

Kulawinski, D., K. Nagel, S. Henkel, et al. (2011). "Characterization of stress–strain behavior of a cast TRIP steel under different biaxial planar load ratios". *Eng. Fract. Mech.* 78, 1684–1695.

Kuwabara, T. (2007). "Advances in experiments on metal sheets and tubes in support of constitutive modeling and forming simulations". *Int. J. Plast.* 23, 385–419.

Lee, E. H. (1969). "Elastic-plastic deformation at finite strains". *J. Appl. Mech.* 36, 1–6.

Lemaitre, J. (1985a). "A continuous damage mechanics model for ductile fracture". *J. Eng. Mater. Technol.* 107, 83–89.

Lemaitre, J. (1985b). "Coupled elasto-plasticity and damage constitutive equations". *Comput. Methods Appl. Mech. Eng.* 51, 31–49.

Lemaitre, J. (1986). "Local approach of fracture". *Eng. Fract. Mech.* 25, 523–537.

Lemaitre, J. (1996). *A Course on Damage Mechanics.* Springer.

Lemaitre, J., R. Desmorat, and M. Sauzay (2000). "Anisotropic damage law of evolution". *Eur. J. Mech. A Solids* 19, 187–208.

Lemaitre, J. and J. Dufailly (1987). "Damage measurements". *Eng. Fract. Mech.* 28, 643–661.

Lou, Y. and J. W. Yoon (2018). "Anisotropic yield function based on stress invariants for BCC and FCC metals and its extension to ductile fracture criterion". *Int. J. Plast.* 101, 125–155.

Lou, Y., J. W. Yoon, and H. Huh (2014). "Modeling of shear ductile fracture considering a changeable cut-off value for stress triaxiality". *Int. J. Plast.* 54, 56–80.

Lou, Y., S. Zhang, and J. W. Yoon (2020). "Strength modeling of sheet metals from shear to plane strain tension". *Int. J. Plast.* 134, 102813.

Lu, T. J. and C. L. Chow (1990). "On constitutive equations of inelastic solids with anisotropic damage". *Theor. Appl. Fract. Mech.* 14, 187–218.

Malcher, L., F. M. Andrade Pires, and J. César de Sá (2014). "An extended GTN model for ductile fracture under high and low stress triaxiality". *Int. J. Plast.* 54, 193–228.

Marcadet, S. J. and D. Mohr (2015). "Effect of compression–tension loading reversal on the strain to fracture of dual phase steel sheets". *Int. J. Plast.* 72, 21–43.

Mohr, D. and S. Henn (2007). "Calibration of stress-triaxiality dependent crack formation criteria: a new hybrid experimental–numerical method". *Exp. Mech.* 47, 805–820.

Müller, W. and K. Pöhlandt (1996). "New experiments for determining yield loci of sheet metal". *J. Mater. Process. Technol.* 60, 643–648.

Murakami, S. (1988). "Mechanical modeling of material damage". *J. Appl. Mech.* 55, 280–286.

Murakami, S. (2012). *Continuum Damage Mechanics*. Vol. 185. Springer Netherlands.

Murakami, S. and N. Ohno (1981). "A continuum theory of creep and creep damage". In: *Creep in Structures*. Vol. 6, 422–444.

Nahshon, K. and J. W. Hutchinson (2008). "Modification of the Gurson model for shear failure". *Eur. J. Mech. A Solids* 27, 1–17.

Nemat-Nasser, S. (1991). "Rate-independent finite-deformation elastoplasticity: a new explicit constitutive algorithm". *Mech. Mater.* 11, 235–249.

Nemat-Nasser, S. and Y.-F. Li (1992). "A new explicit algorithm for finite-deformation elastoplasticity and elastoviscoplasticity: Performance evaluation". *Comput. Struct.* 44, 937–963.

Nouailhas, D., G. Cailletaud, H. Policella, et al. (1985). "On the description of cyclic hardening and initial cold working". *Eng. Fract. Mech.* 21, 887–895.

Ohno, N. (1982). "A constitutive model of cyclic plasticity with a non-hardening strain region". *J. Appl. Mech.* 49, 721–727.

Ohno, N. and Y. Kachi (1986). "A constitutive model of cyclic plasticity for nonlinear hardening materials". *J. Appl. Mech.* 53, 395–403.

Okorokov, V., Y. Gorash, D. Mackenzie, and R. van Rijswick (2019a). "New formulation of nonlinear kinematic hardening model, Part I: A Dirac delta function approach". *Int. J. Plast.* 122, 89–114.

Okorokov, V., Y. Gorash, D. Mackenzie, and R. van Rijswick (2019b). "New formulation of nonlinear kinematic hardening model, Part II: Cyclic hardening/softening and ratcheting". *Int. J. Plast.* 122, 244–267.

Papasidero, J., V. Doquet, and D. Mohr (2015). "Ductile fracture of aluminum 2024-T351 under proportional and non-proportional multi-axial loading: Bao–Wierzbicki results revisited". *Int. J. Solids Struct.* 69-70, 459–474.

Peng, Wang, Dai, Liu, and Zhang (2019). "Effect of stress triaxiality on plastic damage evolution and failure mode for 316L notched specimen". *Metals* 9, 1067.

Prager, W. (1955). "The theory of plasticity: A survey of recent achievements". *Proc. Inst. Mech. Eng.* 169, 41–57.

Rabotnov, Y. N. (1969). "Creep rupture". In: *Applied Mechanics*. Ed. by M. Hetényi and W. G. Vincenti. Vol. I. Springer, 342–349.

Raj, A., R. K. Verma, P. K. Singh, et al. (2022). "Experimental and numerical investigation of differential hardening of cold rolled steel sheet under non-proportional loading using biaxial tensile test". *Int. J. Plast.* 154, 103297.

Ramberg, W. and J. A. Miller (1946). "Determination and presentation of compressive stress-strain data for thin sheet metal". *J. aeronaut. sci.* 13, 569–580.

Rong, H., P. Hu, L. Ying, W. Hou, and M. Dai (2022). "Modeling the anisotropic plasticity and damage of AA7075 alloy in hot forming". *Int. J. Mech. Sci.* 215, 106951.

Roth, C. C., T. F. Morgeneyer, Y. Cheng, L. Helfen, and D. Mohr (2018). "Ductile damage mechanism under shear-dominated loading: In-situ

tomography experiments on dual phase steel and localization analysis". *Int. J. Plast.* 109, 169–192.

Rousselier, G. (1987). "Ductile fracture models and their potential in local approach of fracture". *Nucl. Eng. Des.* 105, 97–111.

Rousselier, G. (2001). "The Rousselier model for porous metal plasticity and ductile fracture". In: *Handbook of Materials Behavior Models*. Ed. by J. Lemaitre. Elsevier, 436–445.

Rousselier, G. (2022). "Lode-dependent second porosity in porous plasticity for shear-dominated loadings". *Int. J. Plast.*, 103446.

Rousselier, G. and M. Luo (2014). "A fully coupled void damage and Mohr–Coulomb based ductile fracture model in the framework of a Reduced Texture Methodology". *Int. J. Plast.* 55, 1–24.

Saanouni, K. (2008). "On the numerical prediction of the ductile fracture in metal forming". *Eng. Fract. Mech.* 75, 3545–3559.

Simo, J. C. and J. W. Ju (1987). "Strain- and stress-based continuum damage models–I. Formulation". *Int. J. Solids Struct.* 23, 821–840.

Simo, J. C., J. G. Kennedy, and S. Govindjee (1988). "Non-smooth multisurface plasticity and viscoplasticity. Loading/unloading conditions and numerical algorithms". *Int. J. Numer. Meth. Eng.* 26, 2161–2185.

Spitzig, W. A. and O. Richmond (1984). "The effect of pressure on the flow stress of metals". *Acta Metall.* 32, 457–463.

Spitzig, W. A., R. J. Sober, and O. Richmond (1975). "Pressure dependence of yielding and associated volume expansion in tempered martensite". *Acta Metall.* 23, 885–893.

Stoughton, T. B. and J. W. Yoon (2004). "A pressure-sensitive yield criterion under a non-associated flow rule for sheet metal forming". *Int. J. Plast.* 20, 705–731.

Tvergaard, V. and A. Needleman (1984). "Analysis of the cup-cone fracture in a round tensile bar". *Acta Metall.* 32, 157–169.

Vignjevic, R., N. Djordjevic, and V. Panov (2012). "Modelling of dynamic behaviour of orthotropic metals including damage and failure". *Int. J. Plast.* 38, 47–85.

Voyiadjis, G. Z., S. H. Hoseini, and G. H. Farrahi (2012). "Effects of stress invariants and reverse loading on ductile fracture initiation". *Int. J. Solids Struct.* 49, 1541–1556.

Voyiadjis, G. Z., S. H. Hoseini, and G. H. Farrahi (2013). "A plasticity model for metals with dependency on all the stress invariants". *J. Eng. Mater. Technol.* 135.

Voyiadjis, G. Z. and P. I. Kattan (1992). "A plasticity-damage theory for large deformation of solids—I. Theoretical formulation". *Int. J. Eng. Sci.* 30, 1089–1108.

Voyiadjis, G. Z. and P. I. Kattan (2005). *Damage Mechanics*. CRC Press.

Voyiadjis, G. Z. and T. Park (1999). "The kinematics of damage for finite-strain elasto-plastic solids". *Int. J. Eng. Sci.* 37, 803–830.

Wang, L. H. and S. N. Atluri (1994). "An analysis of an explicit algorithm and the radial return algorithm, and a proposed modification, in finite plasticity". *Comput. Mech.* 13, 380–389.

Wei, Z., S. Gerke, and M. Brünig (2023a). "Characterization of ductile damage and fracture behavior under shear reverse loading conditions". *Proc. Appl. Math. Mech.*, e202300031.

Wei, Z., S. Gerke, and M. Brünig (2023b). "Damage and fracture behavior under non-proportional biaxial reverse loading in ductile metals: Experiments and material modeling". *Int. J. Plast.* 171, 103774.

Wei, Z., S. Gerke, and M. Brünig (2023c). "Mechanical responses of ductile aluminum alloy under biaxial non-proportional tensile reverse Loading Patterns". *Metals* 13, 1922.

Wei, Z., S. Gerke, and M. Brünig (2024a). "Ductile damage and fracture characterizations in bi-cyclic biaxial experiments". *Int. J. Mech. Sci.*, 109380.

Wei, Z., S. Gerke, and M. Brünig (2024b). "Numerical analysis of non-proportional biaxial reverse experiments with a two-surface anisotropic cyclic plasticity-damage approach". *Comput. Methods Appl. Mech. Eng.* 419, 116630.

Wei, Z., M. Zistl, S. Gerke, and M. Brünig (2022). "Analysis of ductile damage and fracture under reverse loading". *Int. J. Mech. Sci.*, 107476.

Wei, Z., M. Zistl, S. Gerke, and M. Brünig (2023d). "Analysis of ductile damage evolution and failure mechanisms due to reverse loading conditions for the aluminum alloy EN–AW 6082–T6". *Proc. Appl. Math. Mech.* 22, e202200012.

Wilson, C. D. (2002). "A critical reexamination of classical metal plasticity". *J. Appl. Mech.* 69, 63–68.

Yoshida, F., T. Uemori, and K. Fujiwara (2002). "Elastic–plastic behavior of steel sheets under in-plane cyclic tension–compression at large strain". *Int. J. Plast.* 18, 633–659.

Yu, F., P.-Y. B. Jar, and M. T. Hendry (2018). "Constitutive analysis of pressure-insensitive metals under axisymmetric tensile loading: A stress triaxiality-dependent plasticity damage model". *Int. J. Mech. Sci.* 142-143, 21–32.

Zillmann, B., M. F.-X. Wagner, S. Schmaltz, et al. (2015). "In-plane biaxial compression and tension testing of thin sheet materials". *Int. J. Solids Struct.* 66, 111–120.

Zistl, M., M. Brünig, and S. Gerke (2022a). "Analysis of damage and fracture behavior in ductile metal sheets undergoing compression and shear preloading". *Int J Mater Form* 15.

Zistl, M., S. Gerke, and M. Brünig (2022b). "Experiments on damage and failure behavior of biaxially loaded specimens under non-proportional load paths". In: *The 19th international conference on experimental mechanics.* Ed. by Physical Sciences Forum. MDPI, 23.